

INFORMATION TO USERS

This manuscript has been reproduced from the microfilm master. UMI films the text directly from the original or copy submitted. Thus, some thesis and dissertation copies are in typewriter face, while others may be from any type of computer printer.

The quality of this reproduction is dependent upon the quality of the copy submitted. Broken or indistinct print, colored or poor quality illustrations and photographs, print bleedthrough, substandard margins, and improper alignment can adversely affect reproduction.

In the unlikely event that the author did not send UMI a complete manuscript and there are missing pages, these will be noted. Also, if unauthorized copyright material had to be removed, a note will indicate the deletion.

Oversize materials (e.g., maps, drawings, charts) are reproduced by sectioning the original, beginning at the upper left-hand corner and continuing from left to right in equal sections with small overlaps. Each original is also photographed in one exposure and is included in reduced form at the back of the book.

Photographs included in the original manuscript have been reproduced xerographically in this copy. Higher quality 6" x 9" black and white photographic prints are available for any photographs or illustrations appearing in this copy for an additional charge. Contact UMI directly to order.

UMI

A Bell & Howell Information Company
300 North Zeeb Road, Ann Arbor MI 48106-1346 USA
313/761-4700 800/521-0600

A MEASUREMENT OF THE FINE-STRUCTURE
CONSTANT
USING ATOM INTERFEROMETRY

A DISSERTATION
SUBMITTED TO THE DEPARTMENT OF PHYSICS
AND THE COMMITTEE ON GRADUATE STUDIES
OF STANFORD UNIVERSITY
IN PARTIAL FULFILLMENT OF THE REQUIREMENTS
FOR THE DEGREE OF
DOCTOR OF PHILOSOPHY

By
Brenton Christopher Young
January 1997

UMI Number: 9723437

**UMI Microform 9723437
Copyright 1997, by UMI Company. All rights reserved.**

**This microform edition is protected against unauthorized
copying under Title 17, United States Code.**

UMI
300 North Zeeb Road
Ann Arbor, MI 48103

© Copyright 1997 by Brenton Christopher Young
All Rights Reserved

I certify that I have read this thesis and that in my opinion it is fully adequate, in scope and in quality, as a dissertation for the degree of Doctor of Philosophy.

Steve Chu

Steven Chu
(Principal Adviser)

I certify that I have read this thesis and that in my opinion it is fully adequate, in scope and in quality, as a dissertation for the degree of Doctor of Philosophy.

Mark A. Kasevich

Mark A. Kasevich

I certify that I have read this thesis and that in my opinion it is fully adequate, in scope and in quality, as a dissertation for the degree of Doctor of Philosophy.

Blas Cabrera

Blas Cabrera

Approved for the University Committee on Graduate Studies:

- Thomas Wallace -

Abstract

Using atom interferometry, we have measured the photon recoil frequency shift for cesium atoms caused by the absorption of up to 200 optical photons. Performing the measurement using cold atoms allowed interaction times as long as 400 ms, corresponding to 2.5 Hz FWHM interference fringes. We have achieved a measurement resolution of 120 ppb from 90 s of data. This is over an order-of-magnitude higher sensitivity than in a previous version of this experiment. We report a value $\Delta f_{\text{rec}} = 30,012.557\,3(16)(7)$ Hz for the photon recoil shift using the cesium D_1 line, where the first 1σ error bar is the 52 ppb limit from systematic errors, and the second error bar is the 22 ppb statistical uncertainty after 4 hours of data. The uncertainty in Δf_{rec} has improved over an order of magnitude from the previous photon recoil measurement. Combining this recoil-frequency-shift measurement with mass-ratio measurements and an absolute frequency measurement determines a value for the fine-structure constant of $\alpha^{-1} = 137.036\,002\,8(77)$. To within the stated uncertainty, this determination agrees with the value for α obtained from the anomalous magnetic moment of the electron. The largest contributor to the 56 ppb relative uncertainty of this determination of α is the uncertainty in the knowledge of the absolute frequency of the cesium D_1 line. The uncertainty in our measurement of Δf_{rec} limits the relative uncertainty in this α determination to 28 ppb.

Preface

For my parents,
who have supported and encouraged me in my education

Acknowledgements

I would like to thank my advisor Steven Chu for providing me with the opportunity to work on this experiment, which I have found both interesting and challenging. I appreciate all of the guidance that he has given me throughout the course of this experiment.

I would like to acknowledge David Weiss for all of the training he gave me during my early graduate student career. I also appreciate the careful thought that he has put into the photon recoil measurement, particularly as contained in his Ph.D. thesis. His work has served as a useful guide throughout this experiment.

I appreciate the active interest that Mark Kasevich and Kurt Gibble have taken in this experiment. They have both provided me with much useful advice and encouragement. I have also enjoyed fruitful discussions with Martin Weitz, Achim Peters, Heun-Jin Lee, Joel Hensley, and Tom Perkins. The numerical simulations of adiabatic passage described here are nearly entirely the work of Martin Weitz. I appreciate all of his planning and work for the switch to adiabatic passage. I would especially like to thank Joel and Achim for their nice work on the vibration isolation system, without which this experiment would not have been possible. Joel has provided invaluable assistance in the lab throughout most of the experimental work reported here. I also thank Ken Sherwin for all of his technical assistance and for his expertise in equipment acquisition.

I acknowledge the support of an NSF predoctoral fellowship from 1989–92, and the NSF and AFOSR for their funding of the experimental work.

Contents

Abstract	iv
Preface	v
Acknowledgements	vi
1 Introduction	1
1.1 Measurements of the fine-structure constant	1
1.2 Photon recoil measurement	3
1.3 Summary of recent improvements	6
1.4 Overview of this thesis	7
2 Theory	9
2.1 Atom interferometry	10
2.1.1 Fundamentals of interferometry	11
2.1.2 Large-area interferometers	16
2.2 Two-photon transitions	18
2.2.1 Stimulated Raman transitions	22
2.2.2 Adiabatic passage	25
2.3 Recoil measurement using atom interferometry	43
3 Experiment	47
3.1 Summary of the experiment	47
3.2 Cesium fountain	51

3.3	Velocity-selective Raman transitions	55
3.3.1	Magnetic fields	56
3.3.2	Adiabatic passage beam generation	59
3.3.3	Vibration isolation	77
3.4	State-selective detection	81
3.4.1	Doppler-free Raman transitions	82
3.4.2	Atom detection	83
3.5	Tests of adiabatic passage	85
3.5.1	Momentum transfer	85
3.5.2	Interferometry	89
4	Results	93
4.1	Recoil frequency shift	93
4.1.1	Data analysis	93
4.1.2	Interferometer fringes	96
4.2	Checks for systematic errors	97
4.2.1	Magnetic-field shifts	98
4.2.2	Detuning from the excited state	100
4.2.3	ac Stark shifts	101
4.2.4	Missed photon kicks	104
4.2.5	Detuning from the Raman resonance	108
4.2.6	Beam misalignment or imperfect collimation	110
4.2.7	Raman beam wave-front distortion	111
4.2.8	Electronic phase shifts	114
4.2.9	General tests for systematic errors	118
4.3	Summary of recoil results	121
4.4	Determination of α	123
5	Future prospects	125
5.1	Short-term improvements	125
5.1.1	Reduction of systematic error uncertainty	125
5.1.2	Improved measurement sensitivity	126

5.1.3	Reducing amplitude noise from adiabatic passage	127
5.1.4	Normalization of the probe signal	128
5.2	Major revisions of the recoil measurement	129
5.2.1	Lower-mass atoms	130
5.2.2	Large-area interferometers	131
	Bibliography	133

List of Tables

3.1	Control waveforms for adiabatic passage atom interferometers	67
4.1	Systematic corrections and error budget for Δf_{rec}	122
4.2	Various quantities needed to relate Δf_{rec} and α	124

List of Figures

1.1 Measurements of α better than 100 ppb	2
1.2 Simplified version of the photon recoil measurement	5
2.1 Recoil diagrams for two atom interferometer geometries	15
2.2 Techniques for increasing momentum transfer	17
2.3 Large-area interferometers with enhanced sensitivity	19
2.4 Three-level atom	20
2.5 Possible field orientations for stimulated Raman transitions	21
2.6 Population transfer using two-photon transitions	24
2.7 Numerical simulations of adiabatic passage for zero detuning	34
2.8 Numerical simulations of adiabatic passage for nonzero detunings	35
2.9 Atom optics using adiabatic passage	38
2.10 Ramsey-Bordé interferometer implemented by adiabatic passage	41
2.11 Two interferometer resonances used in the recoil measurement	45
3.1 Overview of the experimental apparatus	49
3.2 Magnetic-field profile along the atomic trajectory	60
3.3 Adiabatic passage beam generation	62
3.4 Electronics for the adiabatic passage beam phaselock	73
3.5 An active vibration isolation system	79
3.6 The dark state frequency width for adiabatic transfer pulses	88
3.7 Vibration isolation performance for atom interferometry	91
3.8 Enhancement of the interferometer sensitivity with N	92

4.1	Atom interferometer fringes for $T = 120$ ms and $N = 30$	96
4.2	Variation of Δf_{rec} with the one-photon detuning	103
4.3	Errors in Δf_{rec} contributed by $250 \mu\text{s}$ beam-splitter pulses	105
4.4	Cancellation of wave-front phase errors	112
4.5	Reversal of wave-front phase errors with \mathbf{k}_{eff}	113
4.6	Variation of Δf_{rec} with reversals of \mathbf{k}_{eff}	115
4.7	Contributions of electronic phase shifts to the recoil measurement	117
4.8	Variation of Δf_{rec} with T	119
4.9	Variation of Δf_{rec} with N	120
4.10	Data collected during a continuous 4-hour time period	122

Chapter 1

Introduction

1.1 Measurements of the fine-structure constant

Presently the anomalous magnetic moment of the electron $a_e \equiv (g - 2)/2$ provides the most precise determination of the fine-structure constant α , with an uncertainty of 4.2 ppb (parts per billion). This approach equates the experimental value of a_e [1] with the quantum electrodynamics (QED) calculation of a_e as a power series in α [2] to determine a value for α . Consequently, the currently accepted value for α assumes the validity of QED. Improved precision in a QED-independent measurement of α thereby constitutes a test of QED. The goal of this work is a precision measurement of the recoil of an atom caused by the absorption of a photon. This result, when combined with an absolute frequency measurement and mass-ratio measurements, determines a value for α which does not require QED.

The measurements of α , including this work, with precision better than 100 ppb are shown in Fig. 1.1. In addition to the a_e determination, these include measurements based on the quantum Hall effect [3], neutron diffraction [4], and the ac Josephson effect [5] with relative uncertainties of 24 ppb, 39 ppb, and 56 ppb, respectively. These measurements have statistically significant differences between them, and have considerably higher uncertainties than the a_e value, so another independent measurement of α would be of interest. Even the very precise a_e value recently changed 10σ because of a correction to the theory [2].

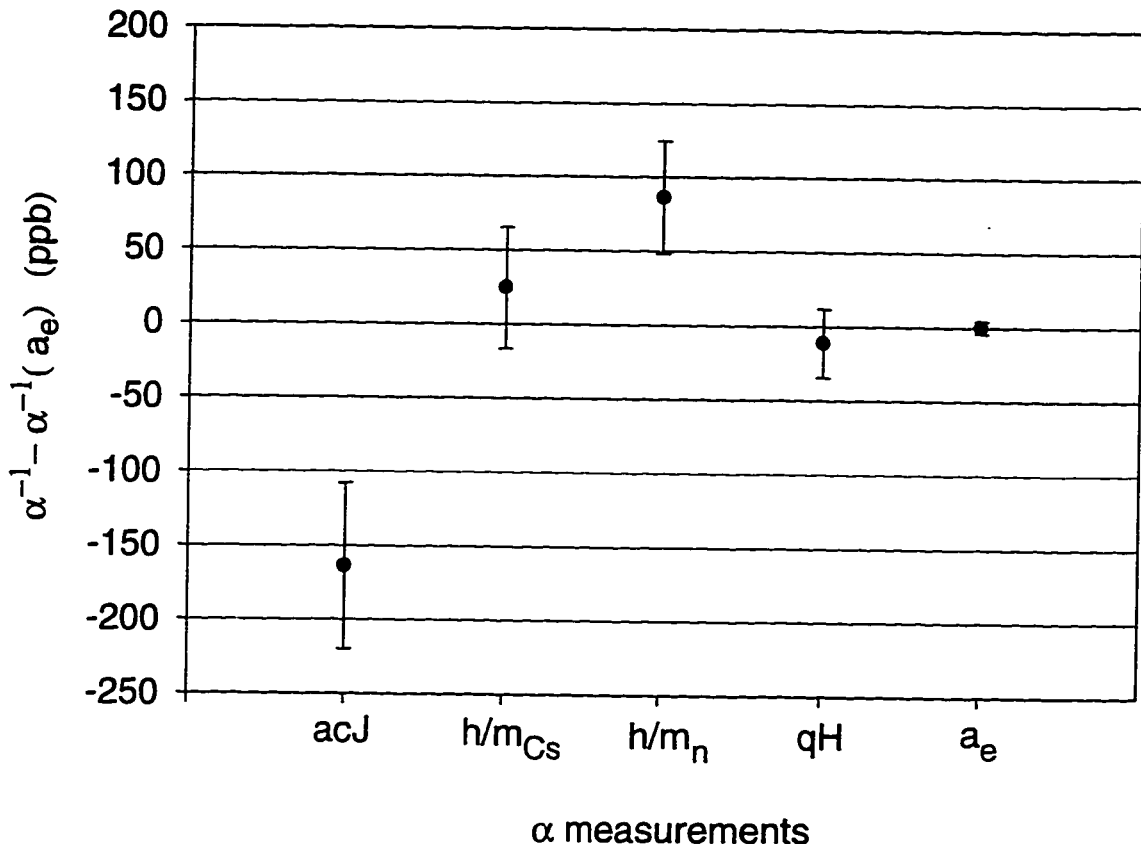


Figure 1.1: Measurements of α better than 100 ppb. The values are plotted relative to $\alpha^{-1}(a_e) = 137.035\,999\,44(57)$ determined from the electron anomalous magnetic moment. These include results from the ac Josephson effect (acJ), this measurement (h/m_{Cs}), neutron diffraction (h/m_n), the quantum Hall effect (qH), and a_e .

Tentatively, our determination of α from the photon recoil measurement has an uncertainty of 56 ppb. Note, however, that the 45 ppb uncertainty of the knowledge of the absolute frequency of the cesium D_1 line is the predominate contributor to the overall uncertainty of the calculation. Anticipated improvements in this absolute frequency measurement could allow this measurement of the photon recoil to provide a value for α with an uncertainty of about 30 ppb.

Some notable distinctions exist among the various QED-independent measurements shown in Fig. 1.1. The quantum Hall effect and ac Josephson effect measurements require the use of electrical definitions, *e.g.*, the calculable capacitor. It is

believed that these measurements may have reached the limit of their precision. The neutron diffraction and photon recoil measurements, on the other hand, are independent of electrical definitions. A good approach for achieving the ultimate precision in a measurement is to frame the experiment as a frequency measurement, since frequencies can be so accurately measured and compared. The neutron diffraction and photon recoil measurements are conceptually very similar—the former measuring h/m_n and the latter h/m_{Cs} . Both approaches use quantum interference of neutral particles, so that they can easily be isolated from perturbing forces, and their interactions with matter are well understood. For neutron diffraction, the interferometer is generated by interactions of the neutrons with silicon crystals, the lattice spacing of which must be calibrated interferometrically. In the photon recoil measurement, the matter-wave interferometers are created by interactions with light fields propagating in vacuum. Accurate stabilization of the laser frequency provides an absolute calibration for the impulses created by the interferometer interactions. Reference [6] provides a comprehensive review of fine-structure constant measurements.

1.2 Photon recoil measurement

In its simplest form, the photon recoil measurement is a determination of the Doppler shift of an atomic resonance caused by the momentum recoil from an absorbed photon. Consider the two-level atomic system of Fig. 1.2(a) with two stable states $|a\rangle$ and $|b\rangle$. If the atom interacts with two counterpropagating, on-resonance fields, as in Fig. 1.2(b), then the difference $\omega_B - \omega_A$ contains a contribution from the momentum recoil of the photon absorbed in the first interaction. Unfortunately, in this simplified measurement, $\omega_B - \omega_A$ also includes a Doppler-shift contribution from the initial velocity of the atom along the direction of the light field. Switching to the differential measurement of Fig. 1.2(c) easily corrects this problem. Here, the first field puts the atom into a superposition of both momentum states. Two resonances exist for the second field frequency ω_B —one for each of the momentum states. The two pairs of

momentum states coupled by ω_B have a velocity difference of

$$\Delta v = \frac{2\hbar k}{m_A}, \quad (1.1)$$

where \hbar is the Planck constant, m_A is the atomic mass, and $k \approx k_A \approx k_B$ is the wave number of the light field. Ignoring the second- and higher-order Doppler shifts, which are insignificant for our experimental parameters, this velocity difference creates a Doppler-shift frequency difference between the two resonances of

$$\Delta f_{\text{rec}} = \frac{k\Delta v}{2\pi} = \frac{2h\nu^2}{m_A c^2}, \quad (1.2)$$

where c is the speed of light and $\nu = ck/2\pi$ is the frequency of the light field.

In our experiment, we precisely measure the frequency shift Δf_{rec} for cesium atoms using light on resonance with the D_1 line. Assuming that ν is known accurately, Eq. (1.2) gives with high precision the ratio

$$\frac{h}{m_{\text{Cs}}} = \frac{c^2 \Delta f_{\text{rec}}}{2\nu^2}. \quad (1.3)$$

We determine α from the photon recoil measurement using the relation

$$\alpha^2 = \frac{2R_\infty}{c} \frac{h}{m_e}, \quad (1.4)$$

where R_∞ is the infinite-mass Rydberg constant and m_e is the electron mass. Since R_∞ is known to 0.028 ppb [7] and c is defined, the uncertainty in the ratio of h/m_e limits the calculation of α from this relation. Expanding Eq. (1.4) using mass ratios, then substituting h/m_{Cs} from Eq. (1.3) gives

$$\begin{aligned} \alpha^2 &= \frac{2R_\infty}{c} \left(\frac{m_p}{m_e} \right) \left(\frac{m_{\text{Cs}}}{m_p} \right) \frac{h}{m_{\text{Cs}}} \\ &= cR_\infty \left(\frac{m_p}{m_e} \right) \left(\frac{m_{\text{Cs}}}{m_p} \right) \frac{\Delta f_{\text{rec}}}{\nu^2}. \end{aligned} \quad (1.5)$$

The proton-electron mass ratio has been measured to 2.2 ppb [8]. The cesium-proton mass ratio is presently known only to 34 ppb [9], but may be improved in the near future to ~ 1 ppb [10]. We stabilize the laser frequency relative to the cesium D_1 line with an accuracy of about 0.3 ppb. The absolute frequency of this transition

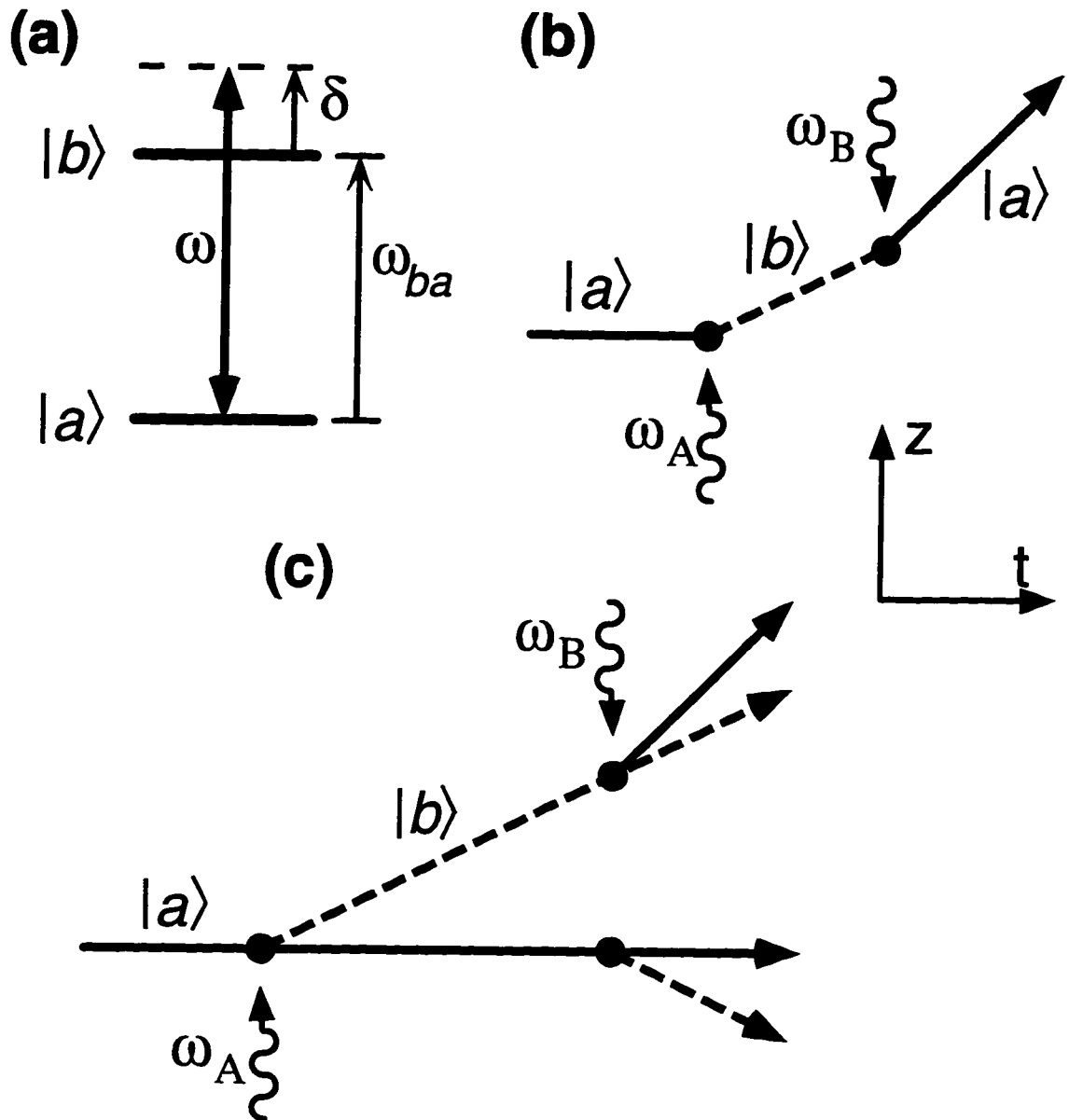


Figure 1.2: Simplified version of the photon recoil measurement. The experiment is performed using the two-level atom in (a). The position of the atom relative to the initial unperturbed trajectory is shown as a function of time. The two field frequencies ω_A and ω_B are centered on resonance. (b) The difference $\omega_B - \omega_A$ includes a contribution from the momentum recoil caused by the absorption of a photon from the first interaction. (c) A simple modification converts this into a differential measurement which cancels out the contribution from the initial atomic velocity.

is presently known to 45 ppb [11], but it soon may be measured to better than 1 ppb [12]. Consequently, an accurate measurement of Δf_{rec} could determine α with an uncertainty eventually approaching 1 ppb.

The fundamental physics of our measurement is essentially identical to the simple picture of Fig. 1.2(c), which makes the basic physical assumptions that the photon momentum is $\hbar k$ and that energy and momentum are conserved. We make two enhancements beyond the simple picture described here. First, we replace the single-photon transitions with two-photon transitions to avoid problems caused by spontaneous emission, as I will describe in Sec. 2.2. This modification has the effect of replacing ν in Eqs. (1.2)–(1.5) with $\nu_{\text{eff}} = \nu_1 + \nu_2$. Secondly, to improve the accuracy of our measurement of the resonance centers, we replace each of the two paths of Fig. 1.2(c) with an atom interferometer, as will be described in Sec. 2.3. The only effect of this change on Eqs. (1.2)–(1.5) is that certain interferometer geometries increase the number of photon recoils measured, thereby increasing Δf_{rec} by a known integer multiplier.

1.3 Summary of recent improvements

The initial version of this experiment [13, 14, 15] was the first attempt to use the new field of atom interferometry for a precision measurement of a fundamental physical constant. In that experiment, we obtained a maximum resolution of 100 ppb in α from two hours of data. Unfortunately, systematic errors limited the measurement at the 1 ppm level. Instead of tracking down the systematic errors at that time, we made major changes to both reduce several suspected systematic errors, and also boost the resolution of the measurement. These changes, which will be described in greater detail throughout the remainder of this thesis, will be briefly summarized in the remainder of this section. The goals of these changes include improved vibration isolation, reduced magnetic-field shifts, longer interferometer interaction times, more efficient atomic state transfers, smaller errors from wave-front phase distortions, and reduced ac Stark shifts.

Previously, horizontal laser beams delivered the interferometer pulses. In that

geometry, gravity did not shift the transitions, so the laser frequencies only required modest shifts of about 200 kHz to account for photon recoils. Additionally, a simple air rail provided adequate vibration isolation to below 1 Hz. Unfortunately, however, the short time the atoms remained near the center of the 2-cm diameter laser beams limited the total interferometer interaction time to about 50 ms. Also, generating a uniform bias field over the trajectory is difficult with large diameter horizontal beams. In the present measurement, the Raman beams propagate vertically through cylindrical magnetic shields. With vertical beams the atoms remain in the beam and the magnetic field is sufficiently uniform to guarantee quadratic Zeeman shift errors below 1 ppb for interaction times as long as 400 ms. The vertical geometry also allows partial cancellation of wave-front phase errors since the atoms stay at nearly the same radial positions in the beams for all of the interferometer pulses.

In the first version of the experiment, the atomic states were changed using stimulated Raman transitions with the two lasers detuned about 2 GHz from the excited state. Now we implement the atom interferometers using adiabatic passage, for the reasons given in Section 2.2.2. We have achieved 93% transfer efficiency using adiabatic transfer, as compared to the 85% transfer efficiency we previously obtained with far-detuned Raman transitions. With this higher efficiency, we can add twice as many transfer pulses for the same loss of atoms.

With these changes in place, we have achieved over an order-of-magnitude increase in the sensitivity of the measurement. We now typically obtain a resolution in α of 100 ppb in 1 minute instead of 2 hours. Judging by better consistency of $(\Delta f_{\text{rec}})_{\text{exp}}$ with various changes of experimental parameters, we also have significantly reduced the size of the systematic errors. Our determination of α presently agrees with the a_e measurement to within the uncertainty of the cesium D_1 line transition frequency.

1.4 Overview of this thesis

Chapter 2 develops the theory required to understand the photon recoil measurement. First I give an overview of atom interferometry for the case of single-photon

transitions. Then I generalize to two-photon transitions, including stimulated Raman transitions and adiabatic passage. Finally I consider the special case of the interferometer geometries used for the photon recoil measurement.

Chapter 3 describes the experimental apparatus. The cold atom preparation is similar to that of the first generation measurement [15], so I cover it relatively briefly. I focus mainly on the newer features of the experiment such as the Raman beam generation, the interferometer pulse sequence timing, the active vibration isolation system, the magnetic shielding, and the state-selective detection using Doppler-free Raman transitions.

I present the results of the photon recoil measurement in Chapter 4, starting with a description of the data collection and analysis procedures. Then I discuss the various anticipated sources of systematic errors, the limitations they place on the measurement accuracy, and the experimental parameters that we varied in our search for possible problems. After summarizing the recoil measurement results, I present a value for the photon recoil shift and calculate from it a value for α .

Chapter 5 covers the future prospects for this measurement, including both near-term improvements that may reduce systematic errors or boost the signal-to-noise, and larger-scale changes for the next generation measurement.

Chapter 2

Theory

The simplified version of the photon recoil measurement presented in Chapter 1 accurately describes the basic physics of the experiment, but would not in practice provide the precision required for an improvement in α . In that example, we measure the difference between the centers of two resonances separated by Δf_{rec} . For our atomic system, $\Delta f_{\text{rec}} \approx 30 \text{ kHz}$. A 10 ppb measurement of α requires a 20 ppb measurement of Δf_{rec} , or $600 \mu\text{Hz}$. Suppose that we are performing the experiment using cesium atoms laser cooled to about $4 \mu\text{K}$, corresponding to a 70 kHz Doppler-width of the two-photon transition. We could conceivably use long, low-intensity pulses to give transition lineshapes with widths $\sim 1 \text{ Hz}$. In doing so, however, we would be addressing only 0.001% of the atoms. Since we still would need to measure the resonance centers to about 10^{-3} , this reduction of signal could severely increase the difficulty of the measurement. One of the great advantages of atom interferometry is that it allows the use of short, intense light pulses that address a broad velocity distribution, but separates the pulses by long free-evolution periods that create narrow interference fringes. Consequently, we can accurately locate the resonance centers, but without decimating the atom signal.

In this chapter I present the theoretical background necessary to understand the atom interferometry used for the photon recoil measurement. First I establish the formalism for the quantum mechanical description of atom interferometry, using the physical system of a two-level atom with no spontaneous emission. I also introduce

the pictorial representation of atom interferometers that will be used throughout the remainder of this thesis. To avoid the devastating effects of spontaneous emission in electric-dipole transitions and to ease the requirements on the laser frequency stability, I next generalize to the case of two-photon transitions between metastable energy states. Possible two-photon interactions include stimulated Raman transitions and adiabatic passage. With this background, I can then discuss the particular atom interferometers used for the photon recoil measurement.

2.1 Atom interferometry

Two demonstrated approaches to atom interferometry exist. In analogy to optical interferometers, slits or diffraction gratings can split and recombine beams of atoms. Experiments have employed both material structures and periodic light fields to diffract atomic wave packets. The alternative approach, which I will be discussing throughout the remainder of this chapter, is to generate atomic interference of internal states. In this class of interferometers, an electromagnetic field drives atoms between two internal states of either a two-level system as in Fig. 1.2(a) or an effective two-level system. The interference manifests itself in the relative populations of states $|a\rangle$ and $|b\rangle$ at the output of the interferometer.

The earliest example of an interferometer based on the interference of internal states is Ramsey's separated oscillatory field method [16], although Bordé only recently interpreted it as an atom interferometer [17]. In this technique, an initial pulse of microwave radiation puts an atom into a superposition of two internal states. The atom then freely evolves for a while before being exposed to a second pulse. If the atomic superposition state is in phase with the microwave field for the second pulse, then the atom completes the transition from the initial to the final state. This is the interrogation technique applied for cesium atomic clocks.

The photon recoil measurement strongly favors transitions using optical rather than microwave photons because of their larger momentum transfer and higher Doppler sensitivity. The absorption of an optical photon simultaneously changes an atom's internal and momentum states. Consequently, putting an atom into a superposition

of two internal states causes the atomic wave packet to spatially separate. A requirement for atomic interference is that the two internal states of the atom must spatially overlap during the time of the final pulse. The original Ramsey method only needed two pulses to achieve interference since the spatial separation caused by a microwave photon is negligible compared with the spatial coherence of the atomic source. Generalizing the Ramsey technique to the optical regime requires additional field interactions for redirecting and overlapping the atomic wave packets.

I will discuss here on a particular class of internal state atom interferometers which uses light pulses for momentum transfer, focusing mostly on the issues that relate to the photon recoil measurement. I will discuss other interferometer geometries to the level needed to understand the powers and limitations of atom interferometry using adiabatic passage, which is one of the major developments in this work. A more complete development of light-pulse atom interferometers is presented in Ref. [18].

2.1.1 Fundamentals of interferometry

One approach to analyzing atom interferometers is to consider explicitly the propagation of spatial wave packets. In this approach, the interferometer phase shifts are calculated using a set of phase-shift rules for the atom-light interaction points and for the free-space propagation time. Free propagators and S matrices (including variable transit times and second-order Doppler shifts for both standing- and traveling-wave interactions) are described in Ref. [19]. Those general results are particularly useful for the case of a beam of atoms passing through cw laser beams. For pulsed-light interferometers with cold atoms, the interaction time is the same for all atoms and second-order Doppler shifts are generally insignificant, so simpler rules apply [20, 21]. One useful generalization of these rules is to account for ac Stark shifts in two-photon transitions [15].

Rather than develop a wave-packet description of the atomic trajectories, we begin with a quantum treatment where the atomic wave packets are taken to be the sum of momentum plane-wave states. After calculating the effect of the atom-field interactions for a given plane-wave component, we could determine the behavior of the

original wave packet by integrating over all of the momentum states in the atomic ensemble. For determining the phase shifts in atom interferometers, however, this final integration is often unnecessary.

For atom interferometry with optical photons, the entanglement of internal and momentum states implies that the position of the atoms is not a classical variable. Consequently, the basis for atomic states is a tensor product of the Hilbert space describing the internal energy state of the atom and the Hilbert space describing the external degrees of freedom,

$$\begin{aligned} |a, \mathbf{p}_a\rangle &= |a\rangle \otimes |\mathbf{p}_a\rangle \\ |b, \mathbf{p}_b\rangle &= |b\rangle \otimes |\mathbf{p}_b\rangle \end{aligned} \quad (2.1)$$

The Hamiltonian for this system is

$$\hat{H} = \frac{\hat{\mathbf{p}}^2}{2m} + \hbar\omega_a|a\rangle\langle a| + \hbar\omega_b|b\rangle\langle b| + \hbar\Omega, \quad (2.2)$$

where $\hat{\mathbf{p}}$ operates on the momentum portion of the basis states. The Rabi frequency

$$\Omega \equiv -\mathbf{d} \cdot \mathbf{E}/\hbar \quad (2.3)$$

contains the spatial dependence of the electric field

$$\mathbf{E} = \mathbf{E}_0 \cos(\mathbf{k} \cdot \mathbf{x} - \omega t + \phi). \quad (2.4)$$

The operator $e^{i\mathbf{k} \cdot \mathbf{x}}$ in \mathbf{E} can be rewritten with the closure relation

$$\begin{aligned} 1 \cdot e^{\pm i\mathbf{k} \cdot \mathbf{x}} &= \int d^3\mathbf{p} e^{\pm i\mathbf{k} \cdot \mathbf{x}} |\mathbf{p}\rangle\langle \mathbf{p}| \\ &= \int d^3\mathbf{p} |\mathbf{p} \pm \hbar\mathbf{k}\rangle\langle \mathbf{p}|. \end{aligned} \quad (2.5)$$

The spatial dependence of the electric field in the momentum basis yields the well known result: the absorption or emission of a photon of wave vector \mathbf{k} changes the atom's total momentum by an amount $\hbar\mathbf{k}$. This one-to-one correspondence between the internal and external degrees of freedom implies that the basis states simplify to $|a, \mathbf{p}\rangle$ and $|b, \mathbf{p} + \hbar\mathbf{k}\rangle$. The detuning from resonance for this effective two-level system,

$$\delta \equiv \omega - \left(\omega_{ba} + \frac{\mathbf{p} \cdot \mathbf{k}}{m} + \omega_{\text{rec}} \right), \quad (2.6)$$

contains terms corresponding to the Doppler shift $\mathbf{p} \cdot \mathbf{k}/m$ and the recoil shift $\omega_{\text{rec}} = \hbar k^2/2m = \Delta f_{\text{rec}}/4\pi$.

To introduce some terminology to be used throughout the rest of this thesis, consider the special case of detuning $\delta = 0$. Suppose that an atom is initially in state $|a, \mathbf{p}\rangle$ when the optical field turns on with constant field strength \mathbf{E}_0 . Then the occupation probability of the atom begins oscillating sinusoidally between $|a, \mathbf{p}\rangle$ and $|b, \mathbf{p} + \hbar\mathbf{k}\rangle$ at frequency Ω , a process known as Rabi flopping. If the light turns off after a time $\tau_\pi = \pi/\Omega$, then the atom is completely transferred to $|b, \mathbf{p} + \hbar\mathbf{k}\rangle$. This is called a π pulse. Similarly, a $\pi/2$ pulse of duration $\tau_{\pi/2} = \pi/2\Omega$ leaves the atom in a coherent superposition of the two states. Many atom interferometers are simple combinations of $\pi/2$ and π pulses.

When a $\pi/2$ pulse puts an atom into a coherent superposition of its two internal states, the recoil causes the parts of the atom in the two states $|a, \mathbf{p}\rangle$ and $|b, \mathbf{p} + \hbar\mathbf{k}\rangle$ to begin separating at a velocity $\mathbf{v}_{\text{rec}} = \hbar\mathbf{k}/m$. If these two wave packets are to interfere at some later time, they must be made to spatially overlap. If optical photons are used in an atomic fountain, the recoil distance can approach 1 cm, which is much larger than the spatial coherence of the atomic source. In these cases, interference will not occur unless the parts of the atom separated during the $\pi/2$ pulse recombine at some later time. Since the momentum basis states $|\mathbf{p}\rangle$ are spatially delocalized, the above formalism does not account for nonoverlapping wave packets until we make an explicit sum over a superposition of momentum states.

Recoil diagrams are convenient tools for verifying spatial overlap in atom interferometers. A recoil diagram is a plot versus time of the center “position” of an atomic wave packet relative to an inertial frame freely falling along the initial unperturbed trajectory of the atom. Consequently, the diagram does not include any motion caused by gravity nor any spreading of the wave packet caused by pulses of nonzero duration. Atom-light interactions create vertexes in the plot at which paths split or deflect because of momentum transfer from the light field. If two or more paths overlap at any interaction point, then interference occurs on the output of that interaction provided that the momentum transferred causes two or more input paths to contribute to a single output path. Besides providing a clear picture of spatial

overlap of wave packets, recoil diagrams also provide a visual gauge of the sensitivity of atom interferometers to conservative potentials such as gravity. References [20] and [21] provide the theoretical basis of and practical uses for recoil diagrams. Figures 1.2(b) and (c) contain simple examples of recoil diagrams, and many more will appear in the following discussions of various atom interferometer geometries. In summary, we can correctly calculate atom interferometer phase shifts using only momentum basis states, without explicitly summing over the superposition of states in the wave packet, as long as we check the the recoil diagram for spatial overlap.

The simplest optical pulse atom interferometer that achieves spatial overlap is the $\pi/2 - \pi - \pi/2$ pulse sequence shown in Fig. 2.1(a). It was first demonstrated in the atom interferometer measurement of g [22, 23]. If an atom is in resonance with the light field, then the first $\pi/2$ pulse acts as a beam splitter, introducing a velocity difference $v_{\text{rec}} = \hbar k/m$ between the two states. After a time T , the π pulse acts as a mirror and redirects the wave packets so that they overlap at the time $2T$ of the second $\pi/2$ pulse. Even if the inhomogenous velocity distribution is sufficiently broad that the spectral width of the π pulse ($\delta\omega \simeq 1/\tau$) is less than the Doppler-broadened linewidth, atoms partially in resonance with the laser will receive the same momentum transfer and register the same net interferometer phase shift for this pulse sequence.

A pulse sequence consisting of one pair of $\pi/2$ pulses followed by a pair of oppositely directed $\pi/2$ pulses is another pulse scheme used to redirect the trajectories of the atoms [24, 25]. This pulse sequence was originally used to extend the Ramsey separated oscillatory field technique to the optical domain, and the interpretation of the experiment in terms of an atom interferometer with separated wave packets followed eight years later [26]. This is the pulse sequence that we used in the first generation photon recoil measurement [14, 15]. The atomic trajectories for this type of interferometer are shown in Fig. 2.1(b). The geometry of the atom interferometer that we use in this round of experimentation is identical, but instead of Raman π and $\pi/2$ pulses, we use adiabatic passage pulses, as will be described in Secs. 2.2.2 and 2.3.

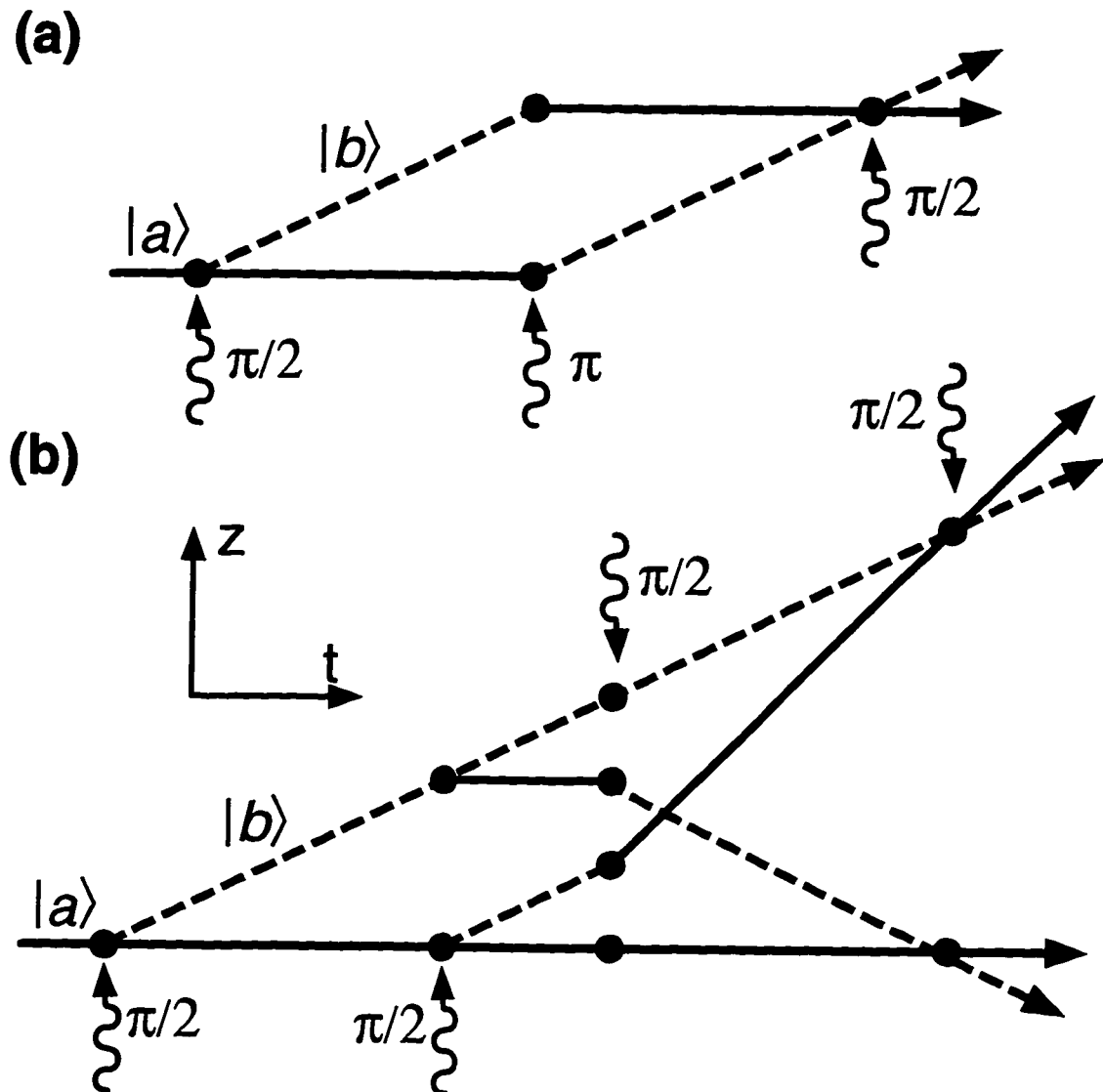


Figure 2.1: Recoil diagrams for two atom interferometer geometries. The vertical axis is the position z of an atom relative to a reference frame freely falling along the initial trajectory of the atom. Solid and dashed lines indicate paths for which the atom is in $|a\rangle$ and $|b\rangle$, respectively. The vertices are points of interaction with light pulses, with k indicated by the direction of the arrows. (a) The $\pi/2 - \pi - \pi/2$ geometry used for the g measurement. (b) The Ramsey-Bordé sequence used for the photon recoil measurement. Note that the orientation of k is reversed for the second pair of $\pi/2$ pulses. Noninterfering paths are omitted.

2.1.2 Large-area interferometers

The sensitivity of atom interferometers can be enhanced by using multiple-pulse sequences to create large momentum differences between interferometer paths. For example, in the case of Sagnac-effect gyroscopes, sensitivity scales linearly with the area enclosed by the two interferometer arms, so that larger momentum differences produce larger areas (all else the same). In the case of a gravimeter, sensitivity increases linearly with wave-packet separation (for fixed T), so again larger momentum recoil implies greater sensitivity. For this interferometer, the geometric area is zero, but the linear enhancement of sensitivity with area can be seen if the area is measured on the recoil diagram of Fig. 2.1(a). In this sense, such interferometers can be referred to as “large-area” interferometers.

Figure 2.2(a) illustrates a sequence of pulses that can replace a single π pulse, but provide larger momentum transfer. Consider an atom initially in $|a, p\rangle$. A first π pulse transfers the atom to $|b, p + \hbar\mathbf{k}\rangle$. Next, a π pulse with reversed propagation vector $-\mathbf{k}$ stimulates the atom back to its ground state, but now with momentum $\mathbf{p} + 2\hbar\mathbf{k}$. Additional pulses, with alternating propagation directions, may be used in a similar manner to increase the momentum transfer. A sequence of N such π pulses transfers momentum $N\hbar\mathbf{k}$ to the atom. Note that when the Rabi frequency is less than the recoil shift, the frequency of the driving light field must be switched to maintain the resonance condition. We have transferred the momentum from up to 200 optical photons in this manner (see Sec. 3.5.1). Replacing the first π pulse in Fig. 2.2(a) with a $\pi/2$ pulse, as in Fig. 2.2(b), creates a beam splitter with increased momentum transfer. (We assume here that the Rabi frequency is chosen smaller than the recoil frequency shift so that the driving field is resonant with just one of the two wave packets.)

The sequences of pulses in Fig. 2.2 can be applied to improve the momentum transfer of the $\pi/2$ and π pulses in the three- and four-pulse interferometer sequences described above. For example, Fig. 2.3(a) shows a Ramsey-Bordé interferometer with $\mathbf{k}_{\text{eff}} \rightarrow 2\mathbf{k}_{\text{eff}}$ by using the pulse sequences of Fig. 2.2. Note that the middle two $\pi/2$ pulses can be replaced with π pulses because the lasers can independently address the two interferometer arms. This eliminates the noninterfering paths in

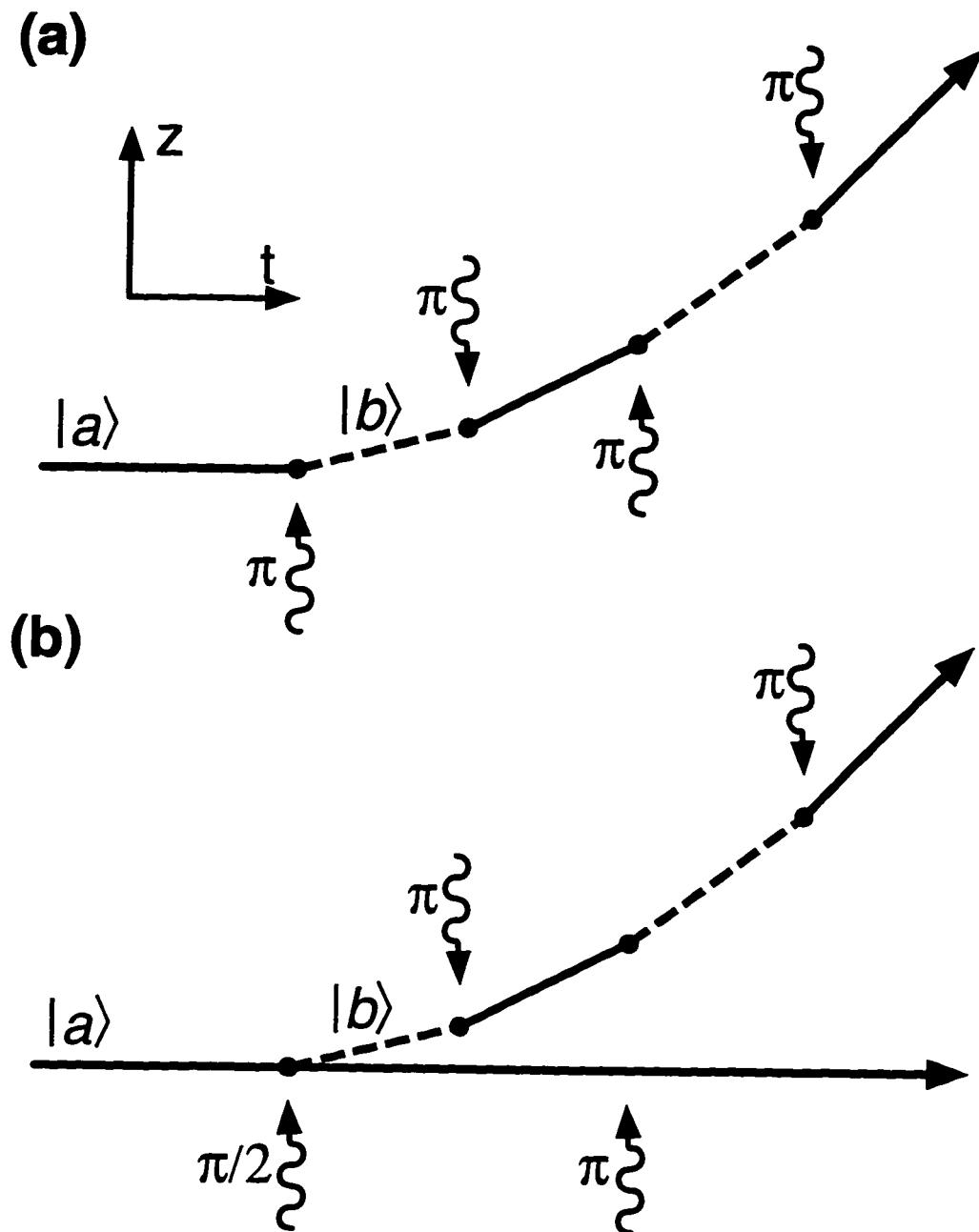


Figure 2.2: Techniques for increasing momentum transfer. The sensitivities of atom interferometers constructed with π and $\pi/2$ pulses can be enhanced by replacing each pulse with a sequence of pulses with greater momentum transfer. (a) An effective π pulse or mirror. (b) An effective $\pi/2$ pulse or beam splitter. We assume that $\Omega < \omega_{\text{rec}}$ so that the laser can be tuned to deflect only one of the two paths.

the standard Ramsey-Bordé interferometer. In general, the addition of N pulses for each interaction causes the transformation $\mathbf{k}_{\text{eff}} \rightarrow (N + 1)\mathbf{k}_{\text{eff}}$, which increases the interferometer phase sensitivity by a factor of $(N + 1)^2$. I will describe the operation of this interferometer in greater detail in Sec. 5.2.2.

Figure 2.3(b) shows another enhanced version of the basic Ramsey-Bordé interferometer that I will refer to as a modified Ramsey-Bordé interferometer. It includes additional π pulses between the central two $\pi/2$ pulses. This increases the interferometer sensitivity by a factor of only $N+1$ instead of $(N+1)^2$. For practical experimental reasons, however, this is the interferometer geometry used in the present experiment.

2.2 Two-photon transitions

Atom interferometry with high sensitivity to velocity changes, such as we desire here, strongly prefers optical photons over microwave photons. On the other hand, the implementation of an interferometer requires an atomic level scheme where both states are stable against radiative decay for the duration of the pulse sequence. With laser-cooled atomic sources the available interaction time with a single collection of atoms can approach 1 s, which far exceeds the lifetime of electric-dipole transitions. Furthermore, if we were to use a forbidden optical transition, then the optical frequency of the laser must be stable to well below 1 Hz for this interaction time, which is difficult to achieve. To fully utilize the available interaction time, while reducing the requirements on the laser stability, we replace the single-photon transitions with two-photon transitions between metastable atomic states. Consider the three-level atom in Fig. 2.4 consisting of two metastable states $|a\rangle$ and $|b\rangle$ with microwave splitting ω_{ba} and an excited state $|i\rangle$ with decay rate Γ . Two fields at optical frequencies ω_1 and ω_2 drive the atom. Since this two-photon transition only depends sensitively on the difference frequency $\omega_1 - \omega_2$, we no longer need ultra-stable control of the optical frequencies of the lasers—only the difference frequency.

The relative orientation of the field propagation vectors \mathbf{k}_1 and \mathbf{k}_2 determines the momentum delivered by the transition, and simultaneously, the velocity sensitivity of

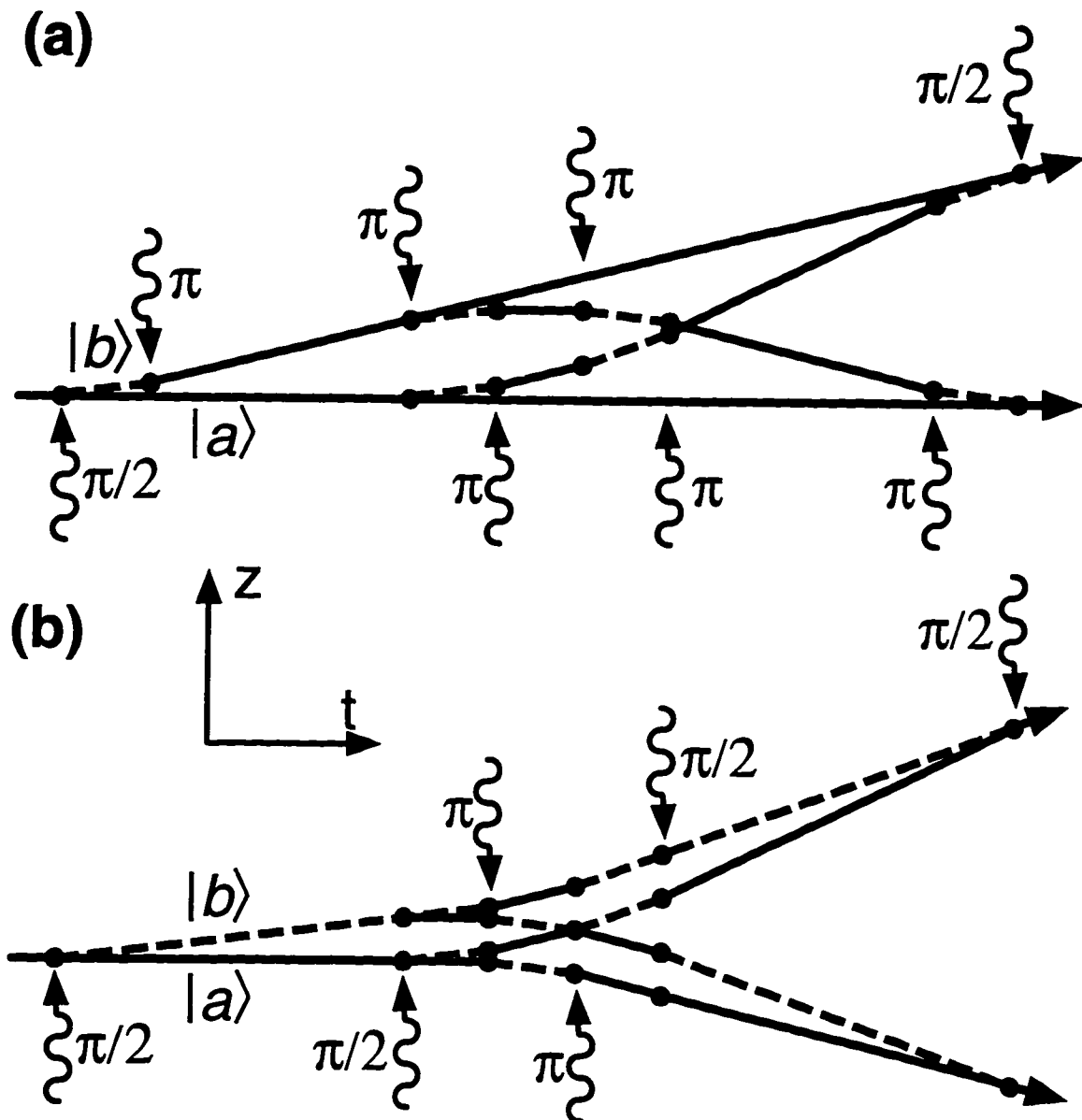


Figure 2.3: Large-area interferometers with enhanced sensitivity. (a) Ramsey-Bordé interferometer with $k_{\text{eff}} \rightarrow 2k_{\text{eff}}$. The orientations of k_{eff} are shown for the upper interferometer. For the lower interferometer, k_{eff} must be reversed for all pulses after the first two. (b) Modified Ramsey-Bordé interferometer geometry used for the photon recoil measurement. Adding $N = 2 \pi$ pulses between the pairs of $\pi/2$ pulses increases Δf_{rec} by a factor of $(N + 1) = 3$.

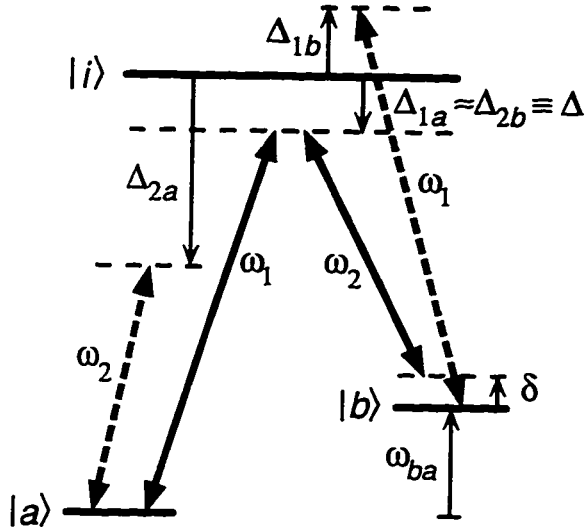


Figure 2.4: Three-level atom. Two light fields at frequencies ω_1 and ω_2 couple metastable states $|a\rangle$ and $|b\rangle$ via the intermediate state $|i\rangle$. The one- and two-photon detunings are Δ and δ , respectively. The interactions of ω_1 and ω_2 with the wrong levels (dashed arrows) cause additional ac Stark shifts.

the transition. For copropagating fields, as in Fig. 2.5(a), the recoil caused by the absorption of a photon from one field nearly cancels the recoil from stimulated emission of a photon into the other field, leaving only the recoil from a microwave photon at ω_{ba} . As a simple consequence of the conservation of energy and momentum, a small recoil also implies low velocity sensitivity: the Doppler shifts are nearly identical for the two beams, leaving again only the Doppler-shift and recoil shift for a microwave photon at ω_{ba} . These Doppler-free Raman transitions work well for transitions that should be sensitive to the internal state of the atom, but not the momentum state. For example, we use Doppler-free Raman transitions for the final internal-state selective detection to eliminate atoms in undesired ground-state sublevels, as described in Sec. 3.4.1. Alternatively, if the fields are counterpropagating, as in Fig. 2.5(b), then the transition produces the momentum recoil and velocity sensitivity of two optical photons. We use this Doppler-sensitive configuration for all of the interferometer pulses, where we desire large recoils and high velocity sensitivity. In fact, since the recoil frequency shift Δf_{rec} is proportional to the product of the momentum recoil

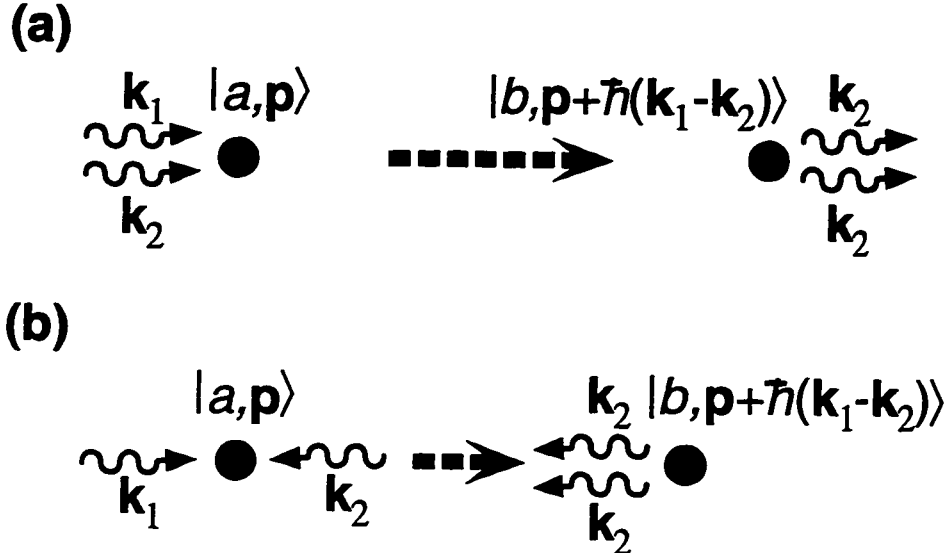


Figure 2.5: Possible field orientations for stimulated Raman transitions. (a) The fields copropagate ($\mathbf{k}_2 \approx \mathbf{k}_1$) for Doppler-free transitions, and (b) counterpropagate ($\mathbf{k}_2 \approx -\mathbf{k}_1$) for Doppler-sensitive transitions.

and velocity sensitivity of the transition, switching to this two-photon transition gives a fourfold increase in Δf_{rec} .

For both Doppler-free and Doppler-sensitive Raman transitions, replacing the two photons with a single effective photon with propagation vector

$$\mathbf{k}_{\text{eff}} \equiv \mathbf{k}_1 - \mathbf{k}_2. \quad (2.7)$$

correctly determines both the momentum recoil and Doppler-sensitivity of the transition. Consequently, all of the recoil diagrams and interferometer results presented in this thesis apply equally well for stimulated Raman transitions as for single-photon interactions if the direction of the photon is interpreted as the orientation of \mathbf{k}_{eff} . Absorption of an effective photon then means the absorption of a photon from field ω_1 , and a stimulated emission into field ω_2 . A stimulated emission of an effective photon represents the reverse process.

In our experiment using cesium, we use the ground-state hyperfine clock transition $6S_{1/2}$, $F = 3$, $m_F = 0 \leftrightarrow F = 4$, $m_F = 0$, which has a lifetime much longer than our interaction time. Since the transition is in the microwave regime, it is easy to experimentally achieve accurate control of the difference frequency by techniques

described in Sec. 3.3.2. In addition, the transition is magnetic-field insensitive, so that the atoms are easily isolated from the perturbing effects of stray magnetic-field gradients (which would give rise to spurious noninertial forces on the atomic wave packet). The two-photon Raman transition using the 894.6 nm cesium D_1 line causes a velocity kick of about 0.67 cm/s. The Doppler sensitivity of 22.4 kHz/(cm/s) is nearly five orders of magnitude larger than that of the single-photon microwave transition.

I discuss in this section two possible techniques for driving these two-photon transitions. Both methods pertain to the three-level atom in Fig. 2.4. The main distinction between the two approaches is the manner in which they avoid spontaneous emission. In the first case, which I refer to simply as stimulated Raman transitions, spontaneous emission is avoided by selecting $\Delta \gg \Gamma$, so that the probability of excitation into the excited state is negligible. The other process, adiabatic passage, has both beams tuned directly on resonance ($\Delta = 0$), yet avoids spontaneous emission by quantum interference between the probabilities of excitation into $|i\rangle$, as will be described in Sec. 2.2.2.

2.2.1 Stimulated Raman transitions

First consider the far-detuned limit $\Delta \gg \Gamma$ with counterpropagating fields $\mathbf{k}_2 \approx -\mathbf{k}_1$. In this case, the intermediate level can be adiabatically eliminated from the interaction picture Schrödinger equations and the dynamics of the three-level system reduces to that of a two-level system. In the first version of the photon recoil measurement, we used stimulated Raman transitions with the two lasers detuned about 2 GHz from the cesium $6P_{3/2}$ excited state. Consequently, this system was analyzed in detail [15], including the ac Stark shifts from the couplings shown with dashed lines in Fig. 2.4.

In this experiment far-detuned Raman transitions were not used for the sensitive interferometer transitions, so I merely summarize simplified results from this earlier work. The essential conclusions are as follows:

1. In certain regimes the three-level system can be viewed as a two-level system

coupled with an effective Rabi frequency

$$\Omega_{\text{eff}} = \frac{\Omega_1^* \Omega_2}{\Delta}. \quad (2.8)$$

2. The internal state of the atom is correlated with its momentum.
3. The two-photon Raman excitation can be modeled by a traveling-wave excitation of frequency

$$\omega_1 - \omega_2 \simeq \omega_{ba} \quad (2.9)$$

and effective propagation vector

$$\mathbf{k}_{\text{eff}} \equiv \mathbf{k}_1 - \mathbf{k}_2 \approx 2\mathbf{k}_1. \quad (2.10)$$

Implementation of these transitions for light-pulse atom interferometry involves simultaneously pulsing on both fields as shown in Fig. 2.6(a). While the fields are both on, the atom Rabi flops between its metastable levels $|a\rangle$ and $|b\rangle$ at rate Ω_{eff} , similarly to a two-level atom. Square pulses of duration $\tau_{\pi/2} = \pi/2\Omega_{\text{eff}}$ and $\tau_\pi = \pi/\Omega_{\text{eff}}$ create $\pi/2$ and π pulses, respectively. Replacing the square pulses with Blackman pulses reduces the wings of the velocity distribution of transferred atoms [15].

The first light-pulse atom interferometers were constructed using stimulated Raman transitions. The initial version of the photon recoil measurement was limited by two disadvantages of far-detuned Raman transitions. First, $\pi/2$ and π pulses are quite sensitive to spatial nonhomogeneity of the laser beams and to laser intensity fluctuations. Secondly, ac Stark shifts can make sizable contributions to the atom interferometer phase. As mentioned in Section 2.1.2, several atom interferometer experiments have sensitivities that can be greatly enhanced by applying multiple light pulses to deliver a large number of photon recoils. Unfortunately, adding more pulses also increases the sensitivity of the interferometer to intensity variations. An alternative technique for changing the states of atoms is adiabatic passage. It has advantages over stimulated Raman transitions which include less intensity sensitivity and smaller ac Stark shifts, so it has good prospects for improving certain atom interferometry experiments.

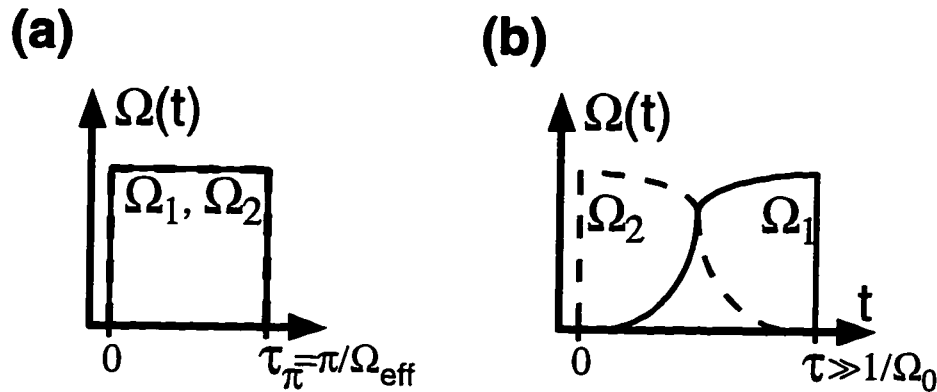


Figure 2.6: Population transfer using two-photon transitions. (a) For stimulated Raman transitions, the beams turn on and off simultaneously. The atom Rabi flops between $|a\rangle$ and $|b\rangle$ while the light is on. The light intensity and pulse duration determine the final state of the system. A π pulse of duration π/Ω_{eff} will transfer the atom either from $|a\rangle$ to $|b\rangle$ or vice versa. (b) For adiabatic transfer, a time delay separates the pulses at frequency ω_1 and ω_2 . This pulse sequence transfers the atom from $|a\rangle$ to $|b\rangle$. To achieve the reverse transfer, the pulse sequence must be time-reversed.

First consider the sensitivity of stimulated Raman transitions to laser intensity nonhomogeneities and fluctuations. Since $\Omega_{\text{eff}} = \Omega_{\text{eff}}(x)$ for real laser beams, the π pulse condition $\tau_\pi = \pi/\Omega_{\text{eff}}$ cannot be simultaneously met for atoms at all locations in the beam. This limits the transfer efficiency for a cloud of atoms of nonzero extent. In the first version of the photon recoil experiment, up to 15 π pulses enhanced the size of the measured recoil. The observed transfer efficiency per pulse was limited to about 85% by spatial variations in the beam intensity. Increasing the laser beam waist reduces this problem, but also decreases the Rabi frequency (for fixed laser power), which reduces the atom signal size for typical experimental parameters. Fluctuations of the beam intensities also cause deviations from the desired π pulse condition. For small fluctuations, the atom loss is second order in the fractional intensity noise, but if several pulses are applied, it can still become a significant noise source unless the laser intensities are actively controlled. The most pernicious effects of intensity fluctuations, however, involve ac Stark shifts.

With stimulated Raman transitions, ac Stark shifts can make sizable contributions

to the atom interferometer phase. Typically, the ac Stark shift of the two-photon transition Ω^{AC} is of the same size as the effective Rabi frequency Ω_{eff} [15]. Consequently, for a single π pulse, the ac Stark shift can cause a phase shift $\sim \pi$. Since the goal of the experiment is the measurement of phase shifts to about 0.1% of a cycle, this ac Stark shift must be canceled exquisitely. Two techniques can reduce the contributions of ac Stark shifts [15]. First, in interferometer measurements, the ac Stark shift often cancels for homogeneous fields. Secondly, the average Stark shift can generally be zeroed by properly adjusting the ratio of beam intensities and the single-photon detuning. Unfortunately, the phase shift remains linearly sensitive to intensity variations and nonhomogeneities around the set values. For example, a possible source of systematic error in the first recoil measurement was the ac Stark shift caused by standing waves. The average ac Stark shift had been zeroed in this experiment, but the presence of standing waves caused a strong modulation of the ac Stark shift along the direction of the beam, which caused a systematic shift of the interferometer phase. Proper selection of polarizations eliminated most of this shift, but some remnant probably persisted from imperfect polarizations. Along with wave-front phase errors, ac Stark shifts was likely one of the main contributors to the 800-ppb discrepancy between the measured recoil and the accepted value [15].

2.2.2 Adiabatic passage

An alternative process that reduces both the sensitivity to beam intensities and the magnitude of the ac Stark shift is stimulated Raman adiabatic passage [27, 28, 29, 30]. In adiabatic passage, time-delayed, on-resonant light fields efficiently transfer atoms between two states. The atoms adiabatically follow an eigenstate of the atom-field interaction Hamiltonian that is not coupled to the excited state, yielding two important benefits. First, despite the use of on-resonant light, spontaneous emission can be nearly completely avoided, and secondly, the atoms experience very low ac Stark shifts [31].

Adiabatic passage was first used in magnetic spin resonance [32, 33] before being carried over into the optical regime [34]. This process drove the transfer by chirping

the field frequency through resonance. This approach can also be applied for optical transitions by sweeping the two-photon difference frequency through resonance [35, 36]. Achieving low ac Stark shifts with adiabatic passage requires the laser frequencies to remain on resonance, which suggests another method of adiabatic passage that replaces the frequency chirp with a time offset between the two fields.

Adiabatic population transfer with time-delayed fields was first demonstrated in the optical regime by passing a molecular beam through two displaced Gaussian beams [37]. Driving the transition with counterpropagating beams changes the momentum states of atoms simultaneously with the internal states, thereby creating the momentum transfer needed for use in atom interferometry [30, 38]. Several groups have demonstrated adiabatic population transfer with time-delayed pulses [39, 40, 41]. In the earliest experiment, the internal states were changed with counterpropagating beams, so momentum transfer must have occurred, but it was not resolved in the detection [39]. Momentum transfer of $4\hbar k$ and $6\hbar k$ was first observed in helium with 95%/ $2\hbar k$ and 84%/ $2\hbar k$ transfer efficiency, respectively [40], and $8\hbar k$ transfer in cesium with an efficiency of 81%/ $2\hbar k$ [41]. In the latter experiment, the $8\hbar k$ momentum transfer was achieved in a single step by changing the internal atomic state from the $6S_{1/2}$, $F = 4$, $m_F = +4$ to the $F = 4$, $m_F = -4$ Zeeman sublevel using the cesium D_2 line. The authors of that work suggested that off-resonant excitation to other states in the excited-state hyperfine manifold limited the transfer efficiency.

In contrast to earlier work using optical adiabatic passage, we use a magnetic-field insensitive transition, which is essential for precision interferometry [22]. We transfer the atoms between the cesium $6S_{1/2}$ hyperfine ground states $F = 3$, $m_F = 0$ and $F = 4$, $m_F = 0$ via the excited state $6P_{1/2}$, $F' = 3$ or 4 , $m_F = 1$ by two counterpropagating laser beams in a $\sigma^+ - \sigma^+$ polarization configuration. The cesium D_1 line has the advantage of a 5.8 times larger excited state hyperfine splitting (1.17 GHz) [42] compared to the D_2 line, which significantly reduces off-resonant excitation [39]. Finally, by shaping the excitation pulses, we have been able to improve the transfer efficiency. In the course of our work on the photon recoil measurement, we have demonstrated coherent momentum transfer in cesium with efficiency as high as 93%/ $2\hbar k$. Additionally, we have created the first atom interferometer using adiabatic passage to split,

redirect, and recombine atomic wave packets [43].

Adiabatic passage by delayed laser pulses appears attractive since the atoms remain in a dark state and should not undergo any ac Stark shifts. However, transfer in a finite amount of time requires slight nonadiabaticity. Since the atoms undergo many Rabi cycles during the transfer, the nonadiabaticity might cause significant phase shifts from ac Stark shifts. Before deciding to use adiabatic passage in the second generation of the photon recoil measurement, we first studied the ac Stark shifts induced in the transfer process for a more realistic atomic system and the practical limits to transfer efficiency [31]. I will present a report of those results here. First, I will derive the general formulas describing adiabatic passage in a three-level atom. Then I will show analytically that in a pure three-level system, an atom does not experience any ac Stark shift when the lasers are tuned precisely on resonance with the intermediate state. Next I present numerical calculations of transfer efficiencies and ac Stark shifts for a realistic atomic system. In real atoms, the presence of additional excited states introduces ac Stark shifts and limits the maximum possible transfer efficiency, so I also show results including the ac Stark shift caused by the presence of a fourth level.

General results

Consider again the three-level atom of Fig. 2.4 interacting with counterpropagating laser beams of frequencies ω_1 and ω_2 . For adiabatic passage we set the single-photon detuning near zero, so the relaxation rate Γ of the intermediate state $|i\rangle$ can not be neglected. Its effect can be included by adding to the Hamiltonian of Eq. (2.2) a non-Hermitian term [27], giving

$$\hat{H} = \frac{\hat{\mathbf{p}}^2}{2m} + \hbar\omega_a|a\rangle\langle a| + \hbar(\omega_i - i\Gamma/2)|i\rangle\langle i| + \hbar\omega_b|b\rangle\langle b| - \mathbf{d} \cdot \mathbf{E}, \quad (2.11)$$

where the driving electric field is given by

$$\mathbf{E} = \mathbf{E}_1 \cos(\mathbf{k}_1 \cdot \mathbf{x} - \omega_1 t + \phi_1) + \mathbf{E}_2 \cos(\mathbf{k}_2 \cdot \mathbf{x} - \omega_2 t + \phi_2). \quad (2.12)$$

At present, we neglect the off-resonant couplings of $|b\rangle$ and $|i\rangle$ by ω_1 , and $|a\rangle$ and $|i\rangle$ by ω_2 , as shown by the dashed lines in Fig. 2.4. (These couplings are important,

however, as they can limit the transfer efficiency and cause ac Stark shifts. Our numerical simulations including these couplings [43].)

We assume that the laser detunings from the respective transition frequencies are small compared to the splittings between the states, i.e., $\omega_1 \approx \omega_a$ and $\omega_2 \approx \omega_b$, so that transitions are induced only in a closed family of momentum states. In contrast with stimulated Raman transitions, for adiabatic passage we cannot adiabatically eliminate the population of the excited state, so the interaction state vector has the form

$$|\psi\rangle = \begin{pmatrix} c_{a,p}(t) \\ c_{i,p+\hbar\mathbf{k}_1}(t) \\ c_{b,p+\hbar\mathbf{k}_{\text{eff}}}(t) \end{pmatrix}, \quad (2.13)$$

where \mathbf{k}_{eff} is the effective wave vector for the two-photon transition from Eq. (2.7).

The interaction Hamiltonian is

$$\hat{H}_{\text{int}} = \frac{\hbar}{2} \begin{pmatrix} 0 & \Omega_1^* e^{i(\Delta_1 t - \phi_1)} & 0 \\ \Omega_1 e^{-i(\Delta_1 t - \phi_1)} & -i\Gamma & \Omega_2 e^{-i(\Delta_2 t - \phi_2)} \\ 0 & \Omega_2^* e^{i(\Delta_2 t - \phi_2)} & 0 \end{pmatrix}, \quad (2.14)$$

where the single-photon detunings of ω_1 and ω_2 are

$$\begin{aligned} \Delta_1 &= \omega_1 - (\omega_i - \omega_a) + \frac{|\mathbf{p}|^2 - |\mathbf{p} + \hbar\mathbf{k}_1|^2}{2m\hbar} \\ \Delta_2 &= \omega_2 - (\omega_i - \omega_b) + \frac{|\mathbf{p} + \hbar\mathbf{k}_{\text{eff}}|^2 - |\mathbf{p} + \hbar\mathbf{k}_1|^2}{2m\hbar}, \end{aligned} \quad (2.15)$$

the single-photon Rabi frequencies are

$$\begin{aligned} \Omega_1 &\equiv -\langle i | \mathbf{d} \cdot \mathbf{E}_1 | a \rangle / \hbar \\ \Omega_2 &\equiv -\langle i | \mathbf{d} \cdot \mathbf{E}_2 | b \rangle / \hbar \end{aligned}, \quad (2.16)$$

and the two-photon detuning is

$$\delta = \Delta_1 - \Delta_2 = (\omega_1 - \omega_2) - \left(\omega_{ba} + \frac{\mathbf{p} \cdot \mathbf{k}_{\text{eff}}}{m} + \omega_{\text{rec}} \right). \quad (2.17)$$

For the present analysis, we restrict discussion to the zero-detuning case $\Delta_1 = \Delta_2 = \delta = 0$. The effect of small detunings from the one- and two-photon resonances are discussed in Ref. [28]. Generally speaking, the following formulas are still approximately valid as long as both detunings are small compared to Ω_{eff} . We also consider

the effects of nonzero detunings in our numerical simulations. For zero-detuning, the Hamiltonian of Eq. (2.14) simplifies to

$$\hat{H}_{\text{int}} = \frac{\hbar}{2} \begin{pmatrix} 0 & \Omega_1^* e^{-i\phi_1} & 0 \\ \Omega_1 e^{i\phi_1} & -i\Gamma & \Omega_2 e^{i\phi_2} \\ 0 & \Omega_2^* e^{-i\phi_2} & 0 \end{pmatrix}. \quad (2.18)$$

For any Ω_1 and Ω_2 , there exists an eigenvector of \hat{H}_{int} with eigenvalue zero, given by

$$|\Psi_D\rangle = \begin{pmatrix} \cos \theta \\ 0 \\ \sin \theta e^{-i\phi} \end{pmatrix}, \quad (2.19)$$

where the real angles θ and ϕ are defined by the relation

$$\tan \theta e^{-i\phi} = -\frac{\Omega_1}{\Omega_2} e^{i(\phi_1 - \phi_2)}. \quad (2.20)$$

This eigenvector is of particular interest because the amplitudes for excitation from the two lower levels to the excited state exactly cancel [44, 45, 46]. Consequently, despite the presence of on-resonance light, an atom in $|\Psi_D\rangle$ will not experience spontaneous emission. This state is consequently referred to as the noncoupled, or “dark” state. Since the single-photon detuning is zero, the ac Stark shift is much smaller than for stimulated Raman transitions. In fact, for a three-level system, the ac Stark shift is zero even if the transfer is not completely adiabatic [31]. The presence of additional energy levels causes the ac Stark shift to deviate from zero, but if the detuning of these states is sufficient, the ac Stark shift can still contribute much less than one cycle of phase shift to an interferometer during the time of the light pulse.

If $\Omega_1 = \Omega_1(t)$ and $\Omega_2 = \Omega_2(t)$, but the variation with time is sufficiently slow that the system can evolve adiabatically, then the steady-state solution of Eq. (2.19) still applies [29]. To characterize the requirements for adiabaticity, we define an effective Rabi frequency

$$\Omega_0 = \sqrt{\Omega_1^2 + \Omega_2^2}. \quad (2.21)$$

If an atom is initially in the dark state defined by the light fields, and then the dark-state parameters θ and ϕ vary gradually over a time $\tau \gg 1/\Omega_0$ for $\Omega_0 \gg \Gamma$, or

$\tau \gg \Gamma/\Omega_0^2$ for $\Omega_0 \ll \Gamma$, then the atom will follow the dark state defined by the light, without undergoing excitation into $|i\rangle$.

Since we use laser-cooled atoms, we can take a new approach to adiabatic passage. Instead of using spatially displaced beams to drive the transfer, we precisely overlap the two laser beams and then vary the beam intensities. In that manner, we can create multiple pulses with a single pair of beams during the nearly 1 s period that the atoms stay within the beams. For example, Fig. 2.6(b) shows how we completely transfer atoms from one state to the other. Note that the adiabaticity criterion does not preclude turning on a single beam instantaneously, nor suddenly turning both beams on or off together, since none of these operations forces a rapid change of θ or ϕ . Consequently, these pulse shapes allow faster transfer with the same efficiency as for the two displaced Gaussian pulses of Ref. [29]. Other pulse sequences used for creating beam splitters for atom optics will be described in Sec. 2.2.2, but first we consider in greater detail the transfer efficiency and ac Stark shifts for complete transfer processes.

The population transfer achieved with adiabatic passage is qualitatively very different from the transfer achieved with stimulated Raman transitions. For stimulated Raman transitions, the atomic state vector evolves coherently regardless of the initial state of the system when the light pulse is applied. Consequently, light pulses that take an atom from $|a\rangle$ to $|b\rangle$ will also take an atom from $|b\rangle$ to $|a\rangle$. The effects of adiabatic transfer pulses, however, depend strongly on the initial state of the system. For example, if an atom starts out in $|a\rangle$, then Ω_2 must be turned on alone at the beginning of the adiabatic pulse sequence in order to avoid spontaneous emission. If Ω_2 alone were applied to an atom initially in $|b\rangle$, however, then the atom would scatter photons, eventually resulting in an incoherent transfer into $|a\rangle$ via optical pumping. More generally, suppose the state of the atom at time $t = 0^-$ is $|\psi(0^-)\rangle$, and that the laser beams are turned on at time $t = 0$ with phases and intensities defining a dark state $|\Psi_D(0^+)\rangle$. The projection $|\Psi_D(0^+)\rangle\langle\Psi_D(0^+)|\psi(0^-)\rangle$ of the initial atomic state onto the dark state gives the fraction of the initial state that will not scatter photons, but will adiabatically follow the dark state as it slowly changes to $|\Psi_D(t)\rangle$. Assuming that the beam intensities are varied sufficiently slowly that the transfer is completely

adiabatic, the coherently transferred part of the wave function immediately after the end of an adiabatic passage pulse of duration τ is

$$|\psi(\tau^+)\rangle = |\Psi_D(\tau^-)\rangle \langle \Psi_D(0^+)|\psi(0^-)\rangle. \quad (2.22)$$

In Fig. 2.6(b), the initial and final dark states are $|\Psi_D(0^+)\rangle = |a\rangle$ and $|\Psi_D(\tau^-)\rangle = |b\rangle$, so Eq. (2.22) correctly describes the operation of a complete transfer pulse. Reversing the roles of Ω_1 and Ω_2 provides for the opposite transfer. Later, Eq. (2.22) will be applied for analyzing atom interferometers using adiabatic passage.

ac Stark shifts for a 3-level system

During the population transfer, the atomic states undergo many Rabi oscillations, so nonadiabaticity may *a priori* allow a light-induced phase shift to accumulate. We now show analytically that for zero-detuning, $\Delta_1 = \Delta_2 = \delta = 0$, there is no accumulated phase shift for arbitrary pulse shapes, even if the transfer is not completely adiabatic.

Suppose that initially at time $t = 0$ the coupling fields are turned off and the wave function is

$$|\Psi(0)\rangle = \begin{bmatrix} c_a(0)e^{-i\phi_1} \\ ic_i(0) \\ c_b(0)e^{-i\phi_2} \end{bmatrix}, \quad (2.23)$$

where we are free to choose all of the coefficients $c_j(0)$ real. The phases ϕ_1 and ϕ_2 contain information regarding the phase relation of the wave function components relative to the light fields as the fields turn on. We will show that the wavefunction at any later time t can be written as

$$|\Psi(t)\rangle = \begin{bmatrix} c_a(t)e^{-i\phi_1} \\ ic_i(t) \\ c_b(t)e^{-i\phi_2} \end{bmatrix}, \quad (2.24)$$

with all $c_j(t)$ real. Since there is then no change in the relative phases of the various components of the wave function, this will prove that no light-induced phase shift accrues.

We can prove Eq. (2.24) by direct substitution into the time-dependent Schrödinger equation, which gives

$$\dot{\mathbf{c}}(t) = \mathbf{A}(t)\mathbf{c}(t), \quad (2.25)$$

where

$$\mathbf{A}(t) = \frac{1}{2} \begin{bmatrix} 0 & -\Omega_1(t) & 0 \\ \Omega_1(t) & -\Gamma & \Omega_2(t) \\ 0 & -\Omega_2(t) & 0 \end{bmatrix} \quad (2.26)$$

is a real matrix. (We can take Ω_1 and Ω_2 to be real by including any phase in ϕ_1 and ϕ_2 .) If we assume reasonable restrictions on the smoothness of $\mathbf{A}(t)$, then a unique solution of Eq. (2.25) exists for $t > 0$. Furthermore, since both $\mathbf{c}(0)$ and $\mathbf{A}(t)$ are real, the solution $\mathbf{c}(t)$ must also be real [47], which proves Eq. (2.24). We have verified this result using the Bloch equations for the three-level density matrix.

The dressed-state picture also provides an explanation for this result. Since the dressed state eigenenergies $\lambda_{\pm} = \pm\sqrt{(\Omega_{\text{eff}}/2)^2 - (\Gamma/4)^2}$ are symmetrically shifted about zero and the nonadiabatic populations of the two coupled states during the laser pulses are equal, the average shift is zero.

Numerical calculations

We have performed numerical simulations for the adiabatic passage complete transfer pulses of Fig. 2.6(b) with $\Omega_{1,\text{max}} = \Omega_{2,\text{max}}$ [31]. The atomic system used for the calculation is the magnetic-field insensitive transition between the cesium hyperfine ground states $6S_{1/2}$, $F = 3$, $m_F = 0 \leftrightarrow 6S_{1/2}$, $F = 4$, $m_F = 0$ using $6P_{1/2}$, $F' = 4$, $m_F = +1$ as an intermediate state. Counterpropagating lasers with a $\sigma^+ - \sigma^+$ polarization configuration drive the atom. We assumed that the two-photon detuning $\delta = 0$, so that the one-photon detunings are equal, $\Delta_1 = \Delta_2 \equiv \Delta$. The goal of the calculations was to determine the theoretical and practical limits to the transfer efficiency, as well as the expected size of ac Stark shifts contributed by the presence of additional atomic levels and nonzero detunings.

We obtained numerical results using two techniques. First, we directly integrated the interaction Schrödinger equation. I present the results of those calculations below. With this technique, imperfect coherent transfer appears directly as a reduction

in the wave function modulus. To check these results, we also integrated the Bloch equations. This approach requires more care for determining coherent transfer efficiency and absolute phase shifts. We added a fourth level not coupled to the first three levels corresponding to atoms in a separate arm of an atom interferometer. A coherence was introduced between the initial state and the fourth state before the transfer pulse. Then by determining the amount of coherence that could be transferred to the final state and the fourth state, we could calculate the coherent transfer efficiency.

We first calculated the transfer efficiency and ac Stark shift phase for zero detuning $\Delta = \delta = 0$, as shown in Fig. 2.7. These results include the effects of off-resonant excitation to the neighboring $6P_{1/2}$, $F' = 3$ level and also the effect of the small 9.2 GHz off-resonant couplings of ω_1 with the transition $|b\rangle \leftrightarrow |i\rangle$ and ω_2 with $|a\rangle \leftrightarrow |i\rangle$. The calculations cover a range of pulse lengths τ for three different intensity levels. To clarify the influence of the additional system complexities, the dotted lines of Fig. 2.7 show the transfer efficiency for a simple three-level system. (In this case the ac Stark shift is identically zero.) As expected, in this ideal three-level system, the transfer efficiency increases monotonically with τ as the adiabaticity of the transition improves. With the existence of additional levels, however, the transfer efficiency initially increases with improving adiabaticity, but eventually decreases because of spontaneous emission losses. Meanwhile, the ac Stark shift increases monotonically with τ . The maximum transfer efficiency is about 98.7% (independent of the laser power for $I_{j,\max} \gg I_{\text{sat}}$) for an optimum pulse length of $\tau \approx (500 \mu\text{s}) \times I_{\text{sat}}/I_{j,\max}$, where I_{sat} is the saturation intensity. Since the accumulated phase shift for a reasonably adiabatic process is roughly proportional to the pulse length at a given laser intensity, shortening the pulse length below that required for peak transfer efficiency may yield lower ac Stark shifts. This issue will be discussed further in Sec. 4.2.3.

For comparison with the original technique for adiabatic transfer using displaced Gaussian beams, we replaced the pulse shapes shown in Fig. 2.6(b) with

$$\begin{aligned}\Omega_1(t) &= \Omega_{1,\max} e^{-(t/\tau-u)^2} \\ \Omega_2(t) &= \Omega_{2,\max} e^{-(t/\tau+u)^2}.\end{aligned}\quad (2.27)$$

In this case, we obtained a maximum transfer efficiency of 98.7% for $u \approx 0.5$ and

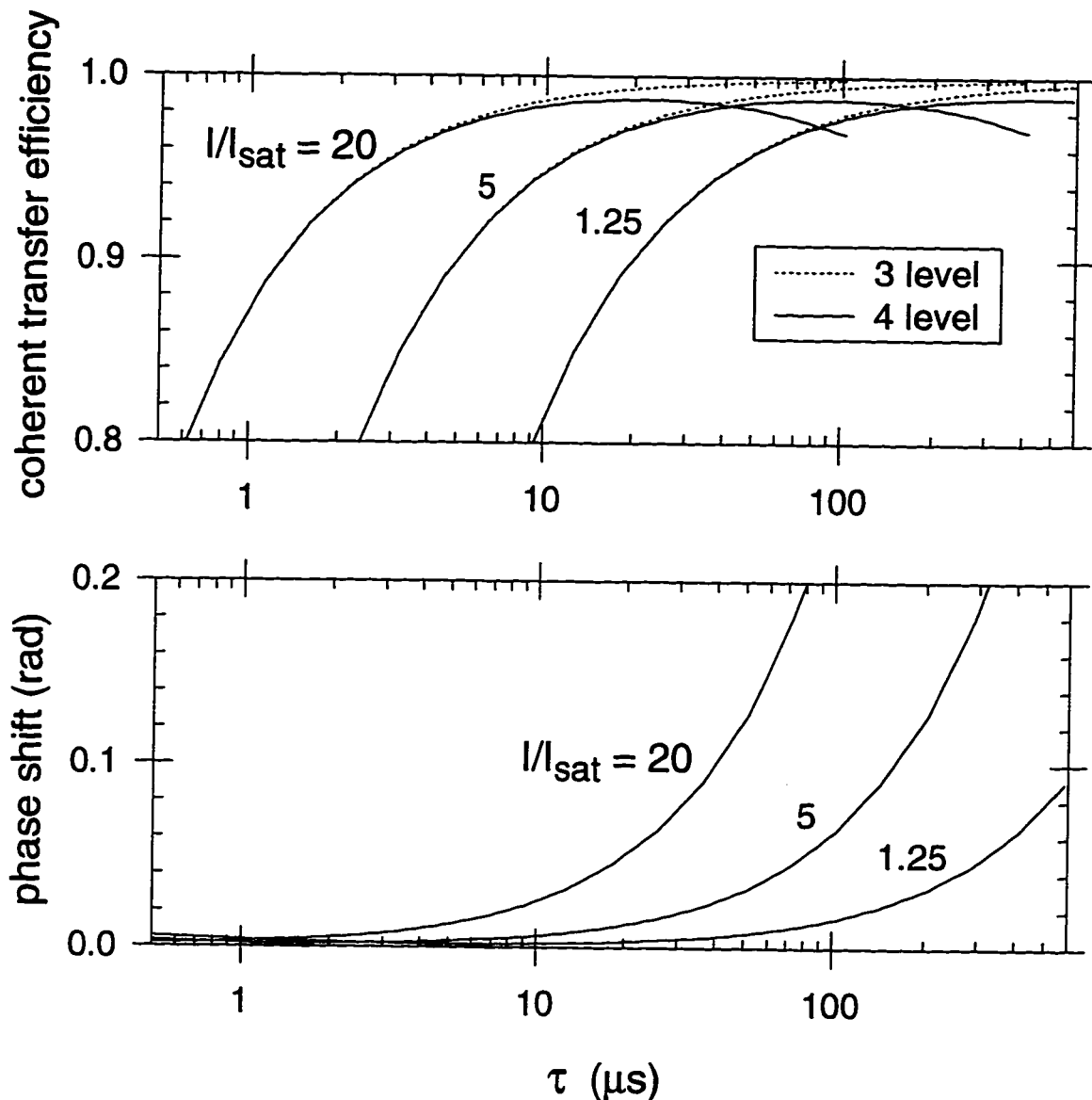


Figure 2.7: Numerical simulations of adiabatic passage for zero detuning. We calculated coherent transfer efficiencies and accumulated phase from ac Stark shifts as a function of pulse length τ for adiabatic population transfer using the cesium $6S_{1/2}$, $F = 3$, $m_F = 0 \leftrightarrow F = 4$, $m_F = 0$ transition with $6P_{1/2}$, $F = 4$, $m_F = +1$ as an intermediate state. Results are shown for three laser intensities ($I_{\text{sat}} \approx 2.2 \text{ mW/cm}^2$ for the cesium D_1 line). The dotted lines show the computed coherent transfer efficiencies for a three-level system, neglecting off-resonant absorption. The ac Stark shift phase contribution is zero for this case.

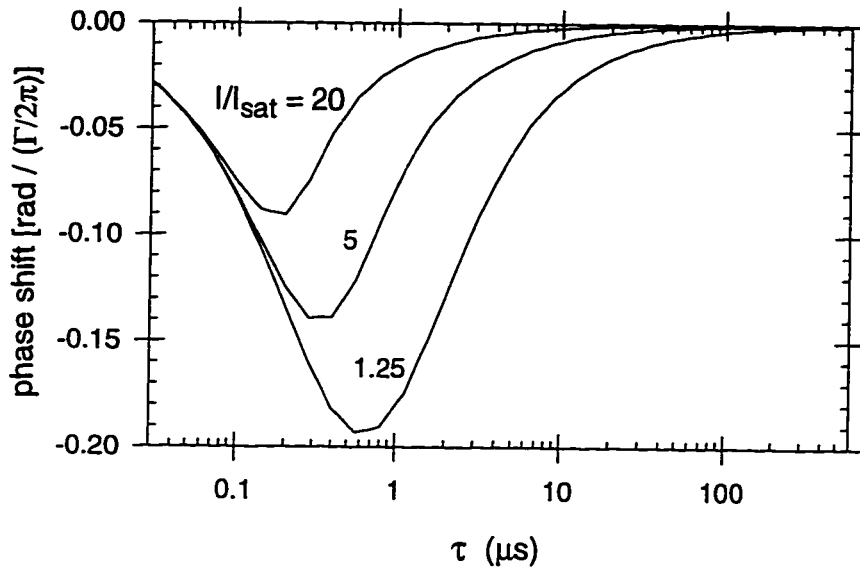


Figure 2.8: Numerical simulations of adiabatic passage for nonzero detunings. We calculate the accumulated phase from ac Stark shifts during adiabatic population transfer in a three-level system for a detuning $\Delta = \Gamma/2\pi$ as a function of pulse length T for three different laser intensities. For small detunings, the accumulated phase shift is proportional to Δ .

$\tau \approx (350 \mu\text{s}) \times I_{\text{sat}}/I_{j,\text{max}}$. The tails of these Gaussian pulses must of course be truncated in a real experiment. With a cutoff at the beam waist, this approach requires 70% longer pulses for the same transfer efficiency as the pulse shapes in Fig. 2.6(b).

We then introduced a small detuning Δ from the one-photon resonance. Since the dark state is still a precise eigenstate of the system with eigenvalue zero for a perfectly adiabatic process [29], no phase shift occurs. A partially nonadiabatic transfer, however, introduces a phase shift since a detuning Δ implies that the eigenvalues of the two coupled states are no longer equally shifted from the dark state energy. The light-induced phase shift is proportional to Δ for $\Delta \ll \Omega_{j,\text{max}}$. Consequently, in Fig. 2.8 we plot the phase shift-to-detuning ratio. Again we performed the calculations for a range of pulse durations for three different laser intensities. We do not anticipate problems from detunings δ from the two-photon resonance since we set this difference frequency very precisely.

Section 2.2.1 described how ac Stark shifts occurring for stimulated Raman transitions can be at least partially canceled. Similar cancellation of the residual ac Stark shifts is also possible for adiabatic population transfer in a four-level system if the lasers are detuned slightly from the one-photon resonance [31]. The necessary detuning, which may be a few linewidths of the excited state, can be approximately determined from the phase shift curves in Figs. 2.7 and 2.8. This optimum detuning is a function of both laser pulse length and intensity. Thus, compensation of the residual ac Stark shift here is more problematic and thus probably less effective than for the case of Raman π and $\pi/2$ pulses, which depends only on the ratio of the intensity of the two Raman lasers and the one-photon detuning [15]. On the other hand, the phase shift accumulated during an adiabatic passage transfer is only about 0.02 rad for 98% transfer efficiency, two orders of magnitude below the raw phase shift from each ground state level during a Raman pulse. Consequently, adiabatic passage appears to be an attractive method to realize high efficiency optical elements for atom optics with small accumulated phase shifts from the ac Stark effect.

Our numerical simulations confirmed that the cesium D_1 line gives higher peak transfer efficiency and lower ac Stark shifts than for the D_2 line. The results also suggested the potential for higher transfer efficiency and lower ac Stark shifts than we obtained with stimulated Raman transitions in the first version of the recoil measurement.

Atom interferometry using adiabatic passage

So far, I have restricted the discussion of adiabatic passage to the complete population transfer created by pulses such as in Fig. 2.9(a). Because of the differences between adiabatic passage and stimulated Raman transitions cited in Sec. 2.2.2, adiabatic passage can not provide perfect replacements for the π and $\pi/2$ pulses of stimulated Raman transitions. Consequently, the recoil diagrams described thus far using π and $\pi/2$ pulses cannot all be directly implemented using adiabatic passage. The purpose of this section is to describe the capabilities and limitations of adiabatic passage for atom interferometry.

Figure 2.9 shows pulse sequences that, along with their complements formed by

interchanging the roles of Ω_1 and Ω_2 , form the basis for constructing atom interferometers using adiabatic passage. The dark state at any time during a pulse is determined by substituting the laser phases and Rabi frequencies into Eqs. (2.19) and (2.20). The net effect of each of these sequences can be determined from Eq. (2.22), using the dark states $|\Psi_D(0^+)\rangle$ and $|\Psi_D(\tau^-)\rangle$ corresponding to the beam phases and intensities at the beginning and end of the pulse sequence, respectively. The beam-splitter pulse in Fig. 2.9(b) is essentially half of a complete transfer pulse. Turning both beams off when the intensities are equal leaves an atom in an equal coherent superposition of $|a\rangle$ and $|b\rangle$ [30]. A pulse of this type splits a single path into two paths for an atom interferometer. Figure 2.9(c) is the time reversal of Fig. 2.9(b), so it projects the initial state of the atom onto the equal coherent superposition with phase defined by $|\Psi_D(0^+)\rangle$, and then transfers that fraction of the wave function into $|a\rangle$. This sequence combines or redirects paths in an atom interferometer. Similarly, Fig. 2.9(d) projects the initial state onto the superposition state defined by $|\Psi_D(0^+)\rangle$, but then leaves the atom still in that superposition state. This pulse sequence is used to split interferometer paths when the atom must start and remain in a superposition state. For an atom initially in either one of the ground states, this element generates a coherent superposition of the two ground states. Half of the population, however, is lost to spontaneous emission. We have demonstrated that pulses like these can be combined to create adiabatic passage atom interferometers [31] with identical geometries to those in Fig. 2.1(b). More recently, we have created modified Ramsey-Bordé interferometers as in Fig. 2.3(b), as will be described later.

The pulse sequences of Fig. 2.9(b)–(d) require sudden simultaneous transitions of both beam intensities. The first demonstrations of adiabatic population transfer used displaced Gaussian beams. Unfortunately, it is not easy with spatially displaced beams to create sudden uniform intensity transitions for two fields. Our experiments with adiabatic passage use laser-cooled atoms launched in a vertical trajectory, centered in a pair of vertical laser beams. By independently controlling beam intensities using acousto-optic modulators, we can directly replicate all of the pulse sequences of Fig. 2.9. In fact, the atoms remain within the $\approx 2\text{-cm}$ diameter beams for up to about 1 s, so that this single pair of beams can apply many pulses. Hence, we can

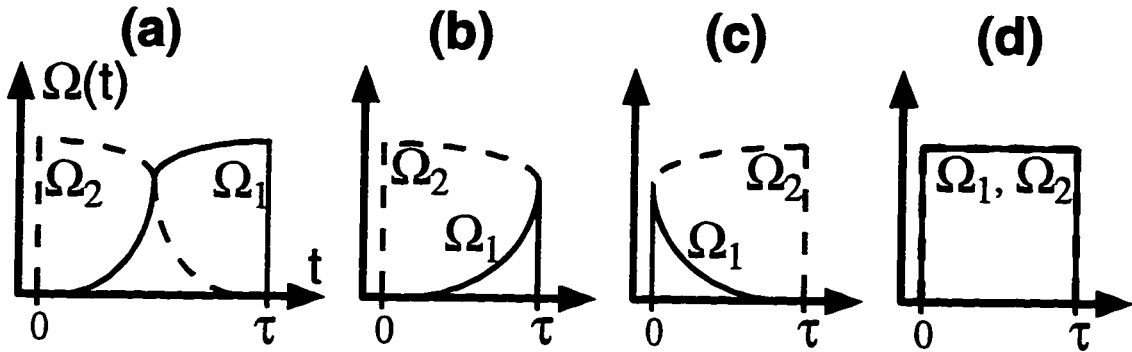


Figure 2.9: Atom optics using adiabatic passage. Changing the field amplitudes Ω_1 and Ω_2 with time (a) transfers an atom from $|a\rangle$ to $|b\rangle$, (b) transfers an atom from $|a\rangle$ to $(|a\rangle + |b\rangle)/\sqrt{2}$, (c) transfers an atom from $(|a\rangle + |b\rangle)/\sqrt{2}$ to $|a\rangle$, and (d) leaves an atom in $(|a\rangle + |b\rangle)/\sqrt{2}$, but sets the phase of the atomic coherence to the phase of the dark state.

create interferometers with practically arbitrary complexity.

As an initial illustration of atom interferometry using adiabatic passage, consider the Ramsey separated oscillatory field method, which requires only two interactions since the atomic wave packet does not separate. Here, instead of microwave transitions, however, we use Doppler-free Raman transitions with two copropagating beams ($\mathbf{k}_2 \approx \mathbf{k}_1$). The two field interactions consist of the pulses in Fig. 2.9(b) and (c) separated by a time T . When the two-photon difference frequency $\delta \equiv \omega_1 - \omega_2$ of the laser beams is detuned from the ground state hyperfine splitting (assume $\delta \ll \Delta\omega_D$, where $\Delta\omega_D$ is the frequency width of a single pulse), the dark state after a time T differs from the original one by an accumulated phase $\Delta\phi = \delta T$. The second pulse projects the atomic wave function onto the dark state defined by the light. This projection has amplitude

$$\begin{aligned} \langle \Psi_D | \psi(T + \tau) \rangle &= \frac{1}{2} [\langle a, p | -e^{i\delta T} \langle b, p + \hbar k_{\text{eff}} |] \cdot [|a, p\rangle - |b, p + \hbar k_{\text{eff}}\rangle] \\ &= \frac{1}{2} (1 + e^{i\delta T}), \end{aligned} \quad (2.28)$$

where $\mathbf{k}_{\text{eff}} \equiv \mathbf{k}_1 - \mathbf{k}_2$ corresponds to the recoil of a microwave photon. The remainder of the second pulse transfers the atom from the superposition state back into state $|a\rangle$. Scanning δ then causes an oscillation in the number of atoms exiting the pulse

sequence in state $|a\rangle$, which is the standard atomic clock signal. In the early stages of testing adiabatic transfer, we demonstrated this interferometer. We observed fringes both by counting the number of atoms surviving in one of the cesium ground state sublevels, and also by detecting the fluorescence from the atoms that scattered photons during the second interaction because they were in the coupled state.

Returning to counterpropagating beams $\mathbf{k}_2 \approx -\mathbf{k}_1$, Fig. 2.10 shows a straightforward implementation of the Ramsey-Bordé interferometer geometry [17, 48] using the adiabatic passage pulses from Fig. 2.9. Since the photon recoil measurement uses this type of interferometer, I will develop the expressions for the interferometer signal including an initial spread $f(\mathbf{p})$ of atomic momentum. The first pulse splits the initial state into a coherent superposition of $|a\rangle$ and $|b\rangle$. After the atom freely evolves for a time T , a second pulse projects the atomic wave function onto the dark superposition state $|\Psi_D(t_2^+)\rangle$, where t_2 is the start time of the second pulse, as shown in Fig. 2.10(b). When Ω_1 turns off, the atom is left in $|a\rangle$. (Turning off Ω_2 instead also leads to a valid interferometer, which is the upper interferometer of Fig. 2.1(b) for the photon recoil measurement.) The fraction of the wave packet that is out of phase with $|\Psi_D\rangle$ will undergo spontaneous emission, and thus lose coherence. It may contribute to the background signal of the interferometer, but will not cause a systematic shift of the fringes. Equation (2.28) still correctly gives the amplitude of the atomic wave function after this projection, except that now δ includes Doppler shifts from the atomic momentum, as in Eq. (2.17), and \mathbf{k}_{eff} now corresponds to the recoil of two optical photons. This result is the familiar velocity grating. The third pulse splits each of the two paths in state $|a\rangle$ into superposition states. After waiting again for a time T , two of the paths overlap spatially. A final pulse applied at this time projects the wave function onto the superposition state $|\Psi_D(t_4^+)\rangle$, again evaluated at the start of the pulse. This second projection operation decreases the wave function amplitude by another factor of the form of Eq. (2.28), except that δ changes to account for the reversed beam directions and the recoil from the first pair of pulses. Integrating this amplitude over the initial distribution of atomic momentum gives the wave function

at the end of the interferometer:

$$|\Psi(t)\rangle = \frac{1}{4} \int d^3 p f(p) |a, p\rangle [1 + e^{i2(\Delta\omega - \omega_{\text{rec}})T} + 2e^{i(\Delta\omega - \omega_{\text{rec}})T} \cos(\mathbf{k}_{\text{eff}} \cdot \mathbf{v})], \quad (2.29)$$

where ω_{rec} is the recoil shift, and δ is assumed to be adjusted to compensate for the gravitational shift so that the detuning $\Delta\omega$ in the atom's reference frame is equal for all pulses. The second term in the brackets gives the fringes, while the last term averages to zero after integration over a broad velocity distribution.

In this interferometer, the two distinct atomic states between which the atomic population oscillates are the dark state and a coupled state that spontaneously decays. This final pulse is tailored to force the atoms to exit in whichever state is preferable for detection, in this case $|a\rangle$. If the phase of the atomic coherence at the overlap point matches the phase of the dark state, then the atom signal will be at a maximum. Scanning δ for the last two pulses changes the relative phase of the atomic coherence and the field, allowing observation of fringes in the atom populations. We have demonstrated atom interferometers with this configuration using adiabatic passage [43].

Creating an analog of the three-pulse $\pi/2 - \pi - \pi/2$ interferometer of Fig. 2.1(a) using adiabatic passage presents special difficulty due to the lack of a substitute for the π pulse. The center pulse in the interferometer is required to redirect both paths, while leaving the atoms in a coherent superposition of $|a\rangle$ and $|b\rangle$. The only adiabatic passage pulse sequence which accomplishes this is Fig. 2.9(d). The phase of the coherence at the time of the π pulse depends on the motional Doppler shift $\mathbf{k}_{\text{eff}} \cdot \mathbf{v}$. For a collection of atoms with a velocity spread Δv such that $(k_{\text{eff}} \Delta v)T \gg 2\pi$, where T is the time between pulses, the phase of the coherence varies greatly over the collection of atoms. Consequently, the phase of the dark state can not be set to simultaneously deflect the paths of all of the atoms. Half of the initial atoms are lost to spontaneous emission in the projection operation. For a three-pulse interferometer implemented using stimulated Raman transitions, a π pulse can completely redirect either state, so a corresponding loss does not occur.

Similar problems limit the use of adiabatic passage for creating large-area interferometers such as that in Fig. 2.3(a). It is feasible with stimulated Raman transitions

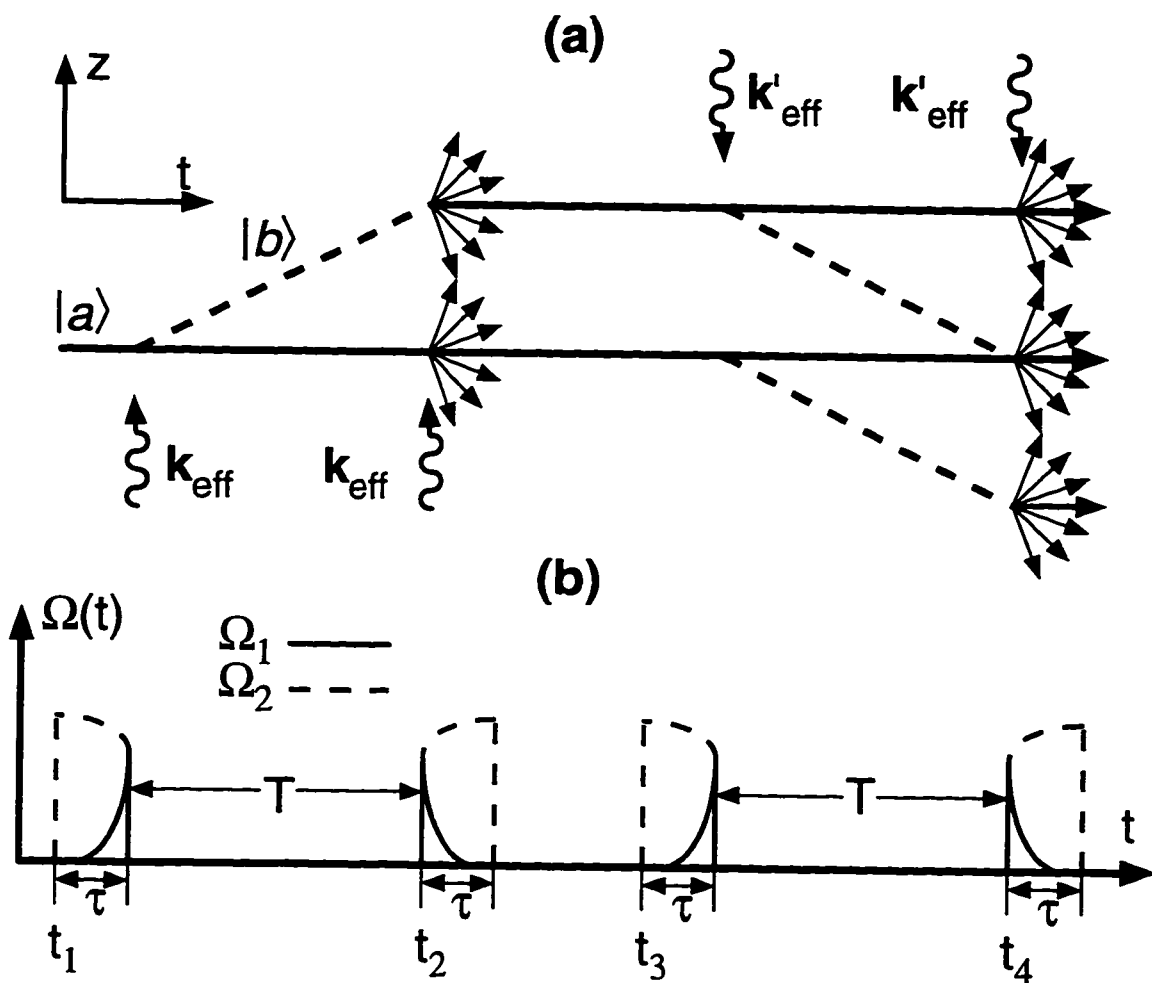


Figure 2.10: Ramsey-Bordé interferometer implemented by adiabatic passage. (a) Recoil diagram. At the second and fourth interactions, the multiple arrows indicate atoms that spontaneously emit because they are in the coupled state, so that their resulting momenta vary. For a three-level system, all of these atoms are optically pumped into $|a\rangle$, so they contribute to the background signal of the interferometer. Neglecting ac Stark shifts, the interferometer phase shift depends only on T , not on τ . (b) This adiabatic passage pulse sequence creates the interferometer in (a).

to separately address the two branches by choosing $\Omega_{\text{eff}} \ll \omega_{\text{rec}}$. The other path will experience an ac Stark shift, but will not scatter photons. With adiabatic passage, however, typical motion-induced detunings of an atom, $\delta \ll \Gamma$, so an atom will scatter photons if it is detuned beyond the dark-state width $\Delta\omega_D$. For an atom to maintain its coherence, it must always remain in a dark state. In an effective two-level system, as considered thus far, this requires that the total momentum transferred in the interferometer does not detune the atom from the dark state. Even then, we must replace each intermediate π pulse with a pulse as in Fig. 2.9(d), which causes a 50% signal loss per pulse. Alternatively, to achieve large momentum transfer with adiabatic passage for this type of interferometer, a third metastable state could be added for preserving one of the branches of the interferometer from scattering photons while the other path is deflected.

The atom interferometer geometry in Fig. 2.3(b), on the other hand, is easily implemented using adiabatic passage since for either the upper or lower interferometer, the atoms are in the same internal state for every π pulse. Since the initial internal state is always known, these π pulses can be replaced by pulses as in Fig. 2.9(a) and its complement. This is the approach presently used for the photon recoil measurement, which provides a factor of $N + 1$ enhancement of the sensitivity.

Another possible route for achieving large-area interferometers using adiabatic passage is to apply a single adiabatic passage pulse that involves the interchange of multiple photons, e.g., using $\sigma^+ - \sigma^-$ polarized beams to transfer an atom between the $m_F = -F$ and $m_F = +F$ ground state sublevels of an atom [41, 49]. For a valid dark state, the frequency width of the dark state must be larger than the total recoil splitting between the two states, which can require considerable laser power for typical beam diameters. Also, these approaches generally involve the use of magnetic-field sensitive transitions. For most precision measurement experiments, magnetic-field nonhomogeneities can not be controlled to the level that such transitions are practical.

A final consideration regarding the use of adiabatic passage for atom interferometry is the level of background atoms that appears in the interferometer signal. In the case of a three-level atom, it would be difficult to distinguish the atoms transferred

by adiabatic passage from those transferred by optical pumping. On average, the momentum transfer would be smaller for optical pumping, but this would be hard to distinguish without subrecoil cooling of the atoms. Incorporating an adiabatic transfer pulse into an atom interferometer would reveal a loss of fringe contrast corresponding to the fraction of optically pumped atoms. In more complex systems, careful selection of beam polarizations allow optical pumping predominantly into states other than the states used for the adiabatic passage. This allows the coherently and incoherently transferred atoms to be distinguished in the detection stage, so that the optical pumping does not cause a severe degradation of fringe contrast [43]. For the cesium D_1 line, the theoretical maximum 33% fringe contrast using the $F' = 3$ excited state is considerably better than the 23% maximum contrast for $F' = 4$ because of smaller matrix elements for falling back into the dark state after spontaneous emission. This is the reason that we switched to the $F' = 3$ excited state in the actual experiment, even though all of our numerical simulations used the $F' = 4$ level.

In contrast, with stimulated Raman transitions, atoms left behind in the wrong atomic state after each π did not affect the fringe contrast since they could be distinguished and removed from the interferometer before the final beam splitter [15]. This clearing process did require an intense on-resonance beam interacting with the atoms within the interferometer, however, which opens the door for ac Stark shifts. In practice the fringe contrast was about the same for interferometers with adiabatic passage and stimulated Raman transitions.

2.3 Recoil measurement using atom interferometry

The previous section described the adiabatic passage implementation of the modified Ramsey-Bordé interferometer used for the photon recoil measurement. Figure 2.1(b) shows the pair of atom interferometers needed for the differential measurement. Notice the similarity of this geometry with the measurement described in Fig. 1.2(c). Essentially, the change from that simple experiment is to replace both branches of the

original measurement with an independent atom interferometer, and then to enhance the momentum transfer in each interferometer as shown in Fig. 2.3(b). The purpose of this section is to discuss the optimization of sensitivity of this atom interferometry measurement, and to generalize the equations developed in Sec. 1.2 for two-photon transitions in modified Ramsey-Bordé interferometers.

Experimentally, switching between measurements for the two interferometers of Fig. 2.1(b) requires shifting the two-photon detuning δ for the third and fourth pulses, and changing the adiabatic passage pulse shapes to leave the atoms off in the opposite ground state after the second pulse. One resonance occurs for each interferometer, as demonstrated experimentally in Fig. 2.11. The two resonances, which are separated by Δf_{rec} , have interference fringes with periodicity $1/T$, where T is the time between beam-splitter pulses. Adapting the original expression for Δf_{rec} from Eq. (1.2) for two-photon transitions gives

$$\Delta f_{\text{rec}} = \frac{2h\nu_{\text{eff}}^2}{m_{\text{Cs}}c^2}, \quad (2.30)$$

where

$$\nu_{\text{eff}} \equiv \frac{c|\mathbf{k}_{\text{eff}}|}{2\pi} = \nu_1 + \nu_2 \quad (2.31)$$

is the frequency of a single photon that would provide the same momentum recoil as \mathbf{k}_{eff} . (The last relation assumes that \mathbf{k}_1 and \mathbf{k}_2 perfectly counterpropagate.)

To realize high experimental sensitivity, we want to simultaneously maximize T and Δf_{rec} . The key starting point for achieving large T is to use a fountain of laser-cooled atoms. An obvious way to increase Δf_{rec} is to use a lower-mass atom, such as hydrogen, helium, or lithium. The disadvantage of that solution is that it is harder to cool lighter atoms to as low of velocities as cesium, so the gain in Δf_{rec} comes at the expense of T . The alternative approach that we have taken is to leave the size of Δf_{rec} alone, but to measure a larger number of recoils by adding mirror pulses between the two beam-splitter pairs as shown in Fig. 2.3(b). Adding N transfer pulses causes the frequency separation of the two interferometers to increase to

$$\Delta f_{\text{rec}}^N \equiv (N+1)\Delta f_{\text{rec}}, \quad (2.32)$$

while leaving the fringe spacing unchanged.

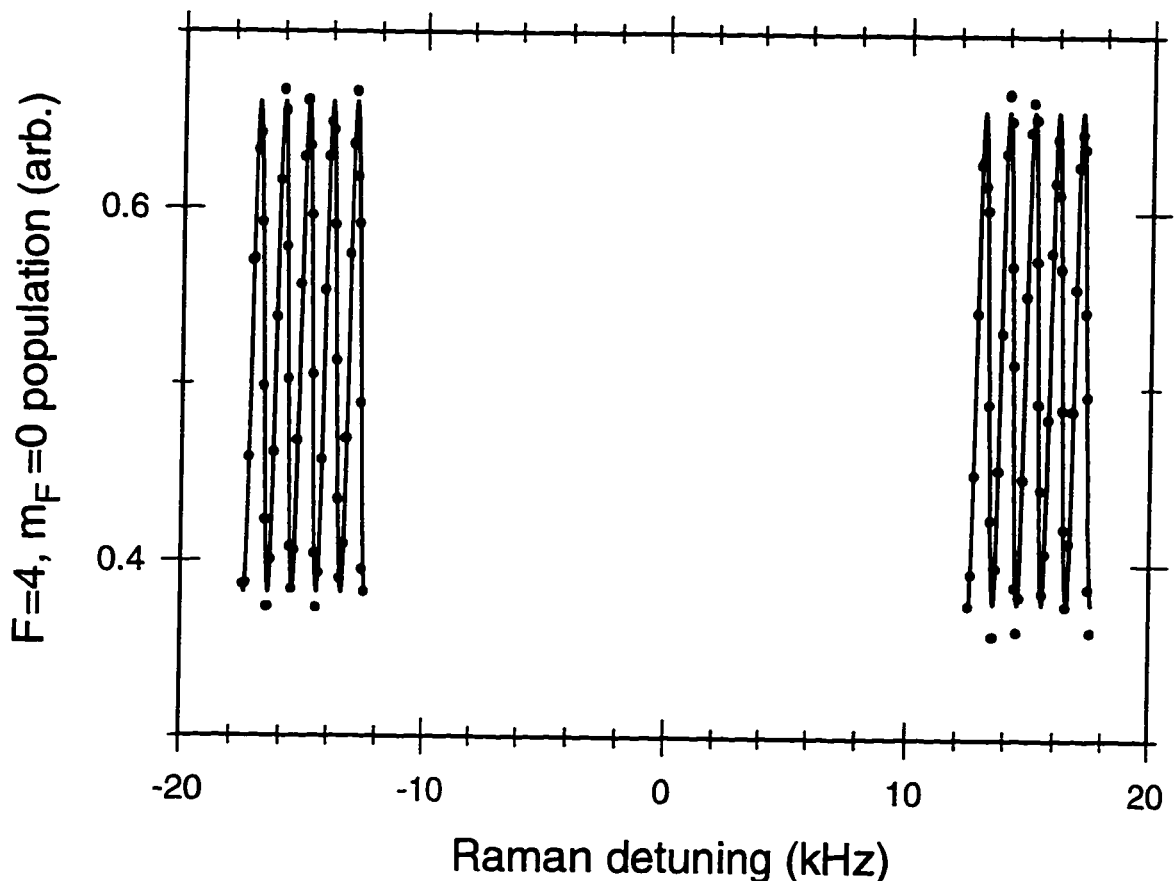


Figure 2.11: Two interferometer resonances used in the recoil measurement. Each point is the measurement from a single launch, interferometer, and detection cycle. The frequency difference between the centers of the two resonances is $\Delta f_{\text{rec}} \approx 30$ kHz and the interferometer fringe spacing is $1/T = 1$ kHz. For the resonances to be visually resolvable on a single plot, we drastically reduce the normal sensitivity of the interferometer by using parameters of $T = 1$ ms and $N = 0$. This 90 s set of data measures Δf_{rec} to about 150 ppm. Peak precision occurs for experimental parameters of $T \approx 120$ ms and $N \approx 30$, which yield a factor of ~ 1000 increase in the measurement resolution.

The remainder of the results from Sec. 1.2 relating to the recoil measurement can be generalized for a measurement using two-photon transitions in a modified Ramsey-Bordé interferometer with N transfer pulses. For future reference, those results become:

$$\frac{h}{m_{\text{Cs}}} = \frac{c^2 \Delta f_{\text{rec}}}{2\nu_{\text{eff}}^2} \quad (2.33)$$

$$\alpha^2 = cR_\infty \left(\frac{m_p}{m_e}\right) \left(\frac{m_{\text{Cs}}}{m_p}\right) \frac{\Delta f_{\text{rec}}}{\nu_{\text{eff}}^2}. \quad (2.34)$$

Note that the enhancement factor N does not appear in either of these equations because it is immediately removed in calculating Δf_{rec} from Δf_{rec}^N via Eq. (2.32).

Chapter 3

Experiment

In this chapter, I will first give a summary of the major features of the experiment. Then I will describe in greater detail the various parts of the apparatus, especially those that have been added or significantly modified in this version of the recoil measurement. I will also describe measurements we made to characterize the individual performance of the experimental equipment. Chapter 4 will cover more comprehensive tests of the entire experiment based on the consistency of the final photon recoil result.

3.1 Summary of the experiment

Figure 3.1 shows the positions and orientations of the various beams that interact with the atoms during the course of the experiment. To achieve a long interferometer interaction time with the atoms, we start with a cold atom source. A cesium atomic beam, slowed by a chirped laser beam [50], loads a magneto-optic trap (MOT) [51]. A Ti:Sapphire laser operating at the cesium D_2 line provides the slowing and trapping light. After a MOT loading time of about 200 ms, the trapping magnetic field shuts off. Next acousto-optic modulators (AOM's) shift the frequencies of the trapping beams to create a molasses in a frame traveling upward at 2.72 m/s [52]. This launches the atoms along a vertical trajectory that will peak at about 37.7 cm above the trap, which is near the top of the solenoid in Fig. 3.1. Before the atoms leave the

trap beams, the beam intensities decrease to further cool the atoms to about $4 \mu\text{K}$ using polarization-gradient cooling. A mechanical shutter then simultaneously blocks all of the molasses beams. On the way up, the launched atoms pass through two laser beams that optically pump many of the atoms into $6S_{1/2}, F = 4, m_F = 0$, which is the only state addressed by the atom interferometer. This Zeeman sublevel pumping increases the final atom signal by a factor of about 3.5.

After the initial state preparation into $6S_{1/2}, F = 4, m_F = 0$, the atoms enter into a region of the chamber isolated from external magnetic fields by a triple layer shield. A solenoid inside the innermost shield establishes a uniform bias field of about 72 mG along the direction of the Raman beams. This bias field shifts the energy levels of the magnetic-field sensitive transitions, so that the Raman lasers only address the atoms in the $m_F = 0$ state both for the interferometer transitions and for the final state-selective detection.

A second Ti:Sapphire laser is the source for the two Raman beams on the 895 nm cesium D_1 line. One beam is on resonance with the $6S_{1/2}, F = 3 \leftrightarrow 6P_{1/2}, F' = 3$ transition, and the other with $6S_{1/2}, F = 4 \leftrightarrow 6P_{1/2}, F' = 3$. Before reaching the vacuum chamber, AOM's shape the adiabatic passage pulses and allow rapid switching of the paths taken by the $F = 3$ and $F = 4$ light, as is needed to reverse \mathbf{k}_{eff} for the interferometer pulse sequences. After careful mode preparation and collimation, the 2-cm diameter beams enter the vacuum chamber from above and below. Polarizing beam-splitter cubes (PBS's) and quarter-wave ($\lambda/4$) plates cause the beams to have $\sigma^+ - \sigma^+$ polarization.

A diode laser beam copropagates with each adiabatic passage beam. These tracer beams measure the noise caused by the Raman beam optics. The upper PBS is part of an optical interferometer (not shown) that overlaps the upward- and downward-propagating tracer beams. A feedback loop corrects the Raman detuning to reduce the phase noise amplitude. In order for this process to properly correct for mirror vibrations, the optical interferometer measuring the beat note must itself be free of vibrational noise. We have constructed a quiet interferometer platform using a computer-based active vibration isolation system. The diode light is at 887 nm, well away from the cesium resonance, so it can be left on between pulses. Consequently,

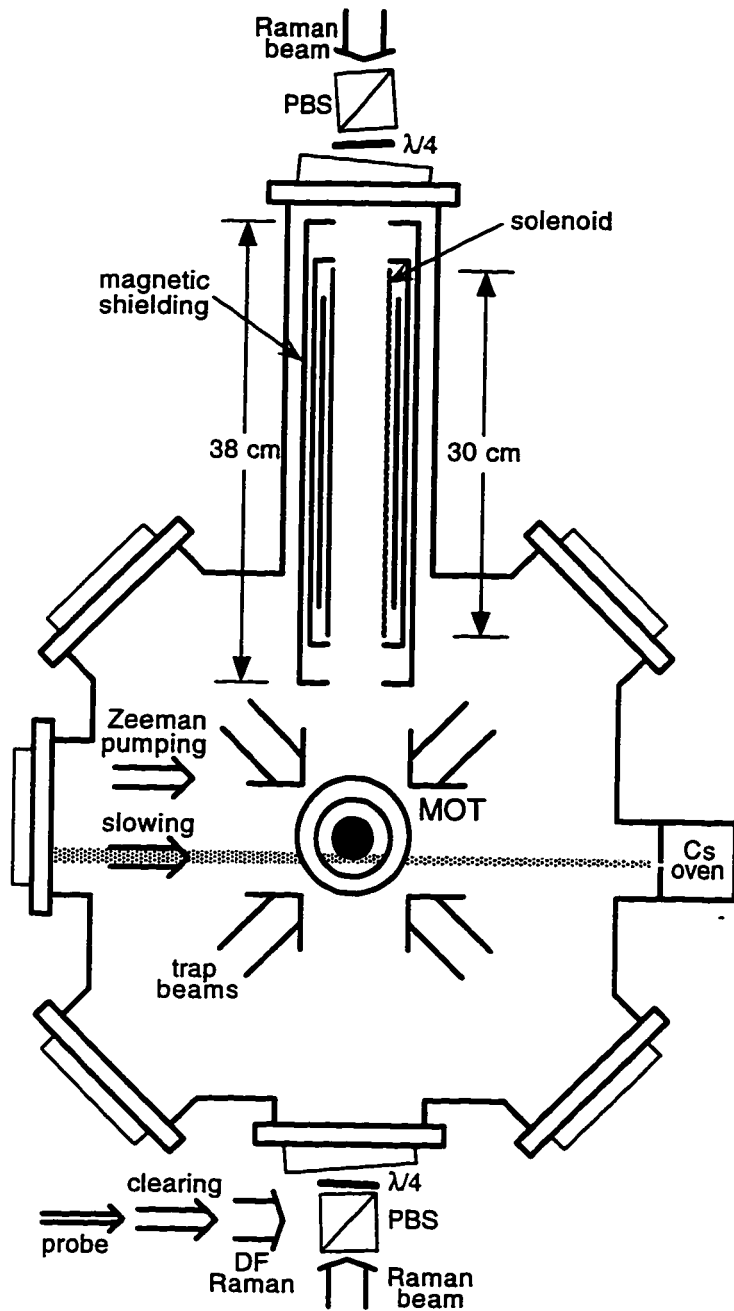


Figure 3.1: Overview of the experimental apparatus. Atoms are slowed from a beam, trapped, cooled, and launched in a vertical trajectory. After initial state preparation, vertical adiabatic passage beams create the interferometer pulse sequences. Vertical detection beams produce a fluorescence signal proportional to the number of atoms in one of the cesium ground state $m_F = 0$ sublevels.

the vibrational phase correction remains stable even when the Raman beams are turned off.

An initial long-duration, low-intensity pulse from the adiabatic passage beams preselects a narrow velocity class from the initial collection of launched atoms. The interferometer pulse sequences described in Sec. 2.3 follow this initial preselection. The shape of the final beam-splitter pulse in the interferometer sequence causes the signal atoms to be transferred into the $6S_{1/2}$, $F = 3$, $m_F = 0$ state. Since the beam polarizations are both σ^+ , a majority of the atoms that spontaneously emit are optically pumped into the $m_F = +3$ and $+4$ magnetic sublevels. Consequently, we perform a state-selective detection so that we only count the atoms that are the $F = 3$, $m_F = 0$ state. This improves the fringe contrast in the detected signal, which increases the immunity to amplitude noise in the number of detected atoms.

The Doppler-free Raman, clearing, and probe beams overlapped with the lower adiabatic passage beam form the basis for the detection process. First, a pulse of resonant $6S_{1/2}$, $F = 4$ to $6P_{3/2}$, $F' = 5$ light from the clearing beam blasts away any background atoms in the $F = 4$ ground state. Then a Doppler-free Raman π pulse transfers the signal atoms from $F = 3$, $m_F = 0$ to $F = 4$, $m_F = 0$. Finally, a second resonant $6S_{1/2}$, $F = 4$ to $6P_{3/2}$, $F' = 5$ pulse from the probe beam scatters light from the recently transferred $F = 4$ signal atoms. A PMT detects this scattered light. A computer numerically integrates and stores the PMT output. The computer controls the interferometer pulse sequences and Raman detuning to scan through interferometer fringes.

I have already presented some sample atom interferometer fringes in Fig. 2.11 for a Ramsey-Bordé interferometer with $T = 1$ ms and $N = 0$. We fit sinusoids of periodicity $1/T$ to each set of fringes. For that data, the fringe contrast of the least-squares best fit sinusoids is $27.0 \pm 0.5\%$. The maximum theoretical contrast is 33%. This slightly reduced contrast is probably because of optical wave-front distortions, poor adiabaticity in beam-splitter pulse transitions, or nonideal removal of background atoms. The measured separation between the two center frequencies is $\Delta f_{\text{rec}} = 30.0072(46)$ Hz, which represents a 150 ppm measurement of Δf_{rec} from 90 s of data. Peak precision occurs with experimental parameters of $T \approx 120$ ms and

$N \approx 30$, which yield a factor of ~ 1000 increase in the measurement resolution.

We collect data such as this by alternating between points on the two interferometers. This helps to reduce the effects of long-terms drifts of the lasers and the vibration isolation system. Also, after completing a measurement using a pair of interferometers, we create inverted interferometers by reversing the orientation of \mathbf{k}_{eff} for all of the interferometer pulses. This allows measurement and partial cancellation of errors from magnetic field variations and wave-front distortions. Chapter 4 will give further details about consistency tests performed on the recoil measurement.

3.2 Cesium fountain

The cesium fountain is nearly identical to that for the first generation photon recoil measurement [14, 15]. Only a few minor changes have been made to reduce the noise in the final probe signal for detecting the launched atoms. Consequently, I will give relatively brief coverage to the cold atom source, and devote more time to the newer features of this experiment, *e.g.*, the adiabatic passage beam generation, the magnetic shielding, and the vibration isolation.

A Schwarz Electro-Optic (SEO) Titan Ti:Sapphire laser provides all of the light near the $6S_{1/2}$, $F = 4 \leftrightarrow 6P_{3/2}$, F' transitions of the cesium D_2 line. This includes the beams for the slowing, trapping, Zeeman sublevel optical pumping, probe, and the frequency reference for the Doppler-free Raman laser. Reference [15] describes modifications to the laser that allow single-mode tuning over a 5 GHz range. A standard FM saturation spectroscopy lock [53] stabilizes the output frequency of this laser relative to the $F = 4$ to $F' = 4$, $F = 4$ to $F' = 5$ crossover line. A double-passed AOM in the lock provides a tunable offset for the laser output frequency, which is presently set to put the laser output about 90 MHz above the $F = 4$ to $F' = 5$ transition.

The cesium beam source consists of a cesium storage region at a temperature of about 85° C and a nozzle region at a higher temperature of about 200° C. The atoms exit the oven through a 0.6-mm diameter hole in the nozzle. After traveling about 50 cm, the beam passes through a movable aperture into the UHV section of the

vacuum chamber. Reference [13] describes the main vacuum chamber in detail. The only major recent change in the vacuum system is the addition of a Varian Vacuum titanium sublimation pump. Previously, a liquid nitrogen cryoshield provided the extra pumping speed needed to bring the pressure down to about 2×10^{-9} torr. (At pressures below about 5×10^{-9} torr, the loss of atoms from collisions with background atoms becomes negligible for a 1 sec cycle time.) Unfortunately turbulence of the liquid nitrogen within the cryoshield added vibrational noise to the system. Also, the liquid nitrogen caused thermal gradients that misaligned the adiabatic passage and tracer beams. The titanium sublimation pump keeps the pressure at a comparable pressure of about 1.5×10^{-9} torr for several weeks before needing recharging. Consequently, it operates very passively—improving our vacuum without adding noise to the experiment.

The slowing and trapping beams each consist of two frequency components, one near the $6S_{1/2}, F = 3 \leftrightarrow 6P_{3/2}, F' = 4$ transition, and the other near the $F = 4 \leftrightarrow F' = 5$ transition. The SEO Ti:Sapphire laser supplies the $F = 4$ light, while an external cavity diode laser [54] provides the $F = 3$ light. This $F = 3$ repumping light keeps atoms that are optically pumped into the $F = 3$ ground state from remaining there. An AOM combines the $F = 3$ and $F = 4$ light. An offset in the cesium lock for the repumping laser compensates for the frequency shift in this AOM, so that the $F = 3$ and $F = 4$ light have equal detunings from their respective transitions for both primary outputs of the AOM. One output of the AOM (about 280 MHz above resonance) becomes the slowing beam, and the other output (about 90 MHz above resonance) provides the trapping light.

The slowing beam counterpropagates with the atomic beam, scattering photons from the atoms to reduce their velocity so that they can be captured in the MOT. The peak of the velocity distribution of atoms leaving the oven is around 300 m/s, which causes a 350 MHz Doppler shift for the 852 nm transition. The actual light that performs the slowing is the -1 order from a traveling-wave EOM [55, 13]. The rf driver for the EOM chirps the frequency of this sideband from 270 MHz to 50 MHz below resonance over 5.5 ms to compensate for the Doppler-shift of the atoms as they decelerate. We set the rate and range of the chirp empirically to maximize the

loading rate into the MOT. This chirp rate of 36 MHz/ms is approximately 60% of the theoretical limit set by the maximum slowing force of $\hbar k \Gamma / 2$.

The MOT consists of six trap beams converging at the center of a quadrupole magnetic field. I will not discuss here the theory of operation of MOT's [56, 57, 58], but will describe the particular trapping conditions in this experiment. Two 4-cm diameter coils arranged in an anti-Helmholtz configuration generate the trapping magnetic field. The two coils are spaced 4 cm apart. Each coil consists of 5 turns of 5/16" copper tubing. Cooling water flows inside of the tubing. The maximum trap loading rate occurs with a current of 16 A in the trap coils, corresponding to a field gradient of about 15 G/cm in the center. Figure 3.1 depicts the orientation of the various trap beams. Three AOM's generate the three different frequency components for the lower, upper, and transverse trapping beams. The frequencies of all three beams are about 20 MHz below the $F = 3$ to $F' = 4$ and $F = 4$ to $F' = 5$ resonances during the trap loading process. These three AOM's provide both the independent control of beam frequencies needed for the launch, and independent control of beam intensities useful for optimizing the trap loading and polarization-gradient cooling. The trap beam diameters, intensities, and polarizations reported in Ref. [13] are still fairly accurate, so I will not discuss them further here.

After loading for about 200 ms, the MOT contains about 10^8 atoms. Then the launching sequence begins. First the trapping magnetic field shuts off. This allows polarization-gradient cooling to further lower the temperature of the atoms before the launch. To facilitate the cooling process, a collection of three $\sim 1\text{-m}$ diameter Helmholtz coils zeroes the magnetic field in the center of the trapping region. For a description of polarization gradient cooling see Refs. [59, 60, 61]. We found that the long 50 ms delay previously allowed for eddy currents to decay [13] before the launch is unnecessary and contributes noise to the final probe signal. Consequently, we decreased the delay to 5 ms. Next the trap beam AOM's shift the frequencies of the lower (upper) trap beams up (down) by about 2.2 MHz. This creates optical molasses in a frame traveling upward [52] at 2.72 m/s. After allowing 400 μs for the atoms equilibrate to this new velocity, the trap beam AOM's lower the beam intensities to roughly 5% of their initial levels. This further reduces the equilibrium temperature

for the polarization gradient cooling. After about 2 ms, a mechanical shutter located near the focus of the primary trap beam simultaneously blocks all six beams. This helps to keep edge effects on the trap beams from disturbing the launch and also protects the atoms from near-resonant light during the sensitive atom interferometry measurement. This launch starts the atoms on a trajectory that reaches a nominal height of 37.7 cm above the trap. (The actual trajectory height varies significantly with the number of photon recoils delivered by the interferometer pulses.)

The final step before the atom interferometer sequence is to prepare the internal states of the atoms. This is accomplished as the atoms pass through the Zeeman pumping beam in Fig. 3.1. This beam is actually two slightly displaced beams. The lower beam is on resonance with the $6S_{1/2}, F = 4$ to $6P_{3/2}, F' = 4$ transition and is linearly polarized in the vertical direction. Immediately after the trap beam shutter closed, the three Helmholtz coil currents switched to new levels which created a bias field in the vertical direction. Since the light polarization matches the bias field direction, $F = 4, m_F = 0$ is a dark state for the light. Consequently, any atoms that fall into that state remain in that state and no longer scatter photons (neglecting impurity of polarizations and off-resonant excitation), so we enhance the population of the $F = 4, m_F = 0$ state. The Zeeman pumping beam is retroreflected to minimize the deflection of the atomic trajectory. Of course, the spontaneous emission inherent in this optical pumping process also heats the atoms as it transfers them into $F = 4, m_F = 0$. Since we are primarily interested in maximizing the total fluorescence signal from the probe beam of Fig. 3.1 that is detected by the PMT, we set the Zeeman pumping intensity to peak up the PMT signal. This probe signal typically increases by a factor of about 3.5 when the Zeeman pumping light is unblocked. Note that this factor includes the loss of signal from additional heating of the atoms. The actual polarization of the atoms into the $F = 4, m_F = 0$ state is considerably higher than this factor would indicate. The upper component of the Zeeman pumping beam is on resonance with the $6S_{1/2}, F = 3$ to $6P_{3/2}, F' = 4$ transitions. It keeps the atoms pumped into the $F = 4$ ground state. It is displaced slightly above the $F = 4$ to $F' = 4$ beam because our state-selective detection scheme (see Sec. 3.4) assumes that the launched atoms are in the $F = 4$ state, so a background in the $F = 3$ state can

cause mismeasurement of the signal levels. Reference [15] contains more details on the performance of the Zeeman pumping.

3.3 Velocity-selective Raman transitions

The next step in the experiment cycle is the creation of the light-pulse atom interferometer. As discussed in Chapter 2, velocity-selective Raman transitions provide the high sensitivity to the photon recoil needed for the measurement. In particular, this version of the measurement uses adiabatic passage to drive the two-photon transitions. The use of Doppler-sensitive adiabatic passage transitions calls to the forefront several important experimental considerations, including especially magnetic-field control, Raman frequency generation, and vibration isolation. These aspects of the experiment will be the subject of this section.

The main contributing factor to the order-of-magnitude increase of sensitivity of this version of the recoil measurement over the first generation experiment is the switch from horizontal to vertical interferometer beams. Two main reasons encouraged the former use of horizontal beams. First, in that geometry, gravity did not shift the transitions, so excursions of the Raman beam difference frequency were small, only needing to compensate for the photon recoils and a small horizontal velocity component in the trajectory. Additionally, adequate vibration isolation to below 1 Hz was achieved passively with a horizontal air rail. Unfortunately, however, the short time the atoms remained near the center of the 2-cm diameter laser beams limited the $\pi/2$ separation to $T \approx 25$ ms. Also, generating a uniform bias field over the trajectory would have been difficult with large diameter horizontal beams. With vertical Raman beams, however, the atoms remain in the beam and the bias field is sufficiently uniform to guarantee low quadratic Zeeman shift errors for up to $T \approx 200$ ms. The vertical geometry also allows partial cancellation of wave-front phase errors since the atoms stay at nearly the same radial positions in the beams for all of the interferometer pulses.

3.3.1 Magnetic fields

All of the atom interferometer transitions occur on the magnetic-field insensitive $6S_{1/2}$, $F = 3$, $m_F = 0 \leftrightarrow F = 4$, $m_F = 0$ transition. The frequency difference of these levels is not completely insensitive to magnetic fields. Although no linear dependence exists, it is subject to a quadratic Zeeman shift of [62]

$$\Delta\nu_{\text{QZS}} \approx \alpha_B B^2, \quad (3.1)$$

where $\alpha_B = 4.27 \times 10^{-4}$ Hz/(mG)². In this experiment, the exact value of the energy level splitting is irrelevant, so long as it is the same for all of the interferometer pulses. Consequently, we do not care about an overall quadratic Zeeman shift, only spatial variations in the shift caused by nonhomogeneous magnetic fields. The sensitivity of an atom interferometer to the quadratic Zeeman shift has the form

$$\delta(\Delta\nu_{\text{QZS}}) \approx 2\alpha_B B \delta B, \quad (3.2)$$

where δB is the difference of the magnetic-field amplitude between two interferometer trajectories.

A conservative goal for the magnetic-field design is to keep quadratic Zeeman shift errors below about 5 ppb in Δf_{rec} , or 150 μ Hz. Assuming that we can achieve a recoil enhancement factor of $N \approx 30$, this sets a limit of 4.6 mHz on the frequency shift difference between beam-splitter pulses. Equation (3.2) suggests that a small bias field $B \sim 1$ mG would easily meet our goal. Unfortunately, two problems arise with such a small bias field—the introduction of a potentially devastating systematic shift of the measurement and a reduction of fringe contrast. Most seriously, we begin involving linearly sensitive magnetic sublevels $m_F \neq 0$ in the recoil measurement. With such a low bias field, the typical ~ 100 kHz frequency widths of the adiabatic passage pulses cover the entire energy spread of the magnetic sublevels. If the magnetic field is sufficiently uniform, then we would actually observe fringes from these atoms, but the fringes would be severely shifted in phase by nonhomogeneities in the magnetic field (roughly 10^6 times worse than for the $m_F = 0 \leftrightarrow 0$ transition). The superposition of these fringes on those for the magnetic-field insensitive transition could severely disturb the recoil measurement. From the huge amplitude of the linear Zeeman shift,

for large T , field nonhomogeneities would probably cause the phase of the fringe shift to vary widely for atoms in slightly different trajectories, causing the fringes to mostly wash out. This is good for reducing systematic errors, but if these atoms are driven by the interferometer pulses and detected, then they contribute to background signal, which reduces the overall fringe contrast. Since signal normalization with adiabatic passage is troublesome (see Sec. 5.1.4), amplitude noise is a real limitation of the measurement. A reduction of fringe contrast rapidly decreases the precision of the determination of fringe center frequencies.

Our solution for dealing with magnetic-field shifts is to make the bias field large enough to eliminate the linearly sensitive transitions, but sufficiently uniform to rule out problems from the quadratic Zeeman shift. To accomplish this, all of the interferometer pulses occur while the atoms are within a triple layer magnetic shield, as shown in Figure 3.1. We designed the dimensions and spacing of the 0.025"-thick Hipernom shields to provide radial and axial shielding factors of 1.3×10^6 and 8400, respectively [63]. In practice, the actual shielding factors may be less than this, especially for time-varying fields. A tightly wrapped solenoid inside of the innermost shield creates a uniform bias field in the vertical direction. The solenoid consists of Kapton-insulated wire wrapped on an aluminum cylinder 30 cm long and 5 cm in diameter. The wire winds continuously down the cylinder and back, giving a total turns ratio of $n = 19 \text{ cm}^{-1}$. Two small auxiliary 8-turn trim coils ($\approx 9 \text{ turns/cm}$) on each end of the solenoid fine-tune the uniformity of the field to reduce edge effects.

Rather than characterizing the actual shielding factors of the magnetic shielding, we proceeded straight to the bottom line: Is the bias field inside of the shielding sufficiently uniform for the photon recoil measurement? To determine this we modified the Doppler-free Raman transitions normally used for the detection (see Sec. 3.4.1). Instead of having the two-photon difference frequency tuned to the $F = 3, m_F = 0$ to $F = 4, m_F = 0$ transition, we changed it to drive the $F = 3, m_F = 3$ to $F = 4, m_F = 3$ transition and reset the π pulse time to account for the change of matrix elements. This transition is linearly sensitive to magnetic fields, but it is Doppler-free, so it is insensitive to atomic velocities. Consequently, a Doppler-free Raman π pulse on this transition makes a good probe for the magnetic field experienced by the

atoms along the trajectory.

Converting the experiment over for this magnetic field probe requires only a couple of changes. First, since we want to measure the field above the normal launch height, we increase the launch velocity to about 2.93 m/s. At this velocity, the trajectory peaks at a height of 44 cm above the trap. Next, we need a supply of atoms in the $F = 3, m_F = 3$ state. Blocking the repumping light normally overlapped with the Zeeman pumping light provides these atoms. Since the initial atoms from the trap are spread throughout the $F = 4$ magnetic sublevels, the $F = 4$ to $F' = 4$ light rapidly optically pumps the atoms into the $F = 3$ state with some going into the $F = 3, m_F = 3$ sublevel. A pulse of on-resonant $F = 4$ to $F' = 5$ light blasts away all atoms remaining in $F = 4$, particularly in the $F = 4, m_F = 0$ dark state. The Doppler-free π pulse transfers the $F = 3, m_F = 3$ atoms to the $F = 4, m_F = 3$ state, which we can detect in the normal manner (see Sec. 3.4.2 for details on the probe detection). Finally, we modified the computer program that normal scans the Raman detuning of the adiabatic passage beams to instead control the detuning of the Doppler-free Raman laser. This allows us to scan through the Doppler-free Raman resonance. The center frequency of the resonance is directly proportional to the magnetic-field amplitude at the location where the atom-light interaction occurs. Varying the time of the Doppler-free π pulse probes the magnetic field at different spatial locations.

Figure 3.2 is a map of the magnetic field along the atomic trajectory with the bias field set to about 72 mG, which is the empirically determined field amplitude at which the interferometer fringe contrast reaches a plateau. Note that the field amplitude actually increases at the ends of the solenoid. This occurs because of the gradual decay within the magnetic shielding of the 500 mG external bias field (used for the Zeeman pumping). A comparison of the field measurements for ascending and descending atoms clearly reveals that variations of the field amplitude in the vertical direction are more serious than any radial variations caused by the transverse motion of atoms in the solenoid. Without the trim coils, the field is acceptably uniform for roughly 10 cm along the solenoid. Proper adjustment of the trim coils extends the usable region to about 23 cm, which is over 75% of the total length of the solenoid. In Sec. 3.3.1, I will use Fig. 3.2 to estimate the magnitude of errors in the recoil

measurement from quadratic Zeeman shifts.

3.3.2 Adiabatic passage beam generation

The switch from stimulated Raman transitions in the original recoil measurement [15] to adiabatic passage in this version of the measurement has incurred a significant amount of work to overcome new technical challenges. Chief among those is the sensitivity of adiabatic passage to the purity of the laser frequencies. As described in Sec. 2.2.2, the presence of extra frequency components in the beams can easily lead to significant spontaneous emission losses or ac Stark shifts if not sufficiently far detuned.

In the previous recoil measurement using velocity-selective stimulated Raman transitions, it was possible to have both of the Raman components overlapped in a single beam, then retroreflected after passing through the vacuum chamber. Since we launched the atoms with a nonzero velocity along the direction of \mathbf{k}_{eff} , we could use the Doppler shift of the two-photon detuning to select which pair of velocity-sensitive beams drives the transition. This approach had several important advantages. First, since k_1 and k_2 only differ by 3×10^{-5} , the Doppler shifts of the two beams from common mirror vibrations are nearly identical for the two beams, so they cancel with high accuracy in the Raman detuning. Since only one of the two driving beams reflects off of the final mirror, Doppler shifts from that mirror do not cancel. Consequently, the problem of obtaining stable laser phases reduces to vibrationally isolating the final retroreflection mirror. With simple passive isolation of this mirror, we experimentally realized interferometer interaction times up to about 50 ms [14]. Secondly, reversing \mathbf{k}_{eff} is a simple matter of inverting the sign of the Raman detuning—a physical switching of the beams is unnecessary. Additionally, we only had to maintain high beam quality along one path to the vacuum chamber. Finally, guaranteeing precise counterpropagation of \mathbf{k}_1 and \mathbf{k}_2 is very simple with a retroreflection.

Unfortunately, retroreflection of a pair of overlapped beams is completely out of the question for adiabatic passage with $\Delta = 0$. Although only one counterpropagating pair will have a dark state that matches the velocity of the atoms, the other pair is still

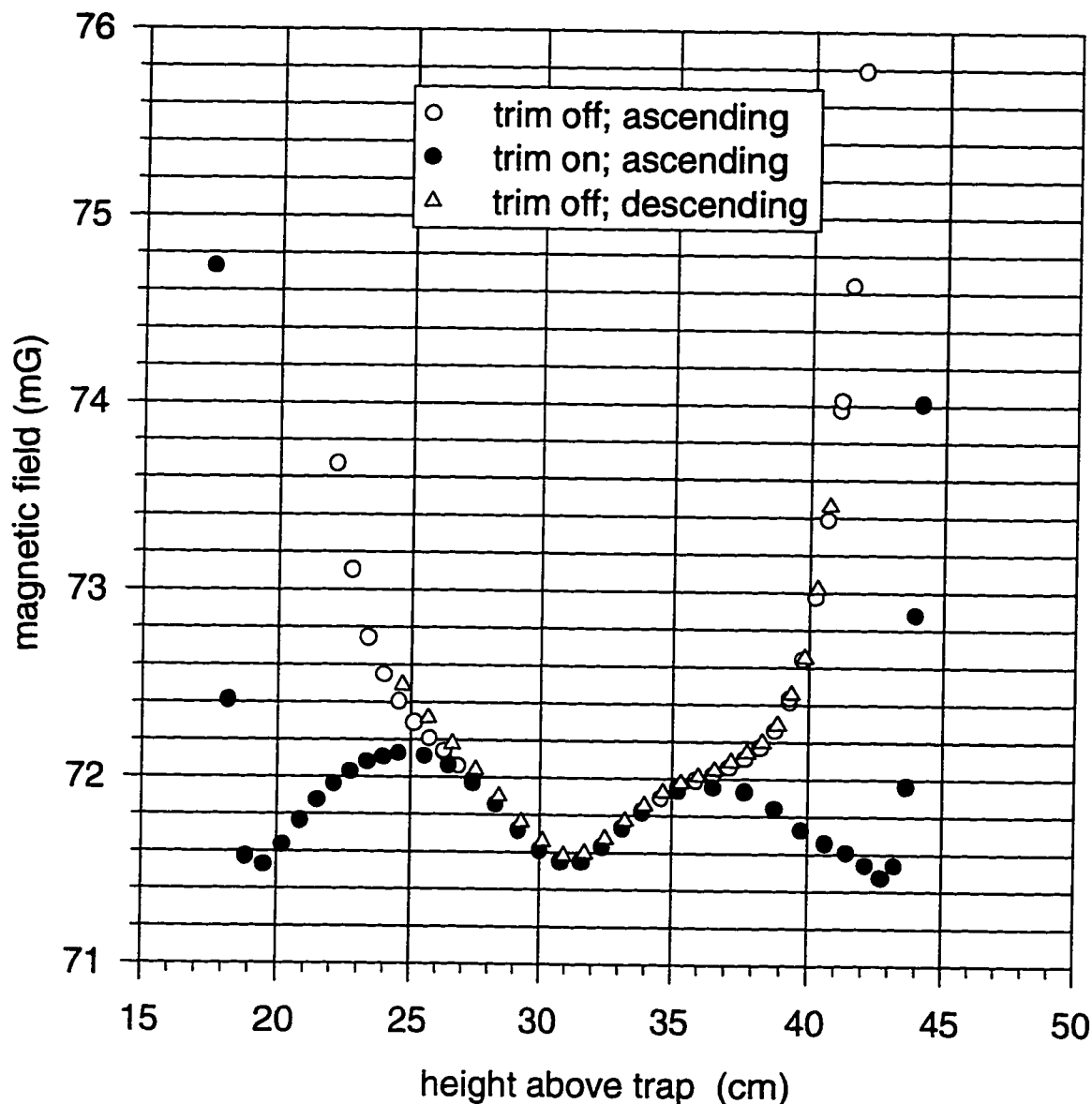


Figure 3.2: Magnetic-field profile along the atomic trajectory. The field measurements agree for ascending and descending atoms. Using the trim coils at the ends of the solenoid, we have achieved a uniformity of 0.6 mG over 23 cm for a 71.8 mG bias field. This allows total interferometer times of up to 430 ms.

on resonance with the one-photon transition, so it will scatter photons from the atoms. Consequently, the method of generating the adiabatic passage beams must maintain a high level of purity of the beam frequencies. Figure 3.3 outlines the process by which we generate the adiabatic passage beams. Independent optical paths bring the beams to the vacuum chamber. At the one point where the beams must copropagate, between PBS2 and PBS3, the combination is performed with a high-quality calcite polarizer (PBS2), and we carefully avoid the use of any birefringent optical elements that could mix the two frequencies before a second calcite polarizer (PBS3) splits the beams again. The following sections will describe the various components of this optical setup.

Optical frequency source

Several methods exist for producing the microwave frequency offset between frequencies ω_1 and ω_2 . These include an optical phase-locked loop between two independent lasers, frequency modulation with an electro-optic modulator, and direct modulation of a diode laser junction current [64]. The initial photon recoil measurement used the first method. Two independent external cavity diode lasers supplied the two Raman frequencies. A phaselock fixed the heterodyne beatnote between these two lasers relative to an rf reference signal. In the present experiment, we are using the second and third methods for the adiabatic passage beams and the Doppler-free Raman beams, respectively. Below I describe the electro-optic method used for the adiabatic passage beams. Discussion of the direct modulation approach will be reserved for Section 3.4.1.

A potentially useful electro-optic frequency generation approach is to drive the EOM near $\omega_{ab}/2$ and use the ± 1 sidebands for the Raman frequencies. The chief limitation of that method is the difficulty of shaping the optical pulses. A single beam intensity control can create stimulated Raman pulses such as in Fig. 2.6(a). Unfortunately, creating the types of pulses needed for adiabatic passage, such as Fig. 2.6(b), requires separating the two frequency components and individually controlling their intensities, *e.g.*, with an AOM.

Alternatively, we have chosen to use the primary output of a Ti:Sapphire laser

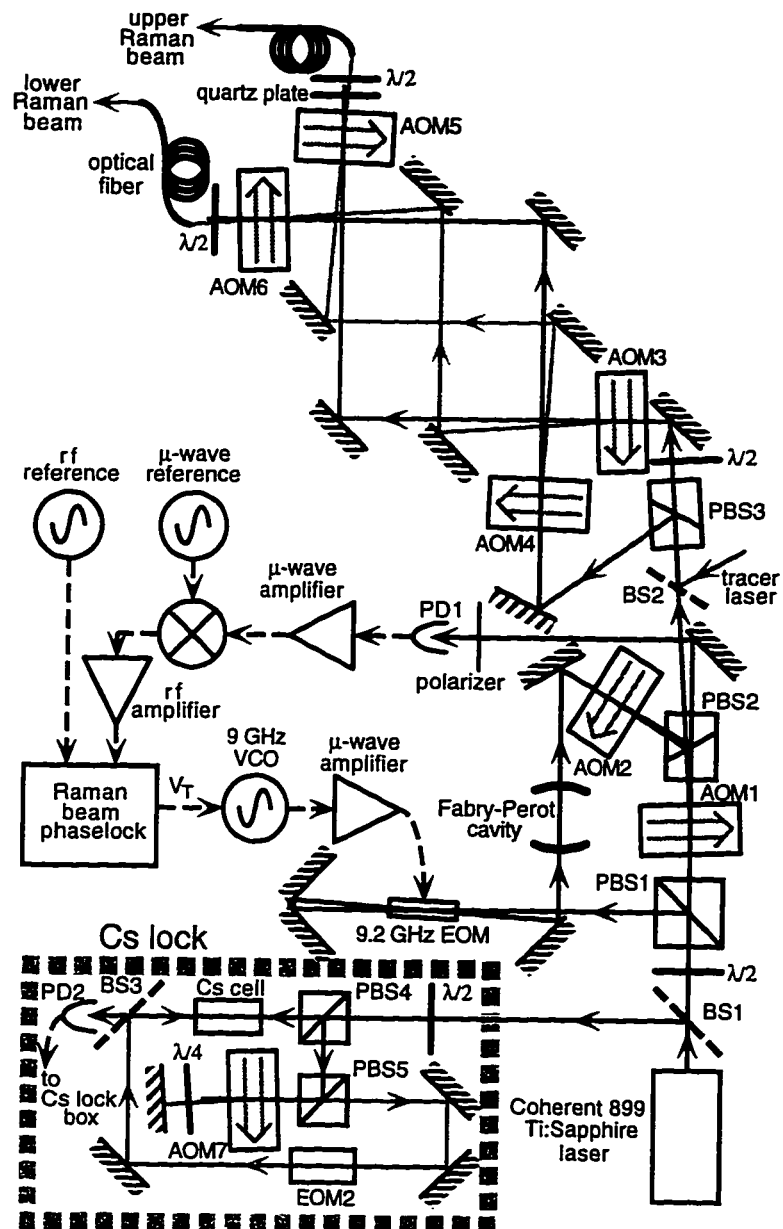


Figure 3.3: Adiabatic passage beam generation. A single Ti:Sapphire laser supplies both Raman beam frequencies. The absolute frequency of the laser is stabilized to cesium. AOM1 and AOM2 shape the adiabatic passage pulses. AOM3–AOM6 switch the orientation of k_{eff} . The frequencies of AOM3 and AOM5 are actively adjusted to correct for vibrational and phase noise from the Raman beam optics. The arrows on the AOM's indicate the direction of the acoustic traveling waves.

for one of the Raman frequencies and generate the second frequency component with an EOM modulated near 9.2 GHz. Various AOM frequency shifts in the beam paths guarantee that only a single pair of beams exactly matches the Raman transition frequency. In addition, a Fabry-Perot cavity filters out most of the light from the carrier and unwanted sidebands. Two goals motivated the switch from diode lasers to a Ti:Sapphire laser for the Raman beams. The first was simply to obtain higher Raman beam powers so that we could address a larger fraction of the cold atoms. Secondly, diode lasers naturally have a large noise bandwidth, so phaselocking is more difficult than for the electro-optic scheme described here. By generating both Raman beams from the same laser, most of the frequency jitter of the laser cancels out in the Raman detuning $\omega_1 - \omega_2$. Consequently, the only need for a phaselock is to remove vibrations from optics and to eliminate frequency-dependent phase shifts from the response of the resonant EOM, microwave amplifier, *etc.*

A Coherent 899 Ti:Sapphire laser supplies the Raman beam light. The Ti:Sapphire output frequency is nominally 60 MHz below the $6S_{1/2}$, $F = 4 \leftrightarrow 6P_{1/2}$, $F' = 3$ transition near 894.6 nm. (The actual detuning makes excursions of about ± 2 MHz around that frequency to compensate for Doppler-shifts of the one-photon detuning caused by the motion of the atoms.) A -40 MHz frequency shift from AOM1 and a $+100$ MHz shift from AOM3 or AOM5 in Fig. 3.3 then puts this beam directly on resonance when it interacts with the atoms.

The absolute frequencies of the Raman beams are important because they set the size of the photon recoil and because nonzero detunings from resonance can cause ac Stark shifts in the adiabatic passage transitions, as shown in Fig. 2.8. Consequently, we took more care with the cesium lock for this laser than for the slowing and trapping laser. Here we use the modulation transfer technique [65, 66, 67] to lock the laser to the saturated absorption signal from a cesium cell, as shown in Figure 3.3. The main difference between this lock and a standard FM lock [53] is that the EOM modulates the pump beam instead of the probe beam. Consequently, the only modulation that can be present in the probe signal is modulation that is transferred via the atoms. This can reduce the rf background caused by amplitude modulation of the probe beam by the EOM. Additionally, the completely antisymmetric lineshape from

modulation transfer is conducive for an accurate and stable lock. As the relative phases of the reference and probe signals vary for standard FM spectroscopy, the lineshape continuously varies from a Lorentzian to a dispersive feature. This causes the zero-crossing—which is generally the lock point—to shift. An ideal modulation transfer signal, on the other hand, is completely antisymmetric, regardless of the mixing phase. Consequently, although the slope through the zero-crossing changes with the mixing phase, the zero-crossing itself never shifts. We did observe, however, that care must be taken with the lock to achieve a truly antisymmetric lock signal. Initially we did not focus the pump beam through the EOM crystal, and spatial inhomogeneity in the EOM crystal caused amplitude modulation of the pump beam sufficiently serious to distort the modulation transfer lineshape, causing errors of up to ± 1 MHz. Now that we have fixed that problem, however, the modulation transfer signal remains antisymmetric regardless of the phase.

The driving frequency of the EOM is $0.7\Gamma \approx 3.5$ MHz, which gives the peak slope for the modulation transfer signal [67]. A double-passed AOM (AOM7) provides a quickly tunable offset frequency for the cesium lock. An HP33120A arbitrary waveform generator controls the tuning voltage for that AOM driver. For each pulse of an interferometer, the arbitrary waveform pattern shifts the cesium lock offset to compensate for the Doppler-shift of the $F=4$ light from the one-photon transition. To properly correct the actual laser detuning, the bandwidth of the cesium lock must be sufficiently fast to follow the changing lock offset between the ~ 1 -ms spaced pulses. We made a simple modification to the Coherent Ti:Sapphire control electronics that allows fast frequency control via the tweeter. By a combination of control and feed-forward signals to the tweeter and to the EXT SCAN input of the control electronics, we achieved a settling time of about 1 ms for the cesium lock. The ± 2 MHz detunings from Doppler-shifts are reduced to less than ± 200 kHz by the cesium lock control electronics. This is sufficient for our present needs, as I will discuss further in Sec. 4.2.2. In the following sections I will provide more details on the arbitrary waveform patterns for the cesium lock offset and the feed-forward control.

We regularly check the absolute accuracy of this lock using cold atoms. With the laser locked to cesium, we apply a $100\ \mu\text{s}$, $10\ \mu\text{W}/\text{cm}^2$ pulse of $6S_{1/2}, F = 4 \leftrightarrow 6P_{1/2}$,

$F' = 3$ light to the atoms while they are at the top of the trajectory. This pulse pumps some atoms into the $F = 3$ ground state. Standard blasting, Doppler Raman π , and probe pulses (see Sec. 3.4) provide a signal proportional to the number of atoms that happen to fall into the $F = 3, m_F = 0$ state after the initial pulse. The computer steps the cesium lock offset frequency through resonance to measure the cesium one-photon lineshape. Then it fits a Lorentzian to the data. The center of the Lorentzian is the offset of the lock from resonance with the cold atoms. In this manner, we observe that the resonance center drifts around roughly 100 kHz(rms). This is several times larger than any of the uncertainties related to the cold atom measurement, so it is quite certainly an error in the cesium lock. That level of accuracy is sufficient for this measurement (see Sec. 4.2.2).

A New Focus Model 4841 9.2 GHz resonant cavity EOM generates the $F = 3$ Raman component from part of the main Ti:Sapphire output. This is a custom unit with a $0.5 \times 1.0 \times 33.4$ mm MgO:LiNbO₃ crystal coated for 850 nm. The crystal dimensions and electrical connections cause it to act as a resonant cavity for microwave radiation at a frequency of about 9.2 GHz. As shown in Fig. 3.3, the Ti:Sapphire light passes through the EOM twice. With the distance of the retroreflection properly adjusted, the modulation from the second pass adds constructively to the modulation from the first pass. Under these conditions, the EOM output has maximum power ($\approx 30\%$) in the first-order sidebands with a microwave drive power of about 600 mW.

The output of the EOM next passes through a Fabry-Perot cavity. The purpose of this cavity is to transmit only the +1 order from the EOM, which is near the $6S_{1/2}, F = 3 \leftrightarrow 6P_{1/2}, F' = 3$ resonance. Initially we had the cavity length set for confocal operation. A confocal cavity has the advantage that transverse modes are degenerate, so that it is fairly easy to make sure that the cavity highly attenuates all undesired frequency components. Unfortunately, the degeneracy of the transverse modes also means that the cavity does very little spatial filtering of the mode distortion caused by the EOM. To avoid having the broad spray of light leak straight through to the fiber, we needed additional spatial filtering after the Fabry-Perot cavity that required about a 40% loss of optical power. We found that, for the same level of leakage light, the Fabry-Perot could do a more efficient job of spatial filtering if we increased

the cavity length to make it nonconfocal. The nondegeneracy of transverse modes for a nonconfocal cavity increases the danger of undesired frequency components transmitting through the cavity along with the +1 order. We fine-tuned the cavity length to try to avoid any strong modes near the +1 sideband. The Fabry-Perot cavity suppresses undesired frequency components by up to about 35 dB. A dither lock using the back mirror of the cavity stabilizes the cavity to the +1 sideband. The finesse of the cavity is sufficiently high that typical 2 MHz shifts of the $F = 3$ light frequency cause about a 25% decrease in the cavity transmission. Although adiabatic passage is fairly insensitive to beam intensities, after 50 adiabatic transfer pulses, this causes about a 30% decrease in the signal amplitude. The cavity lock only has about a 100 Hz bandwidth, so it is not fast enough to follow the light frequency for the interferometer pulses, many of which are spaced less than 1 ms apart. Consequently, custom-built lock electronics allow a feed-forward signal to more rapidly adjust the cavity during the interferometer sequence. This reduces the intensity fluctuations to about 10% of the peak intensity level. This is still one of the weak links of the frequency-shifting electronics, as I will discuss further in Sec. 5.1.3.

Interferometer pattern generation

The creation of an adiabatic passage interferometer pulse sequence requires a number of different control signals for beam intensities, frequencies, orientations, etc. These control signals are all generated and programmed by the QuickBasic program AltInt4X.BAS that controls the experiment. Table 3.1 lists the various control signals, the hardware that outputs the sequence, and the purpose of the signal. For brevity, I will refer to these patterns by the names listed in this table. I will first make a few general comments about the pattern generation, and then I will discuss the individual patterns in greater detail.

A Keithley-Metabyte PCIP-AWFG/2 board generates a majority of the waveforms. This is an arbitrary waveform generator PC board that is mounted inside of the computer that controls the experiment. It has two analog outputs and eight digital outputs. The two analog outputs control the adiabatic pulse shapes for the $F = 3$ and the $F = 4$ light. The digital outputs control the strobe for the Raman

Table 3.1: Control waveforms for adiabatic passage atom interferometers.

Interferometer control waveforms		
Name	Source	Description
$F = 3$	PCIP-AWFG/2	Adiabatic passage pulse shapes for $F = 3$ light
$F = 4$	PCIP-AWFG/2	Adiabatic passage pulse shapes for $F = 4$ light
3+4	PCIP-AWFG/2	Common switch for $F = 3$ and $F = 4$ light
$k_{\text{eff}} \uparrow$	PCIP-AWFG/2	Set optical switch for k_{eff} upward
$k_{\text{eff}} \downarrow$	PCIP-AWFG/2	Set optical switch for k_{eff} downward
STROBE	PCIP-AWFG/2	Update DDS-1EB frequency reference output
GATE	DS345	Gate signal for pausing PCIP-AWFG/2 waveforms
FSK	DDS-1EB	Frequency reference for Raman detuning
FF	HP33120A	Feed-forward signal for cavity and cesium locks
CS	HP33120A	Tuning voltage for cesium lock AOM

detuning synthesizer pattern (STROBE), the orientation of the Raman beams ($k_{\text{eff}} \uparrow$ and $k_{\text{eff}} \downarrow$), and a digital intensity control common to the $F = 3$ and $F = 4$ light (3+4). Several features of this board particularly recommend it for this experiment. First, we need to rapidly (< 500 ms) switch between at least four interferometer patterns. Since this board is mounted inside the computer, patterns can be rapidly programmed and changed over the PC bus. Additionally, the board has a special gating feature that allows it to output high resolution patterns for long interferometer sequences with long dead times.

Initially when we began adiabatic passage interferometry, we were generating the adiabatic passage pulse shape waveforms using HP33120A synthesizers. These have the useful feature of four arbitrary waveform memories, which allowed us to rapidly switch between interferometers. Unfortunately, the pattern resolution achievable with these waveform generators was insufficient. The total interferometer duration may be as long as about 400 ms. With a maximum length pattern of 32,000 points, the time step size for a 400-ms long pattern is 12.5 μs . Since a typical adiabatic passage pulse is $\sim 250 \mu\text{s}$ long, this yields very poor resolution. We obtained improved performance of the adiabatic passage transfer pulses with simple RC filters on the intensity control signal lines to smooth out the steps, but this also reduces the precision of the timing

of the beam-splitter pulses. Consequently, we would prefer a waveform generator that allowed higher resolution definitions of these patterns. The gate input on the PCIP-AWFG/2 board controls the internal clock that steps through the output waveforms. By stopping the internal clock, we can pause the output waveforms during long quiescent periods, *e.g.*, between beam-splitter pulses. To use this feature, we program a gate signal (GATE) in a Stanford Research Systems (SRS) DS345 synthesizer. The gate signal enables the PCIP-AWFG/2 internal clock whenever one of the analog or digital outputs must make a transition, then turns it off again after the pulse or transition is completed.

A SCITEQ DDS-1EB synthesizer outputs the reference frequency for the Raman detuning δ . This board has an external reference input for a 25-MHz square wave, 32 parallel digital inputs to set the output frequency, and a strobe input that tells the board to read the digital inputs and update the output frequency. The board changes the output frequency in a phase-continuous manner, which is crucial for the beam-splitter pulse pairs in the Ramsey-Bordé interferometer. A National Instruments AT-DIO-32F board transfers arrays of frequency data in computer memory to its 32 digital outputs, which connect to the DDS-1EB frequency control inputs.

To obtain consistent interferometer fringe results, it is crucial to avoid jitter between the amplitude and frequency patterns. The patterns for which this is particularly important include $F = 3$, $F = 4$, $3 + 4$, STROBE, GATE, and FSK. (The remaining patterns— $k_{\text{eff}} \uparrow$, $k_{\text{eff}} \downarrow$, FF, and CS—do not have critical timing since they only switch when the light is off, and no phase memory exists.) To gauge the potential magnitude of this jitter problem, suppose that we are measuring fringes for interferometers with spacing $T = 120$ ms between beam-splitter pulses. To compensate for gravity, the DDS-1EB frequency must change about 2.4 MHz between beam-splitter pulses. Further suppose that the transitions of the DDS-1EB strobe inputs nearly coincide with the DDS-1EB clock transitions. Then the actual time of the frequency update may have a jitter of 1 DDS-1EB clock cycle, or 40 ns, from one cycle to the next, or even from one pulse to the next. A shift in the time of the frequency change between two beam-splitter pulses by one clock cycle causes a shift of the reference signal phase of $2\pi(2.4 \text{ MHz})(40 \text{ ns}) \approx 0.6 \text{ rad}$. This would be the dominant source

of phase noise in the experiment. Furthermore, temperature-dependent phase shifts could cause a wandering systematic shift of the recoil result. Here we mainly focus on eliminating jitter on the scale of a clock cycle. Smaller random jitter will not cause noticeable noise and should average out.

Two requirements exist for eliminating clock-cycle magnitude timing jitter. First we must provide all sensitive patterns with synchronous time bases. Also we must ensure that any trigger or strobe line from one device to another has transitions that occur between clock cycle transitions for the receiving device. An advantage of the PCIP-AWFG/2 board is that it eliminates the possibility of timing jitter between the majority of the time-critical patterns. Since the board stores the $F = 3$, $F = 4$, $3+4$, $k_{\text{eff}} \uparrow$, $k_{\text{eff}} \downarrow$, and STROBE signals in parallel memory locations, and cycles through the memory with a single pointer, it is impossible for these patterns to shift relative to each other by a clock cycle. Consequently, the problem simplifies to removing jitter for interactions between the SRS synthesizer (GATE), the PCIP-AWFG/2 board, and the DDS-1EB board.

We provide synchronous timebases for all three of these devices. This required the first of two hardware modifications to the PCIP-AWFG/2 board. This board had a 20 MHz crystal for its internal clock. We removed this crystal and replaced it with a 20 MHz external clock signal from the doubled 10 MHz output of an SRS Loran C receiver (converted to TTL using a comparator). The GATE synthesizer already has an external clock input, so we also provide it with a Loran C 10 MHz signal. The DDS-1EB requires a 25 MHz clock. To achieve a 25 MHz signal synchronous with Loran-C, we phaselock a 100 MHz voltage-controlled oscillator (VCO) to a 10 MHz reference using an ECL decade divider for the 100 MHz signal. An ECL binary counter divides the 100 MHz signal down to the 25 MHz clock needed for the DDS-1EB board.

We have also ensured that no jitter arises from interconnecting control lines. The relevant signals include the SRS synthesizer output driving the PCIP-AWFG/2 gate input and the PCIP-AWFG/2 output driving the DDS-1EB strobe input. First we fixed the gate transitions relative to the PCIP-AWFG/2 clock. The external trigger input and the 40 MHz clock (phaselocked to 10 MHz from Loran C) determine the location of the gate signal transitions. Normally, the interferometer pattern start

trigger comes from an SRS DG535 digital pulse generator. The experiment cycle triggers relative to the 60 Hz line to reduce the effects of line noise, especially electrical noise on the PMT signal and phase noise on the frequency references. To adjust the gate signal transitions, we control the location of the external trigger transitions by gating it with a signal from the PCIP-AWFG/2 board. Unfortunately, the PCIP-AWFG/2 board has no continuous clock output that would be appropriate for gating the interferometer trigger. Obtaining such a signal required the second hardware modification on this board. The permissible output rates for arbitrary waveforms are $(5 \text{ MHz})/n$, where n is an integer. We coupled out from the board a continuous signal at this pattern sampling frequency. Since the 40 MHz and 25 MHz clocks of the other two crucial devices are multiples of $(5 \text{ MHz})/n$, this signal serves as a good gate for the interferometer trigger signal; if we start the gate signal relative to this signal, then all transitions will occur at fixed phases relative to the timebases. The PCIP-AWFG/2 pattern resolution never drops below about $2 \mu\text{s}$ for our typical interferometer patterns. A $2 \mu\text{s}$ shift of the interferometer pulses relative to line does not cause a significant change in the coupling in of line noise. Also, the $\sim 70 \text{ kHz}$ frequency width of the initial velocity distribution of atoms is sufficiently broad that this effective 40 Hz shift does not matter.

Pulse shaping

AOM1 and AOM2 in Fig. 3.3 shape the adiabatic passage pulses for the $F = 3$ and $F = 4$ light, respectively. The 40 MHz rf source for both AOM's is a quadrupled Loran C 10 MHz signal. The $F = 3$ and $F = 4$ patterns from the PCIP-AWFG/2 board control the level of rf power driving these AOM's via Mini-Circuits TFAS-2 variable attenuators. A second-order Bessel filter with 75 kHz cut-off frequency attenuates step transients on each PCIP-AWFG/2 analog output. We calibrated the variable attenuators and AOM's by programming the computer to apply a ramp to the variable attenuator control input for each AOM. The computer recorded the resulting intensity of diffracted light. Then it inverted the response curve to determine the waveform amplitude level required to produce a certain fractional intensity level. In this way, it constructed a 1000-interval linearization table for each adiabatic passage

beam. Using this table, the computer can create pulses with any shape that the user defines. Consequently, we can quite easily vary the pulse shapes in order to optimize the adiabaticity of the pulses, as will be described in Sec. 3.5.

The 3+4 pattern controls a digital rf switch in series with each variable attenuator. We initially intended to use this pattern as a means to simultaneously turn off the $F = 3$ and $F = 4$ light between beam-splitter pulses. We found, however, that turning the beams off with the digital rf switches instead of the variable attenuators degraded the interferometer fringe contrast. Perhaps a sufficiently large difference exists between the response times or threshold levels of the two rf switches that the beams do not actually turn off together with the digital switches. Also, rapid intensity changes can cause problems for the adiabatic passage beam phaselock, which could hurt the fringe contrast. We still use these switches to provide additional isolation for the adiabatic passage beams, but now we turn them on slightly before the variable controls, and off slightly after the variable controls.

Adiabatic passage beam phaselock

The DDS-1EB board output is the reference signal for the adiabatic passage two-photon detuning. The synthesizer output is a frequency shift keying (FSK) pattern, which is a constant amplitude sinusoidal signal that periodically changes frequencies in a phase-continuous manner. The computer sets the frequency for each interferometer pulse to compensate for Doppler-shifts from gravitational acceleration and from photon recoils, using in the calculation the average atomic velocity at the center time of each pulse. The synthesizer board reads the digital frequency control inputs at the falling edges of the STROBE input. The rising edges of the STROBE signal trigger the AT-DIO-32F board to initiate a DMA transfer of the next 32-bit frequency setting. The STROBE signal remains low for about 6 μs . The frequency changes occur about 10 μs after complete transfer pulses and midway between beam-splitter pairs, so the digital lines have plenty of time to settle during the typical $> 500 \mu\text{s}$ times between pulses. An advantage of the frequency control arrangement described here is that it requires the storage and transfer of only one frequency setting per interferometer pulse, regardless of the amount of time spent at that frequency. Most FSK

generators have equally spaced points, thereby requiring a large number of points between beam-splitter pulses when the spacing between transfer pulses is $\ll T$.

We measure the actual two-photon detuning with an optical heterodyne beatnote between the $F = 3$ and $F = 4$ light. After the shaping AOM's (AOM1 and AOM2 in Fig. 3.3), the $F = 3$ light is *s*-polarized, while the $F = 4$ light is *p*-polarized. A calcite polarizer (PBS2) overlaps both the zero- and first-order outputs of these AOM's. Since the shaped first-order outputs are sometimes turned completely off, we determine the detuning from the ≈ 9293 MHz beatnote between the zero-orders, which is precisely 80 MHz lower than the beatnote between the two first-order outputs. The zero- and first-order beams propagate at different angles, and are slightly displaced spatially, so vibrational noise on the polarizer causes slightly different Doppler-shifts for the two pairs of beams. This is probably the dominant source of error in this indirect detuning measurement, but since the differences are small, the added noise is negligible.

A high-speed photodiode (PD1) detects the optical heterodyne beatnote between the $F = 3$ and $F = 4$ light. For this purpose, we found that we could not use the same custom HP photodiodes previously used for a similar beatnote using the cesium D_2 line [15]. The response of those photodiodes dropped rapidly as we tuned the Ti:Sapphire from 852 nm to 895 nm. HP supplied us with another high-speed photodiode designed for use at 1100 nm. This photodiode had about a 20 dB higher response at 895 nm for the same optical power.

Figure 3.3 includes a functional diagram of the microwave and rf signal processing for the adiabatic passage beam phaselock. Because the precise components are of importance in considering the systematic errors from electronic phase shifts (see Sec. 4.2.8), Fig. 3.4 provides more complete device information. The ≈ 9293 MHz photodiode signal is amplified and mixed against a 9280 MHz microwave reference signal. The microwave reference is a dual-loop phaselocked DRO (dielectric resonator oscillator). This unit first phaselocks a 160 MHz crystal oscillator to a 10 MHz external reference, which we supply with a Loran C 10 MHz output. A comb generator creates numerous harmonics of the 160 MHz crystal output. Finally, a phaselocked loop locks the DRO output frequency to the 9280 MHz harmonic. The dual-loop

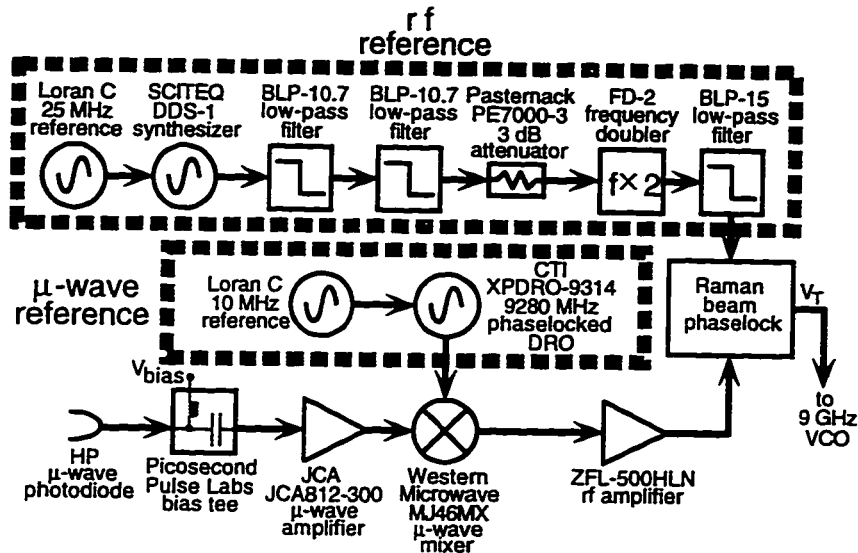


Figure 3.4: Electronics for the adiabatic passage beam phaselock. A microwave reference signal mixes down the heterodyne beatnote between the two Raman frequency components. The phaselock stabilizes the mixed down beatnote relative to an rf reference signal. For each interferometer pulse, the rf reference frequency changes to compensate for Doppler and recoil shifts. (Components are Mini-Circuits parts unless another manufacturer is indicated.)

design is good for use with the SRS Loran C Receiver because the Loran C updates cause considerable phase noise spikes. Multiplying these spikes directly from 10 MHz to 9280 MHz yields peak phase deviations of nearly π radians. Fortunately, with the dual-loop design, the bandwidth of the 160 MHz crystal lock is only about 100 Hz, which effectively damps the high-frequency phase noise spikes. The ≈ 13 MHz mixer output serves as one input to the adiabatic passage beam phaselock. The other input of the phaselock is the FSK output from the DDS-1EB board. (A passive doubler increases the tuning range of the synthesizer, without degrading the phase noise to an unacceptable level). The phaselock tunes the 9 GHz VCO driving the resonant 9.2 GHz EOM to lock the Raman beam beatnote relative to the FSK reference signal. We set the feedback gains for the lock while the FSK signal was rapidly switching between its frequency extremes. The settling time is under $50 \mu\text{s}$, which is sufficiently fast for our needs.

It would certainly be simpler to directly phaselock the 9 GHz VCO relative to the microwave reference, but we would lose two benefits of the more complicated arrangement described above. First, that approach would fail to account for any vibrations on the optics that are not common to the $F = 3$ and $F = 4$ light. We have never tried to run the atom interferometer without correcting for those vibrations, so we do not know for certain how much phase noise those particular optics would add. Based on the rapid degradation of fringes that we have observed with all but one optic isolated (see Sec. 3.5.2), the results would probably be unacceptable. A second advantage of using the optical heterodyne beatnote for the phaselock is that it removes any phase delays caused by the high-power microwave amplifier and, more importantly, from the resonant cavity EOM and the Fabry-Perot cavity. Since these are very narrow-band devices, they might quite conceivably add significant phase shifts to the $F = 3$ light as it is tuned ± 2 MHz around resonance to compensate for Doppler shifts and photon recoils. If we did not measure or correct those phase shifts, they would cause a significant error of the recoil shift measurement. One of the few disadvantages of this phaselock arrangement is that we must avoid drastic changes of the zero-order intensity levels of the shaping AOM's because sudden transients adversely affect the phaselock. This requires us to attenuate the rf power driving these AOM's to yield only about 40% diffraction efficiency. Since we would like to have a little more optical power for the adiabatic passage beams, this power loss is unfortunate.

Beam switching

The constructive addition of photon recoils from a sequence of adiabatic transfer pulses requires that k_{eff} be reversed after each pulse. We would like to apply the pulses less than 1 ms apart. This limits our options for switching k_{eff} since it would be difficult to get mechanical switches to work that fast. We could perhaps use shutters to alternately block beams, but that would waste laser power and add undesired vibrational noise to the optical table in the middle of the interferometers.

Our solution for rapidly switching k_{eff} is the arrangement of four AOM's (AOM3–AOM6) in Fig. 3.3. These AOM's interchange the alignment of the $F = 3$ and $F = 4$

light between two optical fibers with a switching time of under $10\ \mu\text{s}$. This is shorter than the Raman phaselock settling time, so it is certainly fast enough. Immediately before this optical switch, a calcite polarizer (PBS3) separates the $F = 3$ and $F = 4$ light, which had been overlapped for the beatnote measurement. We carefully set the orientation of this polarizer relative to the previous polarizer PBS2 to achieve less than 6 ppm mixing of the two beam intensities. The digital $\mathbf{k}_{\text{eff}} \uparrow$ and $\mathbf{k}_{\text{eff}} \downarrow$ outputs of the PCIP-AWFG/2 board control the rf power driving the switching AOM's via a triple layer of digital rf switches. If $\mathbf{k}_{\text{eff}} \uparrow$ is active, then AOM5 and AOM6 are on, so that the lower Raman beam is $F = 3$ light, and the upper beam is $F = 4$ light, corresponding to \mathbf{k}_{eff} directed upward. If $\mathbf{k}_{\text{eff}} \downarrow$ is active, then AOM3 and AOM4 are on, which reverses \mathbf{k}_{eff} . An 80 MHz signal (multiplied up from Loran C 10 MHz) drives the two AOM's (AOM4 and AOM6) that diffract the $F = 3$ light. An ≈ 100 MHz VCO drives the two $F = 4$ AOM's (AOM3 and AOM5). The actual frequency of the VCO varies slightly around 100 MHz to cancel phase noise in the two-photon detuning originating in the optical fibers or in the remaining adiabatic passage beam optics. A phaselock controls the VCO frequency using information obtained from the tracer beam, which I will describe in Sec. 3.3.3. Finally, note that the physical arrangement of the AOM's shown in Fig. 3.3 gives nearly equal path lengths for all optical paths to the fibers, which allows consistent mode-matching into the optical fibers for both states of the optical switch.

Final Raman beam preparation

Accuracy in the photon recoil measurement requires precisely overlapped Raman beams with excellent wave-front quality, as I will describe more quantitatively in Secs. 4.2.6 and 4.2.7. After transmission and/or diffraction by three sets of AOM's, the optical beam quality is quite poor. We spatially filter the beam modes by focusing them into two single-mode, polarization-preserving optical fibers. Several small loops of fiber near the input of the $\approx 1\text{-m}$ fibers help to strip the cladding modes. The fibers also serve the very useful purpose of insulating the final Raman beam alignment through the chamber from alignment changes before the fibers. As the

room temperature drifts during a day of running the experiment, the output alignment of the Ti:Sapphire laser changes slightly. Also, thermal lensing in the EOM and AOM crystals can significantly deflect the beams. If the direct outputs drove the Raman transitions, then these change of angle would change the amount of momentum transferred to the atoms. A $\lambda/2$ plate on the input of each fiber rotates the light polarization to match the fiber axis.

On the output of each fiber, a $10\times$, 0.25 NA microscope objective reduces the rapid angular divergence of each beam, and mildly refocuses it. After focusing, each beam gradually expands until a 2-m focal length lens collimates it with about a 2-cm diameter. We set the collimation to better than $12\ \mu\text{rad}$ using optical sheering interferometry. The beam quality is better than $\lambda/10$ within the 1-cm diameter central region of the beam. The precision we desire from the photon recoil measurement actually requires measurement of much smaller phase shifts than this, so we rely on cancellation of wave-front phase errors as I will describe in Sec. 4.2.7.

One beam enters the vacuum chamber from above and one from below. The polarizing beam-splitter cubes and $\lambda/4$ plates in Fig. 3.1 cause the beams to have σ^+ - σ^+ polarization. A $\lambda/2$ plate on the output of each fiber rotates the beam polarization. We adjust the angles of the $\lambda/2$ plates to minimize the Raman beam power deflected by the beam splitter cubes adjacent to the vacuum chamber.

The presence of a magnetic bias field splits the degeneracy between the magnetic sublevels of the ground states. This introduces a number of very closely detuned additional levels that could possibly degrade the performance of the adiabatic passage. We carefully set the polarizations of the beams to suppress the effects of these additional levels. As long as the beams have pure σ^+ polarization, the other magnetic sublevels should not be a problem. We set the lower $\lambda/4$ plate by temporarily retroreflecting the upward-propagating Raman beam and minimizing the transmission of the retroreflection through the lower polarizing beam splitting cube. Then we remove the retroreflection mirror and set the upper $\lambda/4$ plate by minimizing the transmission of the upward-propagating beam through the upper beam splitting cube. In this way we measure polarization purities of about 1.5×10^{-3} for both beams. Unfortunately, this procedure assumes that \mathbf{k}_{eff} is aligned with \mathbf{B} within the solenoid. If this alignment

is off, then the actual polarizations seen by the atoms relative to their quantization axis could be much worse. Consequently, it would be preferable to replace this purely optical method of setting polarizations with a technique using atoms.

3.3.3 Vibration isolation

Atom interferometer measurements are relative measurements in the sense that they measure the motion of atoms with respect to the spatial phase of the driving light field. Observation of interference, and particularly, accurate measurement of the phase of the interference, requires that the phase of this field be stable relative to the freely falling frame of the atoms in vacuum. Vibrations in the laboratory do not affect the motion of the falling atoms, but vibrations of the Raman beam mirrors can perturb the phase of the light field in the interaction region.

The adiabatic passage beams reflect from a total of over 20 mirrors that are not common to the two beams, so that the vibrations do not cancel common-mode in the Raman detuning. Even worse, each beam passes through a separate optical fiber with poorly correlated acoustic and thermal noise contributions [68]. Rather than trying to eliminate all of these possible noise sources, we instead overlap with the Raman beams a tracer laser which detects any noise in the laser phase from the fibers or mirrors, and then adjusts the frequency of the switching AOM's for the $F = 4$ light (AOM3 and AOM5) to reduce the noise amplitude. The purpose of this section is to first describe the tracer laser that we use to measure the laser phase noise, and then to describe the active vibration isolation system that creates the quiet reference frame in which we make the phase noise measurement.

Tracer laser

Conceptually, the simplest approach for phase-noise correction would be to directly measure the beatnote of the Raman beams immediately before the chamber. Unfortunately, we pulse the Raman beams on and off with rapid transitions for adiabatic passage. If the measurement utilized these beams, then the phase correction would be completely unreliable at the fast transitions of beam-splitter pulses, which would

be devastating for atom interferometry. Consequently, we instead overlap with the Raman beams off-resonant tracer beams that can be turned on before each pulse and off after each pulse, allowing the phase-noise correction to remain stable throughout the entire pulse.

A beam splitter (BS2) with a 20% reflection coefficient overlaps the tracer beam with the Raman beams immediately after the measurement of the optical heterodyne beatnote, as shown in Fig. 3.3. The tracer laser beam is linearly polarized at 45°, so when the calcite polarizer PBS3 splits apart the Raman beams, roughly equal fractions of the tracer beam copropagate with the $F = 3$ light and the $F = 4$ light. The switching AOM's shift the tracer light overlapped with the $F = 3$ beam down 80 MHz, and the light overlapped with the $F = 4$ beam up about 100 MHz. Above the vacuum chamber, an optical interferometer (Fig. 3.5) centered around the upper beam-splitter cube of Fig. 3.1 overlaps parts of the upward- and downward-propagating tracer beams on a photodiode. (Note that if the downward-propagating tracer beam were polarized identically with the Raman beam, then the polarizing beam splitting cube above the chamber would deflect very little power from that beam. Consequently, a multiple-order quartz waveplate immediately before the optical fiber in Fig. 3.3 rotates the polarization of the tracer light with respect to the 895 nm Raman beam light. This causes about 50% of the tracer beam to be deflected by the beam splitting cube, while only losing 5% of the Raman beam light.) A 2-nm bandwidth interference filter in front of the photodiode blocks most of the Raman beam light, allowing only the tracer light to strike the photodiode.

Because of the frequency shifts from the beam switching AOM's, the beatnote between the two beams should nominally be at 180 MHz. Any deviation of the beatnote from 180 MHz is an indication of either a frequency drift of the VCO driving the $F = 4$ switching AOM's, or noise from the fibers and mirrors. A phaselock adjusts the VCO frequency around 100 MHz to fix the phase of the beatnote with respect to a fixed 180 MHz reference derived from Loran C. The phaselock has a roughly 100 kHz bandwidth. This would probably be excessive for the laboratory noise bandwidth if we were not reversing k_{eff} between pulses. Switching k_{eff} causes a discontinuity of the phase, so it is useful to have a fast settling time for the lock.

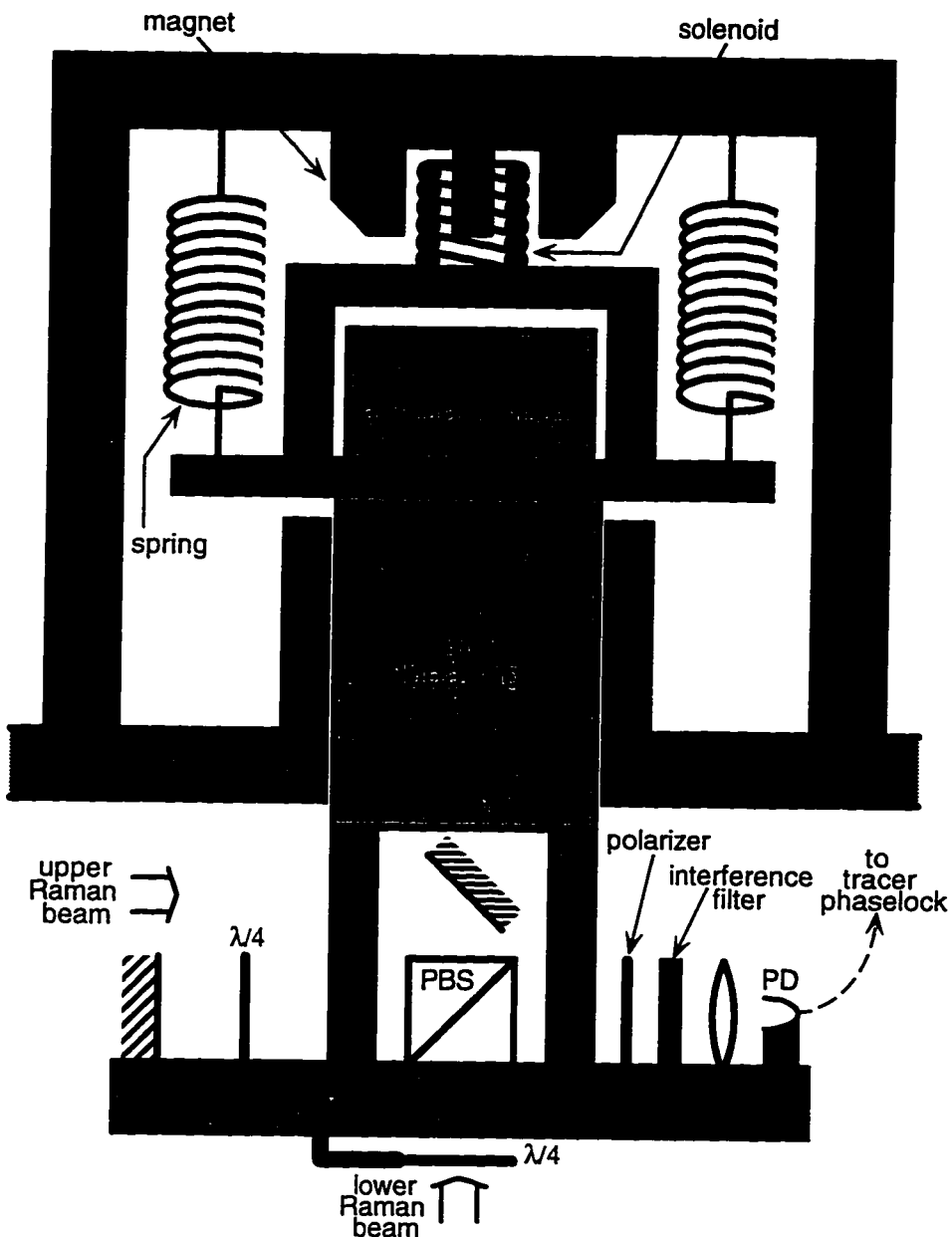


Figure 3.5: An active vibration isolation system. The optical interferometer at the bottom of the figure measures the tracer beam beatnote. The interferometer platform is actively isolated from vibrational noise. An accelerometer measures the vibrations of the reference platform. Feedback electronics (not shown) drive the solenoid to reduce the amplitude of the vibrations. The air bearing allows the platform to be translated nearly frictionlessly in the vertical direction. The springs support the weight of the system, as well as providing additional high-frequency isolation.

The wavelength of the tracer light is an important consideration. Our method of switching k_{eff} shown in Fig. 3.3 does not allow the tracer wavelength to differ grossly from the Raman beam wavelength since the angular deflection of AOM's depends on the optical wavelength. In fact, even with our present choice of 887 nm for the tracer wavelength, the angular misalignment from the AOM diffraction causes about a 30% loss of power through the fibers. Not many choices exist for diodes lasers near 895 nm. The tracer laser is an EG&G C86135E diode laser that required custom modifications for single-mode operation. The nominal frequency of this diode is 905 nm. We ordered several diodes without the standard anti-reflection (AR) coating. New Focus applied a higher quality ($R < 0.1\%$) AR coating to the diodes. We run the diode single-mode using standard external grating feedback [54].

Two sources of error in this phase noise correction include drifts of the absolute frequency of the tracer laser, and the wavelength difference between the tracer laser and the Raman beams. We stabilize the laser diode temperature, but do not presently stabilize the absolute frequency of the diode. The lengths of the optical fibers compensate to within ≈ 10 cm for the difference of the paths lengths for the $F = 3$ and $F = 4$ light up to the location of the atom-light interactions. Consequently, drifts in the absolute frequency of the tracer light should cause only very small shifts of the beatnote phase. Furthermore, in the recoil measurement, we only care about the absolute phase during the time $T \sim 100$ ms between beam-splitter pulses. If this frequency drift eventually becomes a problem, we can stabilize the laser to an atomic or molecular transition. The wavelength difference between the Raman and tracer beams is problematic because our vibration correction uses Doppler-shift measurements. The actual Doppler shift of the 895 nm light is ($887/895 \approx 99.1\%$) of the Doppler shift that we observe on the 887 nm light. Consequently, we actually overcorrect for noise by 0.9%. If this difference eventually becomes the main contribution to phase noise, a DDS synthesizer could scale the beatnote measurement in real-time [69]. The optical heterodyne beatnote would serve as the external reference for the synthesizer, and we could set the synthesizer output frequency to achieve the proper phase-scaling factor.

Actively isolated optical interferometer

Correct measurement of the phase noise from the fibers and mirrors requires that the optical interferometer detecting the tracer beam beatnote must itself have no vibrations along the direction of \mathbf{k}_{eff} . We need to isolate against vibrations down into the mHz regime. Passive isolation at such low frequencies using a mechanical system with a resonant frequency $\omega = \sqrt{k/m}$, where k is the spring constant and m is the mirror mass, would require either an extremely weak spring constant or a large mass. A weak spring is feasible for horizontal isolation, but requires unreasonably large spring extensions when the isolated system is supported against gravity. We avoid this problem by actively isolating the optical interferometer platform [70], as shown in Fig. 3.5. Springs support the interferometer platform and provide high-frequency vibration isolation. The air bearing constrains the platform to nearly frictionless motion in the vertical direction. The accelerometer measures vibrations of the platform. A computer digitally processes the accelerometer signal to derive a control signal for the solenoid at the top of the system.

The reduction of the accelerometer error signal with the feedback loop closed is one indicator of the performance of the vibration isolation system. The error signal indicates that the active isolation decreases the vibrations by a factor of up to 200 in the frequency range from 0.01 to 100 Hz. To actually achieve this level of isolation along \mathbf{k}_{eff} requires a roughly 1 mrad alignment of the sensor axis to \mathbf{k}_{eff} , and a similarly good alignment of the atomic trajectory below the sensor to avoid problems due to tilt [70]. A more directly applicable test for the vibration isolation is its benefit for atom interferometers, which I will discuss in Sec. 3.5.2.

3.4 State-selective detection

At the end of an atom interferometer pulse sequence, the signal atoms are either in $F = 3, m_F = 0$ or in $F = 4, m_F = 0$. Most of the background atoms have been optically pumped into $F = 3, m_F = +3$ or $F = 4, m_F = +3$ or $+4$. Since a fair amount of amplitude noise is present in the number of launched atoms, we need to reduce the

number of background atoms detected as much as possible. Consequently, we desire a detection process that detects only atoms in the $m_F = 0$ sublevel. The magnetic bias field inside the solenoid breaks the degeneracy of the magnetic sublevels. We can therefore drive transitions for only signal atoms using either microwave pulses or Doppler-free stimulated Raman transitions. The eventual goal for efficient detection of cesium atoms is to get all of the signal atoms into the $F = 4$ state. Then the $6S_{1/2}$, $F = 4 \leftrightarrow 6P_{3/2}$, $F' = 5$ cycling transition yields a high scattering rate for photons, with very little loss of atom from optical pumping into the $F = 3$ state.

3.4.1 Doppler-free Raman transitions

In early work on this version of the photon recoil measurement we drove microwave transitions using a microwave horn. The one difficulty was establishing a reasonably uniform level of microwave radiation inside the magnetic shielding (see Fig. 3.1). The holes at the end of the shielding are only about 5 cm in diameter and the microwave horn can not face directly toward the hole without blocking the Raman beams. Since the field was quite nonuniform, the π pulse duration had to be set for the particular location in space that the microwave field interacted with the atoms. Consequently, whenever photon recoils alter the atomic trajectory, the time of the microwave pulse must be adjusted to keep the spatial location of the interaction fixed. Even when we did that, we still observed variable transfer efficiency. Later we discovered that this problem was caused by line noise on the Loran C receiver that was shifting the microwave reference frequency away from the cesium transition. Since then, we have modified the Loran C receiver to reduce the phase noise at 60 Hz harmonics by over 20 dB. Consequently, microwave transitions may yet be a viable approach.

After the inconsistent behavior we observed with microwave transitions, we began using Doppler-free Raman transitions. The advantage of this method is that we could use the polarizing beam-splitting cube at the bottom of the chamber to overlap the Doppler-free Raman beams with the upward-propagating adiabatic passage beam. Consequently, the field irradiates the atoms throughout the entire trajectory, yielding great flexibility for the application of pulses. Also, the beam axis corresponds with

the magnetic field direction, so the polarizations are well defined.

A single Spectra Diode Labs SDL-5411-G1 laser diode with external cavity stabilization is the source for both Doppler-free Raman beam frequencies. Direct modulation of the diode laser current at about 4.6 GHz creates first-order sidebands spaced by the cesium ground-state hyperfine splitting. We set the free spectral range of the external cavity to 2.3 GHz, a subharmonic of the modulation frequency. This enhances the modulation depth [64] by a factor of about 4.4. For a total laser output of 33 mW, a microwave drive power of only 60 mW yields maximum power in the first-order sidebands. A bias tee combines the DC and microwave currents for the diode. We lock the carrier frequency of the diode laser 3.5 GHz above a reference beam from the SEO Ti:Sapphire laser. This fixes the one-photon detuning of both beams at about 1 GHz below their respective transitions. We set the laser intensity to give π pulse times of about 4 ms. The transfer efficiency for a π pulse is about 80%. Poor uniformity of the beam intensity over the relatively large atom cloud is probably the reason for this poor efficiency. Since we never apply more than two of these pulses, this efficiency is acceptable.

3.4.2 Atom detection

As shown in Fig. 3.1, two additional detection laser beams, the probe beam and the clearing beam, copropagate with the Doppler-free Raman beam into the vacuum chamber. Both beams are on-resonance with the $6S_{1/2}$, $F = 4 \leftrightarrow 6P_{3/2}$, $F' = 5$ transition. The 1.25-cm diameter probe beam has an intensity of $1.6 \text{ mW/cm}^2 \approx 1.5I_{\text{sat}}$. We use this beam to scatter light from the signal atoms. The clearing beam is about 2.5 cm in diameter with a comparable intensity. We use this beam to blast away all atoms in the $F = 4$ state. Since the clearing beam is larger than the probe beam, it eliminates all atoms that could scatter probe photons. The only reason for choosing the probe intensity fairly low is that the PMT detects some background scatter of probe light from the AR-coated vacuum can windows. At present, we do not intensity stabilize the probe beam, so eventually the scatter can increase the noise on the signal. This problem only becomes significant after a large number of transfer

pulses has decimated the normally much larger atom signal.

We regularly use two possible detection pulses sequences, depending on the exit state of the signal atoms from the atom interferometer. We can select the shape of the final beam-splitter pulse to leave the signal atoms either in $F = 3, m_F = 0$ or in $F = 4, m_F = 0$. Normally we choose the $F = 3$ state. In that case, the detection sequence consists of a 16-ms clearing pulse to remove all $F = 4$ atoms, a Doppler-free Raman π pulse to transfer the signal atoms to the $F = 4, m_F = 0$ state, and a 5-ms probe pulse. If instead the interferometer leaves the atoms off in the $F = 4$ state, then a Doppler-free Raman π pulse first transfers the signal atoms to $F = 3, m_F = 0$, and then the detection process continues again as before. Alternating between the two possible exit states can test for systematic errors caused by phase shifts from beam-splitter pulses.

A Hamamatsu R943-02 PMT detects the scattered light from the probe beam. Two long-pass filters in front of the input aperture reduce the sensitivity to room lights. The PMT output is amplified and distributed to various scopes and to an A/D input of a Keithley-Metabyte DAS-16 board in the computer. The probe trigger signals the A/D board to sample the input at a rate of 50 kHz for 4 ms. The computer then numerically integrates the probe signal and stores the result for that experiment cycle. The launch and measurement cycles occur at a rate of about 1.1 Hz.

In this generation of the photon recoil measurement, we achieved some improvement in the noise level of the probe signal. The typical level of amplitude noise previously for the probe signal after a launch was about 5%(rms) [13]. Now we have improved that to about 1.5%(rms), mostly through shielding of the laser beams from air-conditioner air currents and improved frequency stability of the probe beam. Two Doppler-free Raman π pulses add in quadrature another about 2%(rms) amplitude noise. This is the reason that we usually choose to apply only one Doppler-free π pulse. This amplitude noise limits the signal-to-noise of interferometer fringes for interferometers with very low N and T , so it hinders the rate at which we can check for some systematic errors. With the most sensitive interferometers, however, other noise sources dominate. Section 5.1.3 will cover possible avenues for further improvements in the signal-to-noise ratio of the fringes.

3.5 Tests of adiabatic passage

Two main operating modes exist for the computer program AltInt4X.BAS that generates the adiabatic pulse sequences and collects the signal data. First, it can create a sequence of N complete transfer pulses. We use this mode to measure the efficiency of adiabatic transfers. Secondly, it can program modified Ramsey-Bordé interferometer sequences with an arbitrary number N of transfer pulses between the beam-splitter pairs. For both modes, the pulse sequence can be preceded by an arbitrary number of lower intensity, longer pulses to preselect a narrow slice of the initial velocity distribution of atoms. The purpose of this section is to describe tests that we have performed to gauge the performance of the adiabatic passage itself, without regard for the particular value it provides for the photon recoil measurement. Tests specifically relating to the recoil measurement will be covered in Chapter 4.

3.5.1 Momentum transfer

A typical measurement of adiabatic transfer efficiency consists of one long-duration, low-intensity transfer pulse followed by an arbitrary number of maximum intensity, shorter transfer pulses. As we apply more transfer pulses to the atoms, the width of the atom velocity distribution becomes narrower. The transfer efficiency should initially start out low, as the transfers weed out atoms with velocities corresponding to the tails of the dark state. The differential transfer efficiency should gradually increase asymptotically to the efficiency that would be expected for an infinitely narrow velocity distribution. The purpose of the first pulse is to preselect a narrow velocity slice from the initial distribution of launched atoms. By throwing out most of the borderline atoms in a single pulse, we accelerate the process of converging to the asymptotic efficiency. Consequently, we can obtain accurate efficiency measurements with a smaller number of transfer pulses. Our numerical calculations and also experimental results suggest that the frequency width of the dark resonance has the dependence

$$\Delta\nu_D \propto \sqrt{I/\tau}, \quad (3.3)$$

where I is the peak beam intensity and τ is the pulse duration. Consequently, the long-duration, low-intensity preselection pulse should have a narrower frequency width than the normal transfer pulses, and thereby serve its planned purpose.

One limitation of this measurement is that it does not completely distinguish the coherently transferred atoms from those that undergo at least one incoherent transfer. When an atom spontaneously emits a photon from the $6P_{1/2}$, $F' = 3$, $m_F = +1$ state, it has a nonzero probability of falling back into the dark state. From the branching ratios, we can calculate the probability for such incoherent transfer. This means that the observed loss rate of atoms may need to be increased by a certain fraction to account for those atoms that were not transferred coherently, but still remain in the dark state. Note that incoherently transferred atoms receive a slightly different momentum recoil than coherently transferred atoms. Consequently, after one incoherent transfer, an atom is more likely to be left behind by future transfer pulses. Since the loss rate correction factor does not take this effect into account, it should give a worst-case estimate of the transfer efficiency. In future statements about transfer efficiencies, I will always report the calculated *coherent* transfer efficiency rather than the measured transfer efficiency, unless stated otherwise.

After every transfer pulse we reverse the direction of \mathbf{k}_{eff} . By alternating \mathbf{k}_{eff} , we cause the momentum recoil from each transfer to add constructively. This provides us with two demonstrations of momentum transfer. First, the application of each pulse provides a significant change in the time that the atoms fall back into the region imaged by the PMT. For example, a single transfer applied while the atoms are at the top of the trajectory changes the passage through the probe region by about $685 \mu\text{s}$. We have applied up to 100 transfer pulses in this manner, which corresponds to the momentum transfer from 200 optical photons. With the recoils all directed upward, this produces a very visible 68 ms delay of the descent of the atoms through the probe region. We can more precisely measure the momentum transfer by scanning the Raman detuning for the final transfer pulse. The centering of the measured velocity distribution around the calculated center frequency (assuming successful momentum transfer) gives an indication of the quality of the momentum transfer.

We chose the shape for the adiabatic passage complete transfer pulses empirically

to achieve the highest transfer efficiency. The pulse shape that we presently use looks much like Fig. 2.9(a). All transitions consist of two exponential curves that meet at about 80% of maximum intensity. This is also the intensity level at which the $F = 3$ and $F = 4$ beam intensities are equal. For typical 65 μs transfer pulses, the fast transitions occur in about 1 μs . We have experimentally tested a variety of different shapes including sinusoids, linear ramps, simple exponentials, and hyperbolic functions. Most of these shapes yield transfer efficiencies roughly 1-2% lower than the shape we now use.

Presently, the total optical power per adiabatic passage beam is about 6 mW. This gives a peak intensity of $3.8 \text{ mW/cm}^2 \approx 1.7I_{\text{sat}}$ at the centers of the 2-cm diameter Gaussian beams. The normal transfer pulses make full use of the available laser power, and are typically about 65 μs in duration. The frequency width of these pulses is about 160 kHz, as shown in Fig. 3.6. This large width relative to the ≈ 75 kHz frequency width of the atomic velocity distribution suggests that we should be able to observe good fringe contrast with very modest velocity preselection. The preselection pulse is typically 800 μs long, with 25% of normal intensity. This pulse has a dark state frequency width of about 20 kHz, so it selects about one-third of the initial velocity distribution. This is a significant improvement in the number of signal atoms over the original photon recoil measurement using stimulated Raman transitions, for which the preselection width was only $\Omega_{\text{eff}} \approx 5$ kHz. Another advantage of the dark-state resonance is the rapid decay of the distribution tails in Fig. 3.6. This arises quite naturally and does not require special pulse shapes such as for stimulated Raman transitions.

From our numerical simulations [31] reviewed in Sec. 2.2.2, the $6P_{1/2}$, $F' = 4$ excited state off-resonant absorption theoretically limits the possible coherent transfer efficiency to 98.7%. A transfer efficiency of this order should require a polarization purity of about 10^{-4} and, in the Doppler-sensitive case for a fast moving atom ($v > \Delta\omega_D/k_{\text{eff}}$) a suppression of back reflections of similar order. When we initially tested adiabatic passage with copropagating (Doppler-free) instead of counterpropagating (Doppler-sensitive) beams, we in fact obtained a coherent transfer efficiency of 98.4% per pulse [43]. For Doppler-sensitive transitions, we have achieved 93% coherent

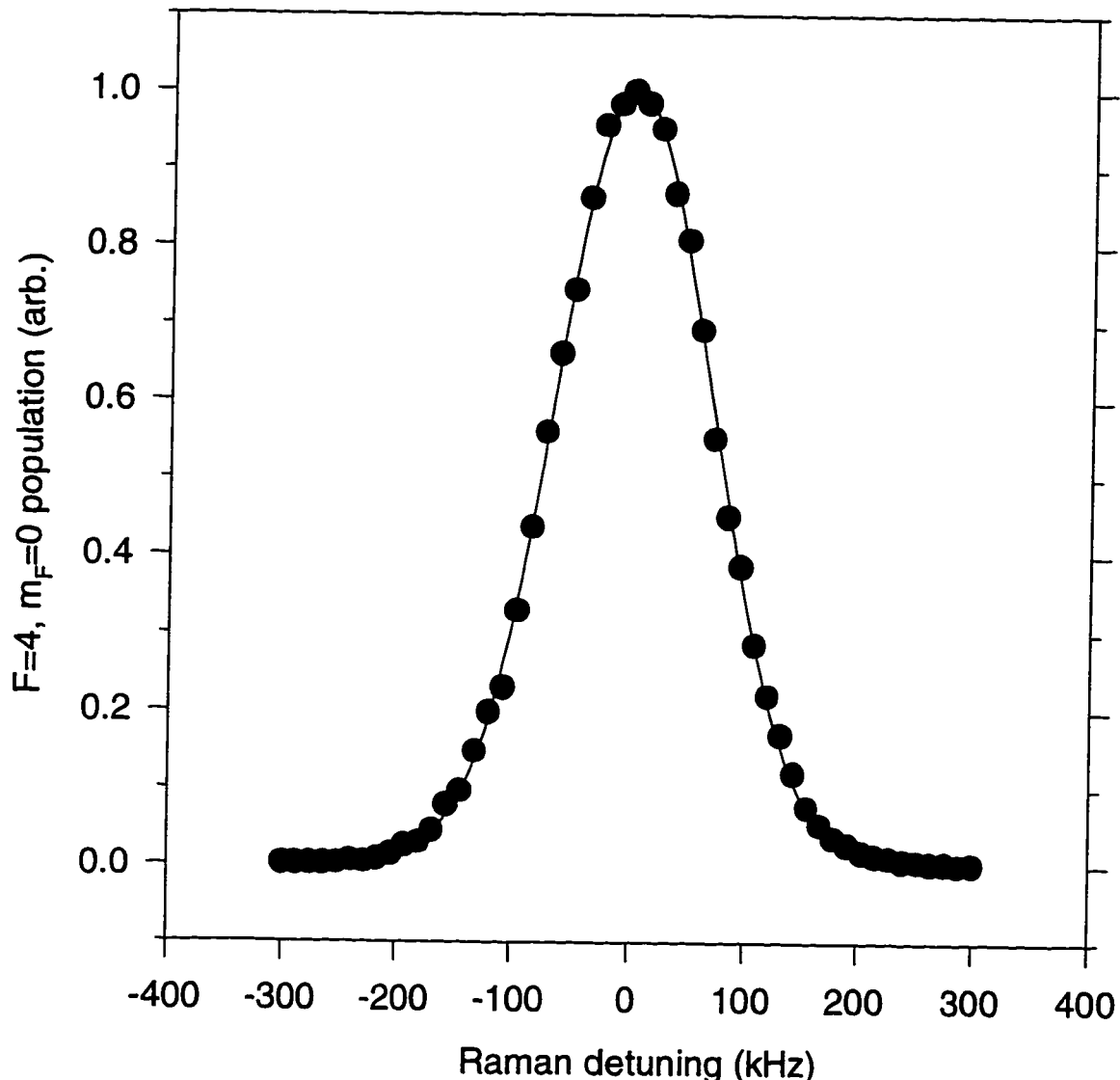


Figure 3.6: The dark state frequency width for adiabatic transfer pulses. We measure this resonance by applying a single preselection pulse to narrow the velocity distribution, followed by the normal transfer pulse. We scan the frequency of the last pulse. A typical $65 \mu\text{s}$ transfer pulse has a 160 kHz FWHM frequency width. A Gaussian lineshape fits the resonance quite well.

transfer efficiency. This represents a significant improvement over the 85% transfer efficiency we previously obtained with far-detuned Raman transitions [15]. With this higher efficiency, we can add twice as many transfer pulses for the same loss of atoms. This is also a large improvement over previous results of about 80%/ $2\hbar k$ using adiabatic transfer with the cesium D_2 line [41], but it is still short of the theoretical limit.

Several possible explanations exist for the nonideal transfer efficiency. We only have about 10^{-3} polarization purity as determined optically (see Sec. 3.3.2), and the magnetic field of the solenoid is probably misaligned from \mathbf{g} by a couple of degrees, which introduces even more polarization impurity relative to the quantization axis of the atoms. At present, we do not have a method for adjusting the solenoid angle. A 1.5×10^{-3} back reflection from the upper vacuum can window may still be a problem, even though we tilted the window about 5° so that the reflection mostly misses the atoms. Finally, the frequency chirp caused by the acceleration of the atoms during the time of the adiabatic passage pulse may also limit the transfer efficiency.

3.5.2 Interferometry

A typical interferometer pulse sequence consists of one preselection pulse followed by two beam-splitter pulses, N complete transfer pulses, and a second pair of beam-splitter pulses. The program centers on resonance the Raman detunings for all of the pulses except for the last two beam-splitter pulses. It then simultaneously scans the frequencies of these final two pulses to produce fringes in the number of detected atoms.

We chose beam-splitter shape definitions similar to the high efficiency complete transfer pulses. Again, the transitions have the form of two exponential curves, as shown in Fig. 2.9(b) and (c). The only new feature is the manner in which the beams turn on and off together. In this case, we optimized the shape parameters to achieve the highest fringe contrast. We typically use $250 \mu\text{s}$ beam-splitter pulses. The beam intensities are equal at about the 50% intensity level. These pulses need to be longer than the complete transfer pulses to minimize ac Stark shifts from nonadiabaticity,

as will be described in Sec. 4.2.3. The longer length of these beam-splitter pulses is the main reason that velocity preselection improves the fringe contrast.

We experimentally demonstrated the first atom interferometers that use adiabatic passage to transfer momentum [43]. That first demonstration obtained fringes for $T = 250 \mu\text{s}$ with a contrast of 29% using the $6P_{1/2}$, $F' = 3$ excited state, and 17% contrast using $F' = 4$. The maximum theoretical fringe contrast is 50% with matrix elements of zero for spontaneous decay back to the dark state. Correcting for the actual matrix elements for cesium gives theoretical limits of 33% for $F' = 3$ and 23% for $F' = 4$. After that initial demonstration, we have always used the $F' = 3$ excited state since the matrix elements are more favorable for high-contrast fringes.

Adiabatic passage interferometers provide a practical test for the performance of the active vibration isolation system. In the recoil measurement, we record a series of several fringes, and then fit a sinusoid to the fringes to determine the location of a fringe center. Consequently, the uncertainty of the fitted phase $\Delta\phi$ of the sinusoid is a good measure of the signal-to-noise of the fringe as it relates to the recoil measurement. In Fig. 3.7(a) we plot the fitted phase uncertainty for sets of fringes taken for a range of beam-splitter separations T . As T increases, the interferometer becomes sensitive to phase noise and vibrations at increasingly lower frequencies. The value of this plot is that it shows how much the measurement sensitivity could be increased by further reduction of the phase noise. Typical interferometers with $N \sim 30$ can use times up to about $T \approx 120 \text{ ms}$ with our present spatial limitations. Consequently, the potential exists for a factor of about 1.5 increase of signal-to-noise from reduction of phase noise. The residual fringe degradation seen here most likely results from either limitations of the active vibration isolation system or air currents. To demonstrate the present growth in the measurement precision with T , we plot the uncertainty of the fringe center frequency $\Delta f_c = \Delta\phi/2\pi T$ in Fig. 3.7(b). This shows an initial rapid improvement of the precision with T which levels off between 100 ms and 200 ms because the phase noise increases at roughly the same rate as the interferometer sensitivity.

Of similar practical interest is the enhancement in measurement precision for atom interferometers as we add transfer pulses. Figure 3.8(a) shows that a potential

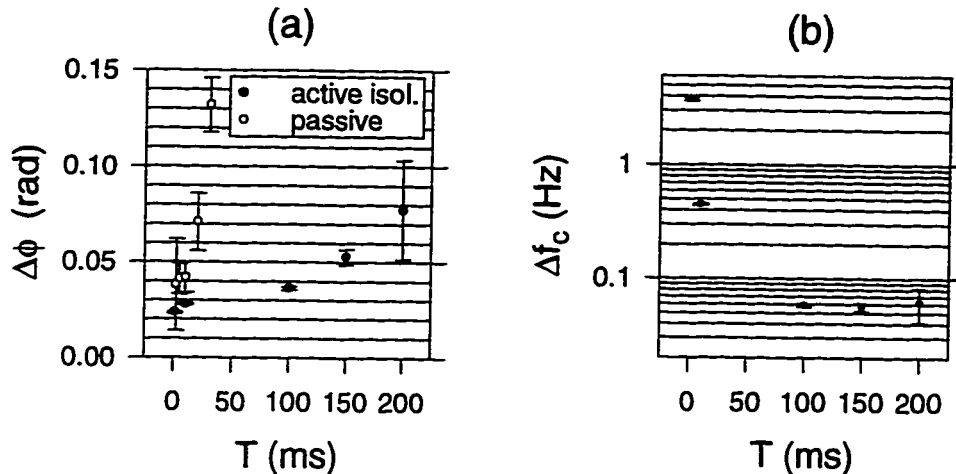


Figure 3.7: Vibration isolation performance for atom interferometry. (a) The fitted phase uncertainty $\Delta\phi$ for 45 s of data collected with $N = 0$ and a range of beam-splitter separation times T is shown for both with and without the active vibration isolation. (b) The corresponding uncertainty in the fringe center frequency $\Delta f_c = \Delta\phi/2\pi T$ has a broad minimum between 100 ms and 150 ms. The error bars for $T = 150$ ms and $T = 200$ ms are larger because we have collected little data for those conditions.

fourfold resolution improvement exists for $T = 120$ ms and $N = 50$ if we could reduce the degradation with N , which is mostly caused by amplitude noise of the adiabatic passage beams. In this situation, the possible $1.3\times$ improvement from reduced phase noise is relatively less impressive. Between Figs. 3.7(b) and 3.8(b), we see that with our present noise sources, the most sensitive interferometers have $T \approx 120$ ms and $N \approx 30$.

These atom interferometers convincingly demonstrate that the adiabatic passage complete transfer pulses truly provide coherent momentum transfer. For the fringes included in Fig. 3.8, we calculated the total number of atoms contributing to the sinusoidal interference signal for each value of N . The rate of decrease of signal atoms with N corresponds to a coherent transfer efficiency 91.5%. Interestingly, the transfer efficiency measured by our standard technique gave the same result, even before correcting for atoms falling back into the dark state. Perhaps with sufficiently large N , most of the atoms are eventually lost and this correction becomes unnecessary.

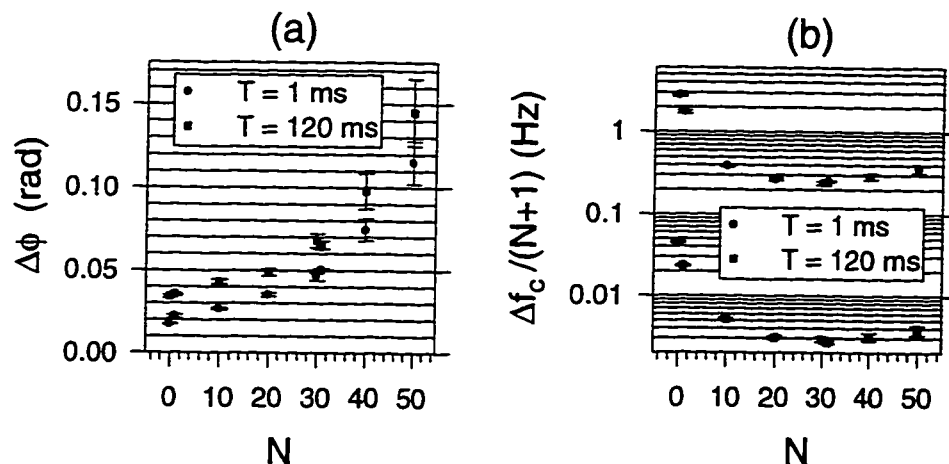


Figure 3.8: Enhancement of the interferometer sensitivity with N . We plot (a) the fitted phase uncertainty $\Delta\phi$ and (b) the corresponding interferometer sensitivity for 45 s of data collected with $T = 1 \text{ ms}$ and $T = 120 \text{ ms}$ for various numbers of transfer pulses. In each case, we divide the uncertainty in the fitted fringe phase by $N + 1$. This ratio is an indicator of the interferometer precision. As long as it decreases with N , the measurement precision improves.

Chapter 4

Results

In this chapter, I will first discuss the process of obtaining a recoil shift value from the measured atom interferometer fringes. Next I will describe the numerous tests for systematic errors that we have made and the limits they place on the accuracy of this measurement. I then will present our measured value for the photon recoil shift using the cesium D_1 line. Using the best measurements of mass ratios and the absolute frequency of the D_1 line, I will calculate from this measured photon recoil shift a value for the fine-structure constant.

4.1 Recoil frequency shift

4.1.1 Data analysis

Experimentally, we observe a nearly sinusoidal variation of the number of atoms detected in one of the cesium hyperfine ground state levels as we vary the Raman detuning of the last two beam-splitter pulses, while holding the frequencies of all other interferometer pulses centered on resonance. Actually, the dark-state frequency width for the beam-splitter pulses serves as an envelope for the interference fringes, so the dependence is not perfectly sinusoidal. For typical experimental parameters, the fringe spacing is about 8 Hz, while the frequency width of the beam-splitter pulses is about 90 kHz. We normally only scan through about 5 fringes near the center of the

envelope, which is only about 0.04% of the width of the envelope. With the present signal-to-noise of our fringes, ignoring this small amplitude modulation does not hurt the quality of our fits. It also should not introduce any systematic shifts of the recoil measurement, as I will discuss in Sec. 4.2.5.

In all of our determinations of the photon recoil shift, we therefore fit the atom interferometer data to sinusoids of the form

$$y = A + B \cos [2\pi T' (f - f_c)], \quad (4.1)$$

where f is the two-photon detuning for the final two pulses, y is the measured atom signal, and A , B , T' , and f_c are the fit parameters. The fit result of greatest interest here is the location f_c of the fringe center. Once we obtain a value for f_c for both interferometers of Fig. 2.3(b), the difference $|f_c^a - f_c^b|/(N+1)$ is the photon recoil shift Δf_{rec} . The Numerical Recipes fit routine that we use also provides uncertainties for the fit parameters based on the covariance matrix. Consequently, we can estimate the uncertainty of the recoil determination by combining in quadrature the uncertainties of f_c^a and f_c^b . This estimate is useful as we collect data for gauging the “quietness” of the lasers, but the final uncertainties that we report here for the recoil frequency shift are based entirely on the statistics of repeated measurement of the recoil shift, not on the fit uncertainties.

We wish to fit for the parameters A , B , and f_c of Eq. (4.1) independently for each interferometer in a straightforward manner. The fringe spacing parameter T' is more complicated. Ideally, we would expect $T' \equiv T$, where T is the time that the light is off between beam-splitter pulses. However, in practice, the light transition times are not infinitesimal. Consequently, it seems reasonable to fit for an effective “off” time T' . Since the same electronics drive the pulses for both interferometers, T' should be identical for the two interferometers. This requires a coupled fit of both sets of fringe data to the two curves with a total of seven free parameters. When we perform this coupled fit, we generally obtain a result for T' that is within 1-2% of T . In practice, we usually perform the fit both with T' variable but coupled, and with $T' \equiv T$, and then pick the result with the best χ^2 value. After an initial fit, we compute the standard deviation σ of the fit residuals and eliminate any points

with residuals larger than 3σ . We have very few “drop-outs” in the experiment, so we generally eliminate only about 0.5% of the data in this way.

We obtain similarly close agreement of T' and T when we fit for a single interferometer. This was a very encouraging early result with adiabatic passage atom interferometers. In the first version of the photon recoil measurement with stimulated Raman transitions, we often observed around a 20% difference between T' for the two interferometers in a pair [13]. The shifts tended to be symmetric around T , so we presumed it was a fairly linear drift from ac Stark shifts or residual motion of the retroreflection mirror. With adiabatic passage, this very troubling effect disappeared. Additionally, we have observed that T' and T still agree within 1-2% even with 250 μ s beam-splitter pulses separated by $T = 250 \mu$ s. Therefore, the time that sets the fringe spacing is clearly the time that the light is off between beam-splitter pulses, *not* the separation of the pulses centers. That is the expected result, because while the light is on, the phase of the atoms remain locked to the phase of the dark state defined by the light. It is only when the light is off that the atoms freely evolve.

One remaining important issue is the $1/T'$ ambiguity of f_c in Eq. (4.1). In theory, we can remove this ambiguity by performing a series of measurements for different interferometer times T . For example, we can initially choose $T \sim 1/\Delta\omega_D$, where $\Delta\omega_D$ is the dark-state frequency width for the beam-splitter pulses. This allows easy identification of the center fringe, thereby determining a rough value of Δf_{rec} . This rough estimate subsequently removes the ambiguity as we increase T for more precise measurements. Then we can repeat the same boot-strap process to remove the ambiguity as we increase N to our highest sensitivity interferometers. In practice, we use the accepted value of Δf_{rec} to estimate the center frequency for both interferometers. In that way, when we collect data, the two sets of interferometer fringes visually appear to have identical phases. We test the assumption that this correctly removes the phase ambiguity every time that we collect data by varying T and N . If the assumption were not correct, we would obtain very inconsistent results as we vary those parameters.

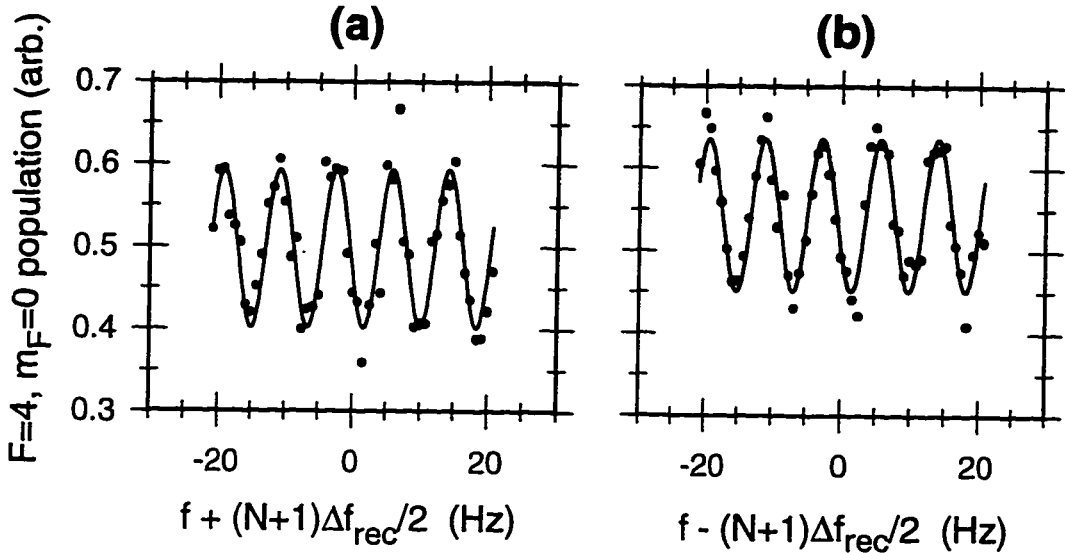


Figure 4.1: Atom interferometer fringes for $T = 120$ ms and $N = 30$. This 90 s set of data provides a 120 ppb measurement of Δf_{rec} . The least-squares fit sinusoids have $18 \pm 1\%$ contrast. The maximum theoretical contrast is 33%. (a) Lower interferometer. (b) Upper interferometer.

4.1.2 Interferometer fringes

The two sets of fringes are fit to sinusoids with periodicity $1/T$. We collect data such as this by alternating between points on the two interferometers. This helps to reduce the effects of long-term drifts of the lasers and the vibration isolation system. Also, after completing a measurement using a pair of interferometers, we create inverted interferometers by reversing the orientation of \mathbf{k}_{eff} for all of the interferometer pulses. This allows measurement and partial cancellation of errors from magnetic-field variations, wave-front distortions, and electronic phase shifts.

Figure 4.1 shows atom interferometer fringes obtained using a modified Ramsey-Bordé interferometer with beam-splitter separations of $T = 120$ ms and $N = 30$ transfer pulses. The values of N and T used here presently yield peak precision for the recoil shift measurement. The frequencies on the horizontal scale are plotted relative to resonance frequencies calculated using the accepted value for Δf_{rec} from Sec. 4.3. The difference of the phases of these two sets of fringes is then a measure of the discrepancy between $(\Delta f_{\text{rec}})_{\text{exp}}$ and $(\Delta f_{\text{rec}})_{\text{acc}}$. The measured separation between

the two center frequencies is $\Delta f_{\text{rec}}^{30} = 31 \times 30,012.5540(35)$ Hz. This is a 120 ppb measurement of Δf_{rec} from 90 s of data. In this single measurement we are already nearing the 97 ppb uncertainty of $(\Delta f_{\text{rec}})_{\text{acc}}$, which is limited mostly by the uncertainty of the absolute frequency of the cesium D_1 line. This statistical uncertainty would limit a determination of α to 60 ppb.

The fit uncertainties of f_c (see Figs. 3.7 and 3.8) indicate that we achieve the highest measurement resolution for Δf_{rec} with parameter values T and N roughly equal to those used in Fig. 4.1. We cannot increase T significantly larger than 120 ms with $N = 30$ without the atoms exiting the magnetically shielded region because of the $124\hbar k$ momentum difference between the two interferometers. The reduced 18% contrast of Fig. 4.1 accounts for a 33% decrease in the signal-to-noise (S/N) ratio. The remaining 25% degradation of S/N for $N = 30$ is caused by amplitude noise from the adiabatic passage complete transfer pulses. Further improvements in sensitivity over the results reported here will probably require addressing both issues of reduced contrast and amplitude noise.

4.2 Checks for systematic errors

The flexible form of this photon recoil measurement provides many powerful options for testing for systematic errors. In less than 15 s we can completely alter the geometry of the atom interferometer by changing the beam-splitter separation time T , the number of transfer pulses N , the orientation of \mathbf{k}_{eff} , and the positions in the trajectory where the atom-light interactions occur. Such variability would be impossible in most atom interferometry measurements with atomic beams instead of a cold atom fountain, for which each interaction requires a physically separate laser beam.

First I will discuss the limits that we can place on certain of the possible systematic errors of which we are aware, including quadratic Zeeman shifts, ac Stark shifts, laser detuning, Doppler-free Raman transitions, laser beam alignment and collimation, wave-front distortion, and electronic phase shifts. Reference [15] discusses numerous other possible systematic errors including second-order Doppler shifts, gravitational red shift, and the Sagnac effect. Since those effects all lie far below the present

measurement precision, I will not discuss them further here. Finally, I will describe more general tests such as varying N and T that may involve a number of these effects, as well as others that I have not enumerated.

4.2.1 Magnetic-field shifts

In Fig. 3.2 we showed the magnetic field experienced by atoms throughout the trajectory. If the field were perfectly uniform, then we would not have to worry about quadratic Zeeman shifts because it would simply cause an overall change of the ground state hyperfine splitting that would not affect the relative phases of the interferometers. Unfortunately, this is not the case, so we need to estimate the size of shifts that can be caused by magnetic fields. For this we use the approximation for the quadratic Zeeman shift $\delta(\Delta\nu_{\text{QZS}}) \approx 2\alpha_B B \delta B$ from Eq. (3.2). In this expression, we take $B \approx 71.8$ mG, the average bias field from Fig. 3.2. The only remaining question is what value to use for the variation δB in the magnetic-field amplitude. The fact that the atomic position is not a classical variable in this experiment complicates the precise calculation of the magnetic-field shifts. We can obtain a reasonable estimate for the size of the shift by integrating over the physical trajectories of the centers of the atomic wave packet. The quadratic Zeeman shift affects the interferometer phase whenever the two paths are in opposite states, or paths in the same internal state experience different fields because they are spatially displaced. Any field-related phase shifts from the first beam-splitter pair cancel between the upper and lower interferometers, since the trajectories overlap. The spatial displacement between the upper and lower interferometers is relatively small during the application of the transfer pulses. Consequently, the main contribution to the phase shift occurs between the final two beam-splitter pulses, as the upper and lower interferometers rapidly separate spatially. The average spatial separation of the two interferometers between these final two pulses is

$$\Delta z = (N + 1) [T + (N + 1)T_{\text{sp}}] (\hbar k_{\text{eff}} / m_{\text{Cs}}), \quad (4.2)$$

where T_{sp} is the spacing between the complete transfer pulses. For example, with typical parameters of $N = 30$, $T = 120$ ms, and $T_{\text{sp}} = 685$ μ s, the average spatial

separation is $\Delta z = 2.9$ cm. Assuming that we restrict the spatial range of the trajectory between 19 cm and 43 cm above the trap, we see from Fig. 3.2 that the average difference between magnetic fields experienced by the upper and lower interferometers must be less than about 0.3 mG. This corresponds to a maximum quadratic Zeeman shift difference of 18 mHz. This frequency shift should be compared with the net recoil shift $\Delta f_{\text{rec}}^{30} = 31\Delta f_{\text{rec}} \approx 930$ kHz, so it represents a 20 ppb change of Δf_{rec} .

If this were the ultimate accuracy limit from quadratic Zeeman shifts, it would be unacceptable; we would either need to make the field more uniform or decrease the bias field. Fortunately, there exists a simple way to cancel most of this shift [15]. Suppose that for both interferometers in the recoil pair, we reverse k_{eff} for every pulse after the initial preselection. This pair of inverted interferometers also measures the photon recoil shift, but it differs from the original interferometer in two ways. First, the atomic velocities are uniformly shifted by $\delta v = \hbar k_{\text{eff}}/m_{\text{Cs}}$. Secondly, the roles of the two internal states are interchanged. This second modification inverts the sign of the phase shift contribution from the quadratic Zeeman shift. If it were not for the spatial displacement caused by the velocity shift, the reversal would be perfect. The average spatial displacement of normal and inverted interferometers between the final beam-splitter pair is

$$\delta z = [1.5T + (N + 1)T_{\text{sp}}] (\hbar k_{\text{eff}}/m_{\text{Cs}}). \quad (4.3)$$

For typical parameters, $\delta z = 1.4$ mm, a factor of 22 [$\approx (N + 1)/1.5$] smaller than Δz under identical conditions. Consequently, the sign reversal is quite accurate for large N . Our approach is then to measure the recoil from the normal pair of interferometers, and then for the pair with reversed k_{eff} . By averaging the two measurements together, we cancel out most of the quadratic Zeeman shift contribution. (Note that the averaging can not be weighted by the fit uncertainties, or the cancellation will not be correct.) The residual error from the cancellation is caused by magnetic field variations over distances of δz , which from Fig. 3.2 is at most $\delta B \approx 0.02$ mG for $\delta z = 1.4$ mm. This gives a maximum quadratic Zeeman shift difference of 1.2 mHz, or a 1.3 ppb change of Δf_{rec} .

4.2.2 Detuning from the excited state

The detuning of the adiabatic passage beams from the $6P_{1/2}$, $F' = 3$ excited state can affect the result of the recoil measurement in two main ways. Clearly from the definition of Δf_{rec} in Eq. (2.30), imprecise knowledge of ν_{eff} can limit the calculation of Δf_{rec} . This issue of photon size is well under control at the present level of the measurement. A less obvious effect, ac Stark shift contributions to interferometer phase shifts, is far more threatening to the accuracy of the measurement. We also believe that we have well characterized the size of possible ac Stark shifts contributions from detuning. Since ac Stark shifts can enter in two ways—through excited state detunings and through nonadiabaticity (in the presence of an additional energy level), I will cover these effects together in Sec. 4.2.3.

The accuracy of the Raman beam lock to the cesium D_1 line sets the limits that we can place on both of these detuning effects. From regular observations of the lock accuracy using cold atoms, we estimate that the cesium lock error is about 100 kHz(rms). The cesium lock mostly compensates for the Doppler-shift of the atoms throughout the trajectory, but some residual error exists. I estimated in Sec. 3.3.2 that at the maximum velocities in the trajectory, the lock error may increase to about 200 kHz. For the photon size effect, all of the pulses contribute, including the complete transfer pulses. Since these pulses occur close to the top of the trajectory, where the atomic velocity is nearly zero, and since they transfer the most of the momentum, it is still reasonable to use the 100 kHz estimate for that effect. For the ac Stark shift effect, however, most of the contribution probably comes from the beam-splitter pulses, two of which occur with the atoms at high velocities. Consequently, it is more accurate to use the 200 kHz estimate for that case.

Assuming that \mathbf{k}_1 and \mathbf{k}_2 exactly counterpropagate, Eqs. (2.30) and (2.31) imply that $\Delta f_{\text{rec}} \propto (\nu_1 + \nu_2)^2$. For an atom interferometer on resonance, the two Raman beams have nearly identical single-photon detunings Δ . Hence we obtain the simple result

$$\frac{\delta(\Delta f_{\text{rec}})}{\Delta f_{\text{rec}}} \approx \frac{2\Delta}{\nu_1}. \quad (4.4)$$

Using $\Delta = 100$ kHz for the cesium lock accuracy gives a limit of 0.6 ppb from the

photon size.

4.2.3 ac Stark shifts

In our numerical simulations of adiabatic passage in Fig. 2.8 we found that a one-photon detuning Δ of the adiabatic passage beams causes a phase shift proportional to Δ . The phase shift is especially large if the transfer is not very adiabatic, which would suggest minimizing the problem by using very long beam-splitter pulses. On the other hand, the presence of a second energy level in the $6P_{1/2}$ excited state manifold causes a phase shift that grows monotonically with the pulse duration. Hence a trade-off exists for setting the beam-splitter pulse lengths.

One important characteristic of ac Stark shifts is that they should dominantly affect the recoil result through the beam-splitter pulses, not the complete transfer pulses. For all of the complete transfer pulses both branches of the interferometer are in the same internal state. Consequently, although ac Stark shifts may contribute to the phase of the atom at the pulse, the phase shift is nearly identical in both arms of the interferometer so no net phase shift occurs. This argument only breaks down to the degree that atoms in the two interferometer arms experience different light intensities. Since the displacement is at most about 1 mm and it is in the vertical direction, the intensity difference should be small for the 2-cm diameter Raman beams. Via ac Stark shifts, N should then only affect the size of the interferometer phase shift if the source of the shift is a spatial variation of intensity—larger N pushes the beam-splitter pulses further apart, thereby increasing the size of the phase shift.

Another important issue relating to ac Stark shifts is the dependence of the phase shift on T . The form of the dependence depends on the source of the shift. For fundamental consequences of the adiabatic passage process, such as those in Figs. 2.7 and 2.8, the result is a fixed phase shift during the interaction time; the free evolution time is irrelevant. If the net interferometer phase shift error is independent of T , then the error in the recoil measurement varies as $1/T$. Situations exist that yield other dependencies, however. For example, still consider the phase shifts from Fig. 2.7 and 2.8 but suppose that the light intensity varies over the positions of the

beam-splitter pulse interactions. Then the phase shifts will not cancel within the interferometer. In this case, the interferometer phase shift error grows with T . The exact dependence will depend on the form of the intensity variation and also the intensity dependence of the particular phase shift effect we are considering.

For the small one-photon detunings $\Delta < \Gamma/25$ that normally exist in the measurement, it would appear from Fig. 2.8 that the size of the detuning shifts would be relatively small compared with the magnitude of the shifts from the presence of the excited state. Consequently, we initially tried using fairly short $\tau = 40 \mu\text{s}$ beam-splitter pulses to reduce the excited state shifts. As we then varied Δ under these conditions, we obtained the recoil results shown by the solid circles in Fig. 4.2. We collected this data at a high sensitivity setting with $T = 120 \text{ ms}$ and $N = 30$. Each point is the average of the normal and inverted interferometers. A very interesting feature of this curve is that it has odd-parity, but the dominant effect is higher order than linear. The data fits reasonably well to a cubic polynomial (also shown in Fig. 4.2) with a linear slope through $\Delta = 0$ of -70 ppb/MHz . Using the 200 kHz estimate for the lock accuracy from Sec. 4.2.2 gives a 14 ppb error in Δf_{rec} from ac Stark shifts. This result only includes detuning-related Stark shifts, and assumes the shift is zero at $\Delta = 0$.

This 14 ppb error bar is larger than we would like. Since the dominant effect here is a detuning-related ac Stark shift, Fig. 2.8 suggests that we could reduce it by using longer beam-splitter pulses. Increasing from $\tau = 40 \mu\text{s}$ to $\tau = 250 \mu\text{s}$ produces the much improved results also shown in Fig. 4.2. Here a residual linear slope must be under about 10 ppb/MHz , which places an improved limit of 2 ppb on detuning-related ac Stark shifts.

To better understand the source of this shift, we focused on the size of the phase shift at a large detuning $\Delta = -16 \text{ MHz}$. We then varied T and N to determine the scaling of the net error in Δf_{rec} . The magnitude of the frequency shift varied as $1/T$ as expected for ac Stark shifts that are not spatially dependent. The recoil shift error also varied approximately as $1/(N+1)$. In this case, however, the error actually decreased slightly faster than expected as N increases. This is the opposite result than we would expect if the source of the error was a spatial variation of the field. Both

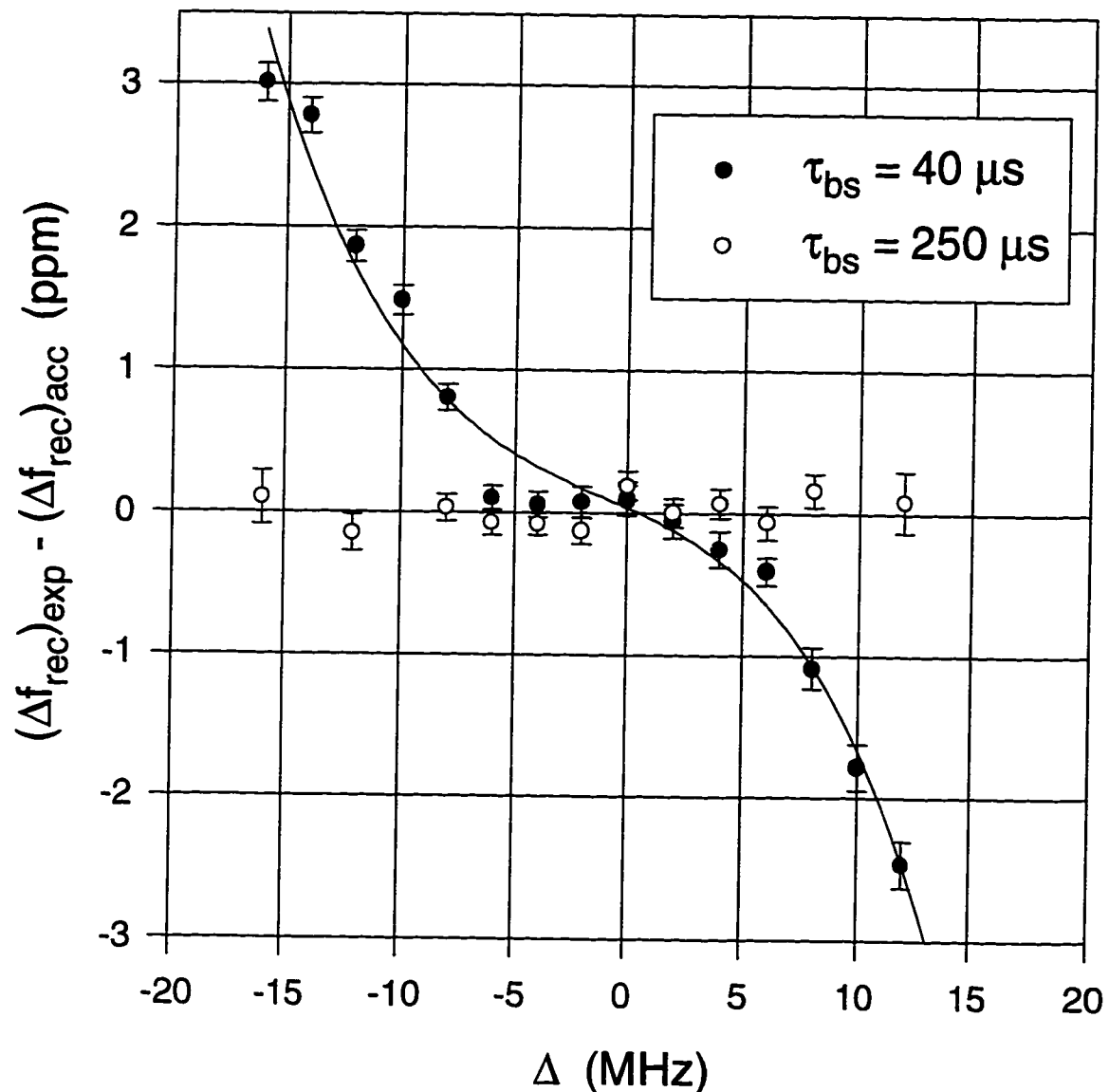


Figure 4.2: Variation of Δf_{rec} with the one-photon detuning. Large ac Stark shift errors occur for $T = 120$ ms, $N = 30$, and short beam-splitter pulses ($\tau_{bs} = 40 \mu s$) because of increasing nonadiabaticity as $|\Delta|$ increases. We fit a cubic polynomial to the data. The linear slope of the fit through $\Delta = 0$ is -70 ppb/MHz. For sufficiently long beam-splitter pulses ($\tau_{bs} = 250 \mu s$), the adiabaticity is sufficient to reduce the shift by over an order of magnitude at the extremes of the detuning range.

scaling results are consistent with the conclusion that the dominant error in Fig. 4.2 is caused by fixed phase shifts contributed by the beam-splitter pulses alone, so that increasing either T or N decreases the relative size of the error. This knowledge of the scaling allows us to remeasure the errors using the conditions $T = 1$ ms and $N = 0$, for which we have a higher signal-to-noise ratio. Figure 4.3 shows the results obtained under these conditions. Here we scale the vertical axis for the limits placed on the contribution of beam-splitter phase shifts for interferometers with $T = 120$ ms and $N = 30$. Ignoring the two extreme detuning points, at which a higher-order effect may dominate, any linear shift appears smaller than about 2 ppb/MHz. This places a yet smaller limit of 0.4 ppb on detuning-related ac Stark shift errors from the beam-splitter pulses. Since this result makes certain assumptions about the spatial dependence of the ac Stark shifts, the scaling of the recoil shift errors, and only includes contributions from beam-splitter pulses, it is probably preferable to use the 2 ppb limit obtained for interferometers with more typical parameters.

The tests above focused on detuning-related ac Stark shift errors. Detuning from resonance always hurts the adiabaticity of the transfer, so we would expect that most ac Stark shift errors would increase with $|\Delta|$. We have not yet performed comprehensive tests for a detuning-independent ac Stark shift error at $\Delta = 0$. One possible measurement would be to compare results obtained with 250 μ s and 400 μ s beam-splitter pulses for $\Delta = 0$. Since the reduction of fringe contrast is not too extreme with this change, such a test may place a reasonable limit on such errors.

4.2.4 Missed photon kicks

In most respects the addition of N complete transfer pulses into the Ramsey-Bordé interferometer helps to reduce the effects of systematic errors. Since the pulses interact with two interferometer paths that are in the same state, they do not contribute to ac Stark shifts (except spatially dependent intensity effects). In fact, a competitive fine-structure constant measurement using cesium would probably not be possible without the significant enhancement it provides. We would be forced to use an atom with a larger recoil velocity, such as lithium.

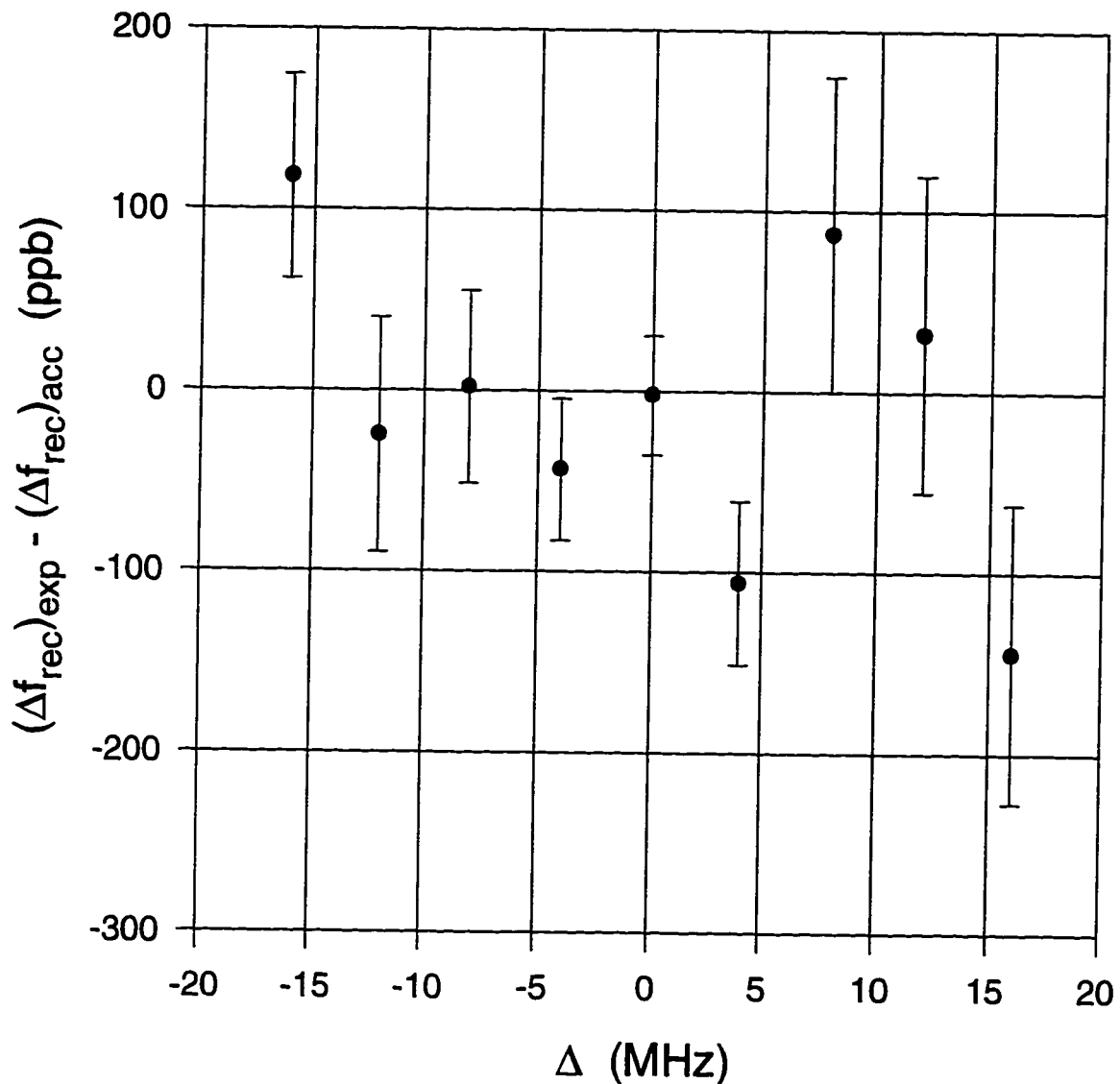


Figure 4.3: Errors in Δf_{rec} contributed by $250 \mu\text{s}$ beam-splitter pulses. We measure phase-shift errors from the beam-splitter pulses with $T = 1 \text{ ms}$ and $N = 0$, for which we have the best signal-to-noise ratio. The vertical axis shows the limits placed on errors in Δf_{rec} caused by the beam-splitter pulses in an interferometer with $T = 120 \text{ ms}$ and $N = 30$.

The most significant risk that these complete transfer pulses introduce is the possibility for Doppler-free transitions that do not deliver the anticipated momentum. Since a single Doppler-free transition in an interferometer causes a fractional change in the recoil frequency shift of order $1/N$, it may at first appear that these transitions must be eliminated practically to the same level as the desired precision of the measurement. Fortunately, that is not the case. Suppose that a fraction η of the atoms contributing to the interference signal make a Doppler-free transition. Then superimposed on the desired interferometer signal is a second set of fringes with equal periodicity, but with relative amplitude η and drastically shifted in phase by $\Delta\phi = (\hbar k_{\text{eff}}^2/m_{\text{Cs}})T$. As long as $\eta \ll 1$, we can still identify the integral number of cycles between the two interferometers in the recoil doublet. Consequently, the huge size of $\Delta\phi$ is irrelevant—all that matters is its remainder modulo 2π , which slightly shifts the location of the peak of the center fringe. The largest shift occurs for $\Delta\phi \bmod 2\pi = \pi/2$. In that case, the total interferometer signal as we vary the Raman detuning δ has the form

$$\begin{aligned} n_A(\delta) &= (1 - \eta) \sin \delta T + \eta \cos \delta T \\ &\approx (1 - \eta) \sin(\delta T + \eta), \end{aligned} \quad (4.5)$$

to lowest nonzero order in η . Consequently, Doppler-free transitions could certainly cause a phase shift, but the problem is not insurmountable.

A Doppler-free transition requires the presence of both $F = 3$ and $F = 4$ light from the same direction. Furthermore, the Raman detuning δ between the copropagating beams must be less than the dark-state frequency width for the Doppler-free transition, $\Delta\omega_D^{\text{DF}}$. We take steps to avoid both of these conditions.

Two possible sources exist for copropagating, on-resonant $F = 3$ and $F = 4$ light. First, when calcite polarizers combine and split the two beams before the optical fibers, they mix the two frequencies by about 6 ppm. A larger amount of light, however, probably arises from back reflections from optics. To minimize the back-reflected light striking the atoms, we tilted all of the Raman beam optics near the chamber, as indicated in Fig. 3.1. The only back reflection that partially makes it into the magnetic shielding is the 1.5×10^{-3} reflection from the upper vacuum

can window. We tilted that window at a 5° angle so that most of the light misses the atoms. Since the beams are large and some light may scatter off the walls of the solenoid, it probably is reasonable to assume a 10^{-4} level of back-reflected light. Having very low intensity for one of the adiabatic passage beams for the Doppler-free transition only reduces the dark-state width by a factor of $\sqrt{2}$ to $\Delta\nu_D^{\text{DF}} \approx 100$ kHz, but the transition is very nonadiabatic, so that few of the atoms that make a dark-state transition undergo the Doppler-free transition instead of the Doppler-sensitive transition.

We also use the Raman detuning to suppress Doppler-free Raman transitions. The Raman detuning always matches the Doppler-sensitive transition. The only time it also drives the Doppler-free transitions is when the atoms have nearly zero velocity. The probability of having more than one Doppler-free transition in a single interferometer is negligible since the probabilities multiply, but having several interactions with $|\delta| < \Delta\omega_D^{\text{DF}}$ increases the total probability that a single Doppler-free transition occurs. For the two interferometers in the recoil pair, one repeatedly receives upward momentum kicks, and the other recoils downward. With the present transfer-pulse spacing of 685 μs , the average rate of acceleration from photon recoils nearly matches gravitational acceleration. Consequently, the atoms in one interferometer stay nearly at constant velocity during the transfer pulses, and the atoms in the other interferometer accelerate downward at about $2g$. For the interferometers with constant velocity atoms, we ensure that the Doppler shift at that velocity is larger than $\Delta\nu_D^{\text{DF}} \approx 100$ kHz. This interferometer is then practically immune to Doppler-free transitions. It would of course be preferable to make sure that the atoms in the other interferometer do not decelerate through $v_z = 0$ during the transfer pulses, but that is hard to arrange for the most sensitive interferometers. Even if they do, the atoms only spend about 2 ms, or about 3 transfer pulses, in resonance with the Doppler-free dark state.

Assuming a 10^{-4} back reflection, we can estimate the resulting shift of the recoil measurement. By numerically integrating the time-dependent Schrödinger equation, we determined that the presence of an on-resonance ($\delta = 0$) back reflection with relative intensity η causes a fraction η of the atoms to be adiabatically transferred

via Doppler-free transitions. Then the probability for a Doppler-free transition in a downward-accelerated interferometer is at most about 3×10^{-4} . From Eq. (4.5), this gives at most a 3×10^{-4} rad fringe shift. For an interferometer with $T = 120$ ms and $N = 30$, the net phase shift is 7×10^5 rad, so the error in the recoil shift is at most 0.4 ppb. An order-of-magnitude error may exist in the estimation of the back-reflection intensity, but we have more likely overestimated than underestimated.

The problem of missed photon kicks is fundamentally different for adiabatic passage than for stimulated Raman transitions [15]. In that case, in addition to the problem of Doppler-free transitions, another potentially harmful process exists [15]. Imperfections of π pulses, which are certain to exist from intensity fluctuations or nonhomogeneities, naturally lead to atoms which do not change states (momentum or internal). Nonetheless, the coherence of the atomic state is preserved, so the atom can continue on through the interferometer sequence and create an interference signal. By using selective clearing of one of the two ground states between the final two $\pi/2$ pulses, the problem can be eliminated for odd numbers of missed transitions. Then the size of the recoil shift error is proportional to the square of the number of atoms left behind by a single π . Unfortunately, for Gaussian beams that probability can be fairly large. With adiabatic passage this effect vanishes because atoms that are not transferred coherently will scatter photons, so they do not contribute to the interferometer fringes. Experimentally it is a far more tractable problem to eliminate back reflections than to make perfect π pulses with Gaussian beams, so suppressing errors from missed photon kicks is easier with adiabatic passage.

4.2.5 Detuning from the Raman resonance

When the computer program calculates the Raman detuning frequencies for all of the pulses in an interferometer, it needs a value for $\mathbf{k}_{\text{eff}} \cdot \mathbf{g}$ to determine the Doppler-shift caused by gravity. Suppose that an error exists in that value, either from inaccurate knowledge of g or a misalignment of \mathbf{k}_{eff} along \mathbf{g} . Could that cause an error in the recoil measurement? Two possible sources of problems include detuning-related ac

Stark shifts or phase shifts from sloping backgrounds. We estimate that our inaccuracies in $k_{\text{eff}} \cdot g$ cause no more than a 5 kHz offset for the final beam-splitter pulses. Since this detuning is much smaller than the accuracy of the cesium lock, it should not be the dominant source of ac Stark shift errors. Consequently, I focus here on the possibility for phase shifts caused by sloping backgrounds.

As discussed in Sec. 4.1.1, atom interference fringes are modulated by the dark-state lineshape of the beam-splitter pulses. Inaccurate calculations of the shift from gravity cause us to collect data slightly off to the side on this envelope. The gradual modulation of the fringe amplitude would not cause of shift of the fitted fringe phase, but the gradually sloping background level might. Two factors keep this from causing a significant error in the recoil measurement. First, to suppress the shift of the fringe fits for the individual interferometers, we always collect data over several interferometer fringes. This helps to average out the effect of the sloping background because peaks and valleys shift in opposite directions. The actual amount of phase-shift suppression depends on the phase of the center point of the scan. Secondly, even if the individual interferometer fringe fits shift, the upper and lower interferometer fits shift nearly the same amount, so that the shifts cancels in the recoil measurement. The two fringe shifts are practically identical because we collect data for the interferometers at frequencies very accurately spaced by the correct recoil splitting, so the two sets of fringes are symmetrically placed in the modulating envelopes.

As a check of the validity of these conclusions, we purposely collected data detuned ± 20 kHz away from the center of the resonance. We left k_{eff} and g alone in the frequency calculations, but just detuned away from the Raman resonance for the final two beam-splitter pulses. We could not observe a systematic shift of Δf_{rec} at the 200 ppb level. Assuming a Gaussian dark-state resonance (see Fig. 3.6) of width 90 kHz for the beam-splitter pulses, the approximately 0.28 ratio between the slopes at 5 kHz and 20 kHz gives a limit of 56 ppb for errors from nonzero Raman detuning. This limit is still a little too large to completely rule out this effect experimentally at our present measurement precision. To obtain a more stringent experimental limit, we would either need to collect more data, or more accurately locate the resonance center. As detailed in the previous paragraph, we do not presently know of a physical

mechanism that would cause a significant systematic shift of the recoil measurement for nonzero Raman detuning, so we are not presently assigning a systematic error for this effect.

4.2.6 Beam misalignment or imperfect collimation

Regardless of the angle between the Raman beams, the effective wave vector $\mathbf{k}_{\text{eff}} \equiv \mathbf{k}_1 - \mathbf{k}_2$ correctly determines the momentum transfer. In this measurement, we align the Raman beams to counterpropagate, and claim to be measuring the photon recoil shift for perfectly counterpropagating beams. If we misalign the beams by an angle θ , then the square of the effective wave vector has a fractional error of

$$\begin{aligned} \frac{\delta(k_{\text{eff}}^2)}{k_{\text{eff}}} &= -\frac{2k_1 k_2 (1 - \cos \theta)}{k_{\text{eff}}^2} \\ &\approx -\frac{\theta^2}{4}, \end{aligned} \quad (4.6)$$

for $k_1 \approx k_2$. Since $\Delta f_{\text{rec}} \propto k_{\text{eff}}^2$, the photon recoil shift decreases by the same fractional amount. Note that this is always a shift to lower Δf_{rec} .

We overlap the two Raman beams at their focuses near the outputs of the two fibers with an estimated accuracy of about 0.5 mm. After collimation by a 2-m focal length lens, simple geometrical optics implies an alignment error of under 250 μrad . From Eq. (4.6), this sets an error limit of -16 ppb for Δf_{rec} . This is fairly close to the current statistical precision, but it is not a fundamental limit. We could easily improve the beam alignment using pinholes.

Imperfect collimation of the Raman beams causes basically the same effect as misalignment, except that θ varies with the radial position in the beam. We collimated the beams with a Melles Griot 50-mm diameter collimator. We estimate that we properly located the 2-m focal length collimation lenses with an accuracy of ± 0.5 cm. From simple geometrical optics, this would give an angular divergence of $\theta \approx 12 \mu\text{rad}$ after collimation at the beam waist for a 2-cm diameter beam. This is larger than the theoretical limit set for a Gaussian beam of that diameter, so geometrical optics should be valid. Ignoring the spatial variation of θ , Eq. (4.6) gives a worst-case error

of -0.04 ppb for Δf_{rec} . This is clearly a smaller problem than beam misalignment at present.

4.2.7 Raman beam wave-front distortion

The necessity for high quality Raman beam wave fronts becomes clear in light of the desired precision of this experiment. The photon recoil measurement is effectively a measurement of the number of optical wave fronts that an atom crosses because of photon recoils. For typical interferometer parameters $T = 120$ ms and $N = 30$, the total number of effective optical phase cycles between the two interferometers is $(N + 1)\Delta f_{\text{rec}}T \approx 10^5$. A 10^{-8} measurement of Δf_{rec} then requires a final phase error of less than $10^{-3}\lambda_{\text{eff}}$ ($\lambda_{\text{eff}} \approx 447$ nm). This is a stringent requirement, especially considering that our beam splitters and wave plates are only specified for $\lambda/8$ at 632.8 nm, which is nearly two orders of magnitude worse.

In the first generation recoil measurement, we observed several reductions of systematic errors as we improved the laser beam quality, so we suspected that it may still have been responsible for some of the remaining 800 ppb error in α . At that time we realized that with vertical Raman beams, we would have much better cancellation of large-scale wave-front distortions in the atom interferometer measurements. As illustrated in Fig. 4.4, gravity causes large displacements of atoms through phase distortions for horizontal beams. Consequently, the atoms cross a different number of optical wave fronts than would be expected for ideal plane waves. For vertical beams, only the transverse velocity of the atoms and the finite length scale of the distortion limit phase-error cancellation. By setting the probe beam diameter smaller than that of the Raman beams, we favor detection of atoms with relatively small transverse velocities, further improving the phase-error cancellation. It is difficult to estimate the actual level of this cancellation since it depends strongly on the spatial scale of the actual beam phase distortions.

Good experimental approaches exist for measuring the size of the wave-front errors, and then canceling them even more completely. In a light-pulse atom interferometer, an atom reads in the phase of the light whenever it makes a transition. For

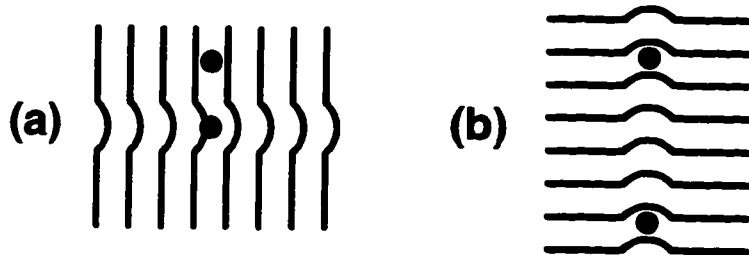


Figure 4.4: Cancellation of wave-front phase errors. The two dots indicate the spatial locations of the final two beam-splitter pulses relative to the optical wave fronts. (a) With horizontal beams, gravity causes large displacements through beam phase distortions during the time between beam-splitter pulses. (b) With vertical beams, the phase error is partially canceled between two beam-splitter pulses. The cancellation is best for small transverse atomic velocities and large length scale distortions.

two-photon transitions, the relevant light phase is $\phi_{\text{eff}} \equiv \phi_1 - \phi_2$, where ϕ_1 and ϕ_2 are the optical phases associated with beams k_1 and k_2 at the location of the atom. Suppose that a flaw in the optics for the lower Raman beam causes a phase distortion in that beam, but that the wave fronts for the upper Raman beam are relatively clean, as shown in Fig. 4.5. If k_{eff} is directed upward, as shown in Fig. 4.5(a), then the distortions of ϕ_{eff} cause the atoms to cross too few optical wave fronts, resulting in an underestimate of Δf_{rec} . For k_{eff} directed downward, the phase of k_2 is distorted instead of k_1 . This reverses the sign of the distortions in ϕ_{eff} , causing an overestimation of Δf_{rec} .

The perfection of this reversal depends on two main factors. First, it assumes that the optical fibers clean up the beam modes so that all beam phase distortions reverse with k_{eff} . Secondly, it assumes that we can reverse k_{eff} without changing the physical trajectory of the atoms. Relating to cancellation of magnetic-field shifts, Sec. 4.2.1 already described one approach that we normally take to reverse k_{eff} for the final two beam-splitter pulses. In that case reversing k_{eff} for every pulse after the preselection nearly inverts the sign of the quadratic Zeeman shift error. The chief distinction between magnetic-field shifts and wave-front phase errors is that while the former contribute over the entire time that the paths are in opposite internal states, the latter only contribute at atom-light interactions. The phase at the final

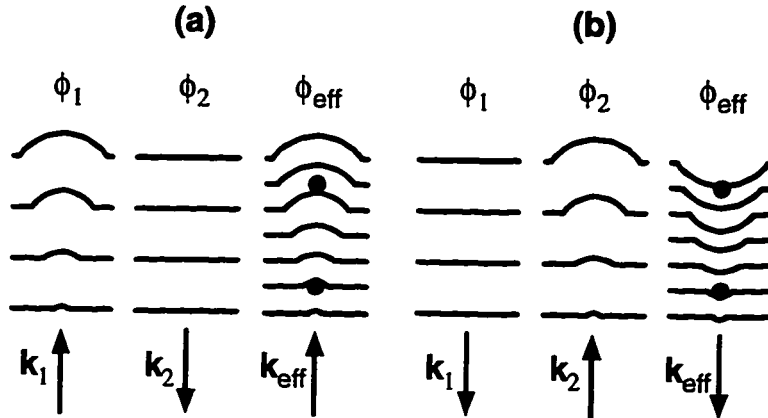


Figure 4.5: Reversal of wave-front phase errors with k_{eff} . Wave fronts are shown for both Raman beams, assuming that a distortion affects only the lower beam. The black circles represent the locations of the atoms in the upper and lower interferometers during the last beam-splitter pulse, when the spatial separation is greatest. The recoil measurement effectively counts the number of optical cycles between the two interaction locations. (a) If k_{eff} is directed upwards, only the wave fronts of k_1 are distorted. The atoms cross too few wave fronts, causing an underestimation of Δf_{rec} . (b) If k_{eff} is reversed, then k_2 is distorted and the sign of the error reverses.

beam-splitter pulse provides the dominant contribution to the error since that is when the spatial separation is the largest. The error suppression achieved by this reversal is then proportional to the ratio of the final spatial separation of the upper and lower interferometers to the final spatial separation between the normal and inverted interferometers, which is roughly a factor of $N + 1$. Another technique for reversing k_{eff} for the last beam-splitter pair is to switch between an even and odd number of pulses. This is a more complicated change, so it is not as clear how to correctly cancel phase errors from this reversal, but it at least serves as a test of the consistency of the reversals.

Figure 4.6 shows data collected using both of these reversal techniques. To test the wave fronts in various parts of the beam and for crossing different numbers of optical wave fronts, we vary N from 20 to 40 transfers. In each case, we measure Δf_{rec} using both normal and inverted interferometers. Before averaging, the errors in the normal and inverted interferometers are ~ 250 ppb. Of this, electronic phase shifts contribute roughly 75 ppb (see Sec. 4.2.8). The remaining shift is still about

an order of magnitude larger than the limits placed on quadratic Zeeman shift errors. Consequently, wave-front distortions quite likely are at fault. If the errors were caused entirely by wave-front distortions, we would expect the errors to reduce by a factor of $1/(N + 1)$ after averaging of the normal and inverted interferometer. This places a roughly 10 ppb limit on wave-front distortion errors for $N = 30$. Unfortunately, we see by comparing the consistency of results for different N in Fig. 4.6 that the residual errors after averaging are actually in the neighborhood of 50 ppb. This suggests that an additional systematic error is present that we have not yet identified, and that error does not flip sign with reversals of \mathbf{k}_{eff} . Until we resolve these discrepancies, we assign a 50 ppb systematic error limit to our measured value of Δf_{rec} .

4.2.8 Electronic phase shifts

Atom interferometry measurements basically use light fields as rulers for measuring the motion of atoms. The laser field establishes a set of wave fronts with periodicity λ_{eff} . Each time the light field causes an atom to make a transition, the atom records (in its phase) its position according to the ruler. Ideally we could leave the ruler fixed spatially for the entire measurement. Unfortunately, accelerations of the atoms from gravity and photon recoils causes the velocity to change so much that the interaction process no longer works, *i.e.*, the Doppler-shift exceeds the frequency width of the transition. Consequently, we generally need to shift the laser frequency to compensate for the Doppler-shift. In other words, we need to move the ruler to make the second measurement. As long as we know exactly how far we have moved the ruler, this is not a problem. In the process of shifting the laser frequency, however, frequency-dependent phase shifts in electronics may cause errors in the motion of the ruler between pulses.

Determining the restrictions our desired measurement accuracy places on the electronics requires finding the exact form of the dependence of the net interferometer phase shift on the electronic phase delays. Figure 4.7 shows the relevant electronic phase shifts for the two interferometers in the recoil measurement. The phases $\phi(f)$ correspond to the wave fronts established with \mathbf{k}_{eff} upward, and $\phi'(f)$ correspond to

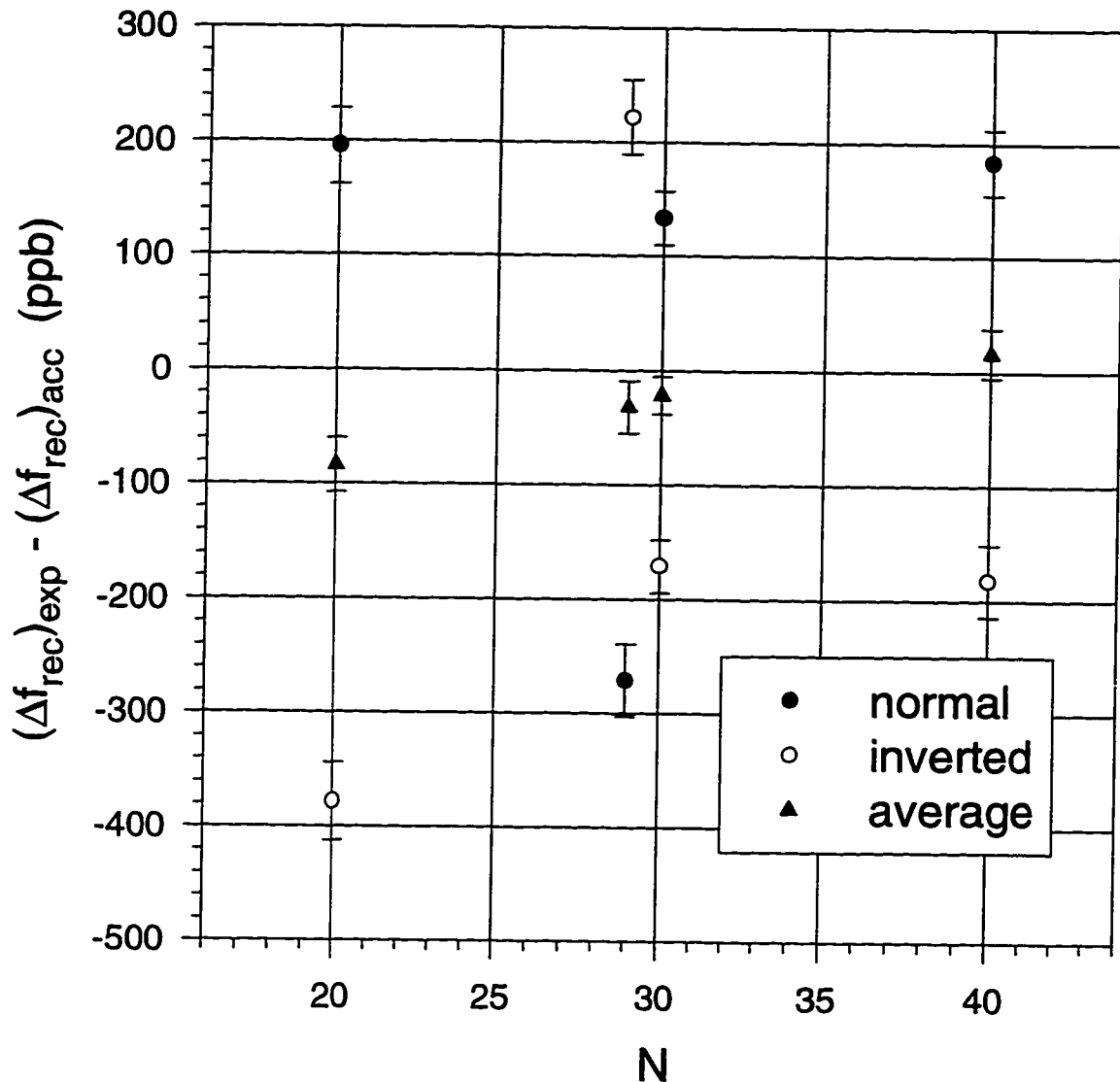


Figure 4.6: Variation of Δf_{rec} with reversals of k_{eff} . This data shows for various values of N the effect of k_{eff} reversals on the measured value for Δf_{rec} . Relatively large errors appear that nearly flip sign when k_{eff} is reversed for the final two beam-splitter pulses, either by switching from normal to inverted interferometers or by changing the parity of N . The errors include contributions from electronic phase shifts, wave-front distortions, and magnetic-field shifts. The accepted value $(\Delta f_{rec})_{acc} = 30,012.558\,8(29)$ Hz serves as the baseline for the data.

\mathbf{k}_{eff} downward. In each case we write the phase as a function of the laser detuning f_i for the i^{th} beam-splitter pulse. (Since a one-to-one correspondence exists between the laser detuning, the reference synthesizer frequency, and the microwave beatnote, f_i could equivalently represent any of those frequencies.) We can ignore the phase contributions at the complete transfer pulses because the atoms in both paths make identical transitions, so the phase shift is identical along both paths of an individual interferometer. The electronic phase delays cause the phase of the lower and upper interferometers to shift by an amount

$$\begin{aligned}\Delta\phi_L &= \phi'(f_4^L) - \phi'(f_3^L) + \phi(f_2) - \phi(f_1) \\ \Delta\phi_U &= \phi'(f_4^U) - \phi'(f_3^U) + \phi(f_2) - \phi(f_1).\end{aligned}\quad (4.7)$$

The net phase error in the recoil measurement from the electronic phase delays is the difference of the phase shifts in the upper and lower interferometers, or

$$\Delta\phi_{\text{rec}} = \phi'(f_4^U) - \phi'(f_4^L) - \phi'(f_3^U) - \phi'(f_3^L). \quad (4.8)$$

Note that the electronic phase shifts from the first and second beam-splitter pulses cancel in this differential measurement. Significantly, $\Delta\phi_{\text{rec}}$ has the form of a curvature estimate of $\phi'(f)$. If $\phi'(f)$ were completely linear in f , then it would not cause an error in the recoil measurement. The simplest source of a frequency-dependent phase shift in electronics is a time delay τ_d . This corresponds to a linear frequency-dependent phase shift $\phi(f) = 2\pi f \tau_d$. Consequently, fixed time delays do not cause a systematic shift of Δf_{rec} . Therefore, we need to worry mostly about those electronic components that have very nonlinear phase characteristics.

The only electronics that can contribute systematic shifts from nonlinear phase delays are those for which the signal frequency changes with the Raman beam detuning. Refer to Fig. 3.4 to identify those components. The most likely sources of nonlinear phase shifts are the low-pass filters on the output of the DDS-1EB synthesizer (the synthesizer itself has no internal filters for the output signal). We have measured the phase delay as a function of frequency for all of the rf reference electronics in Fig. 3.4 between the DDS-1EB and the Raman beam phaselock. From this data, we can correct for the error in the recoil shift caused by the nonlinear phase

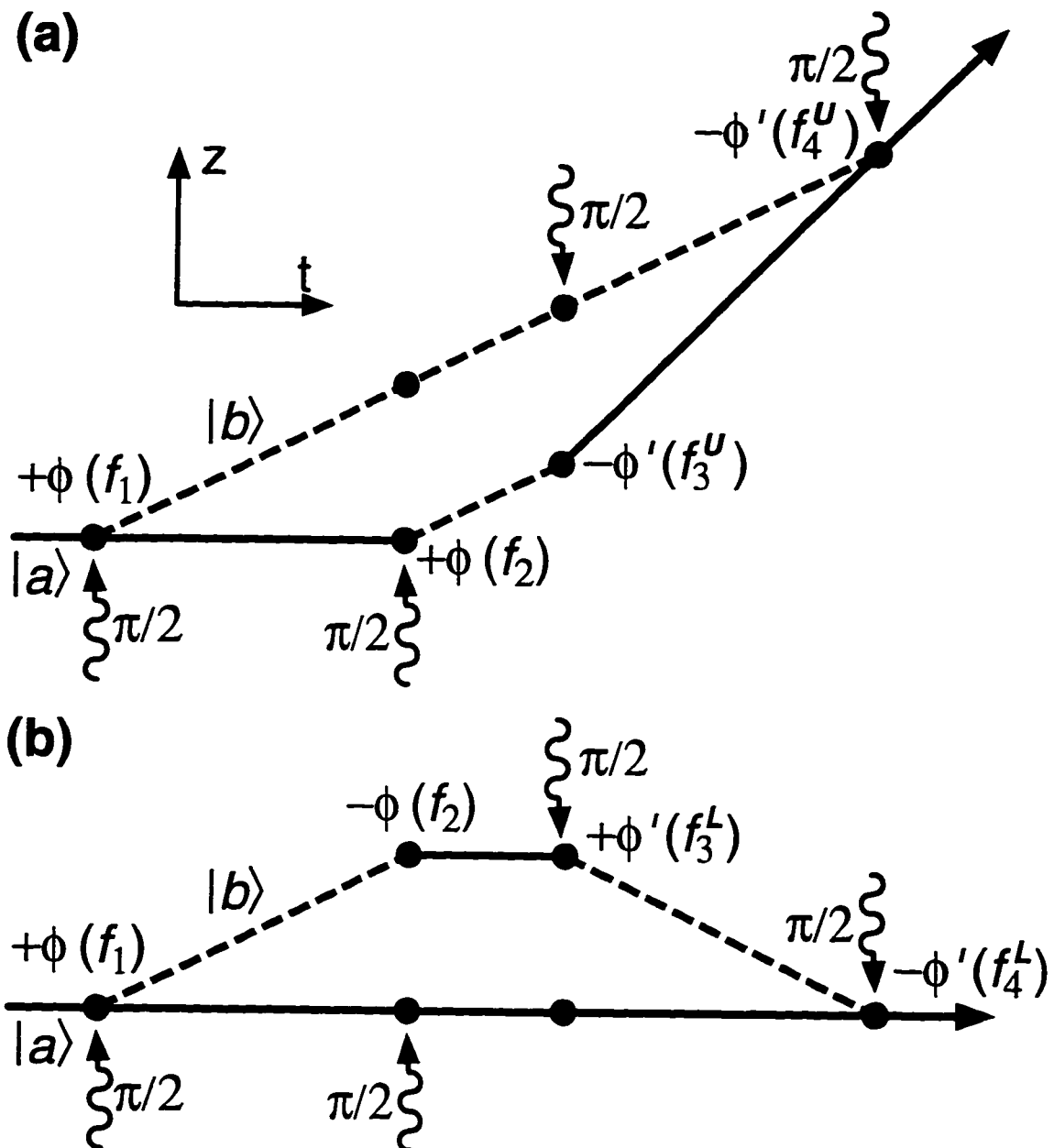


Figure 4.7: Contributions of electronic phase shifts to the recoil measurement. The phase shifts contribute at all atomic transitions. The phase shift is a function of the laser detuning f_i for the i^{th} beam-splitter pulse.

characteristics of the electronics. For the particular interferometers tested in Fig. 4.6, the resulting errors in Δf_{rec} vary from 40 ppb to 120 ppb. The corrections required for the average of the normal and inverted interferometers vary from -24 ppb for $N = 20$ to -40 ppb for $N = 40$. Since the size of this correction is fairly large, we will probably eventually want to replace the present low-pass filters with Bessel filters, which have a flatter time-response. The correction for this error varies depending on the actual synthesizer output frequencies, but since we have collected the most data with $T = 120$ ms and $N = 30$, I will quote the estimated correction of -24 ± 3 ppb for those parameter values and a standard interferometer starting time.

4.2.9 General tests for systematic errors

We have very flexible control over the parameters T and N defining the interferometer geometry. Changing these values influences a wide variety of systematic errors, so testing for consistency of the results with different geometries is a powerful general test for systematic errors, as already seen in Fig. 4.6.

Reducing T and N from their optimum values of $T \approx 120$ ms and $N \approx 30$ to the lower range of $T \approx 1$ ms and $N = 0$ decreases the measurement resolution by a factor of about 1000—a reduction that we can never compensate for to our desired uncertainty levels with increased integration time. However the increased sensitivity from large T and N actually scales down the sizes of the contributions of several possible systematic errors. Consequently, for those cases, the averaging time need not be increased to identify systematic errors at the level of our desired precision. For example, as noted in Sec. 4.2.3, the ac Stark shifts at large detunings scale down nicely with increases of both T and N . In the remainder of this section, I will focus on general tests for those systematics for which this scaling does apply. Those errors which do not scale with T and N generally include those caused by spatially dependent fields. For testing those effects we rely on data collected at maximum sensitivity, such as in Fig. 4.6.

Figures 4.8 and 4.9 show data collected over large ranges of T and N , respectively. I plot the data with the actual measurement uncertainties in Figs. 4.8(a) and 4.9(a).

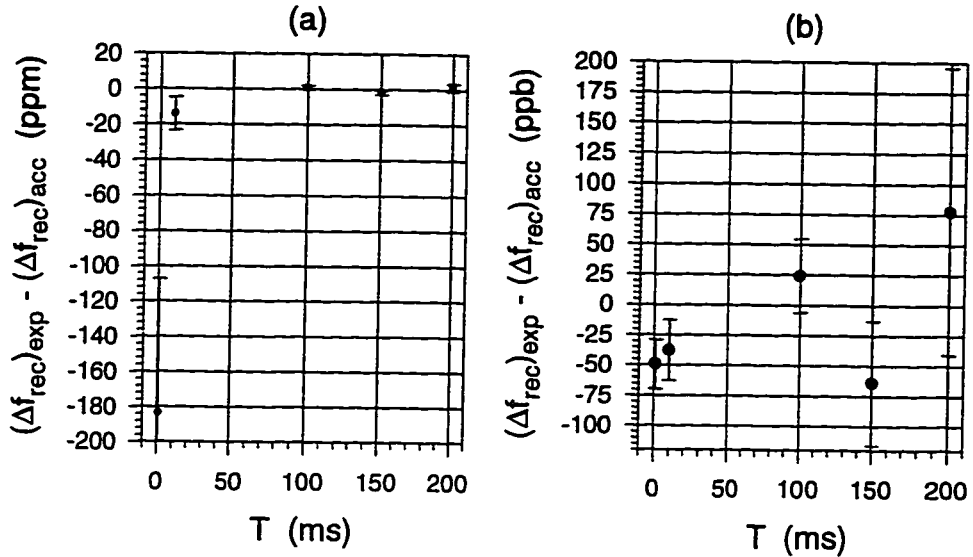


Figure 4.8: Variation of Δf_{rec} with T . (a) The actual recoil measurement results with their statistical error bars. (b) We scale the discrepancies and error bars for $T = 120$ ms and $N = 30$, assuming that they are caused by systematic errors that scale down with increasing T and N . This determines the limit that can be placed on scaleable systematics, but ignores the actual statistical error bar. The accepted value $(\Delta f_{rec})_{acc} = 30,012.5588(29)$ Hz serves as the baseline for both plots.

This shows the rather poor global limits placed by the data on all possible systematic errors. In Figs. 4.8(b) and 4.9(b), the error bars and discrepancies are scaled relative to $(\Delta f_{rec})_{acc}$ in order to show the limits placed on errors for data collected with $T = 120$ ms and $N = 30$. This assumes that the errors scale down with increasing N and T , such as ac Stark shift errors. The only statistically significant discrepancy occurs for the point with $T = 1$ ms and $N = 0$. We collected more data under those conditions, and it showed no systematic discrepancy the second time (see the $\Delta = 0$ point in Fig. 4.3). Unfortunately, the precision of this data is only sufficiently good to rule out variations with T and N at about the 50 ppb level, and even that only applies for systematic errors that scale. It is comforting, however, that we can change the parameters over two orders of magnitude without seeing gross trends. Significantly, inconsistent behavior with N and T were indicators of problems with systematic errors in the first generation recoil measurements. Any such trends are greatly reduced in the present data.

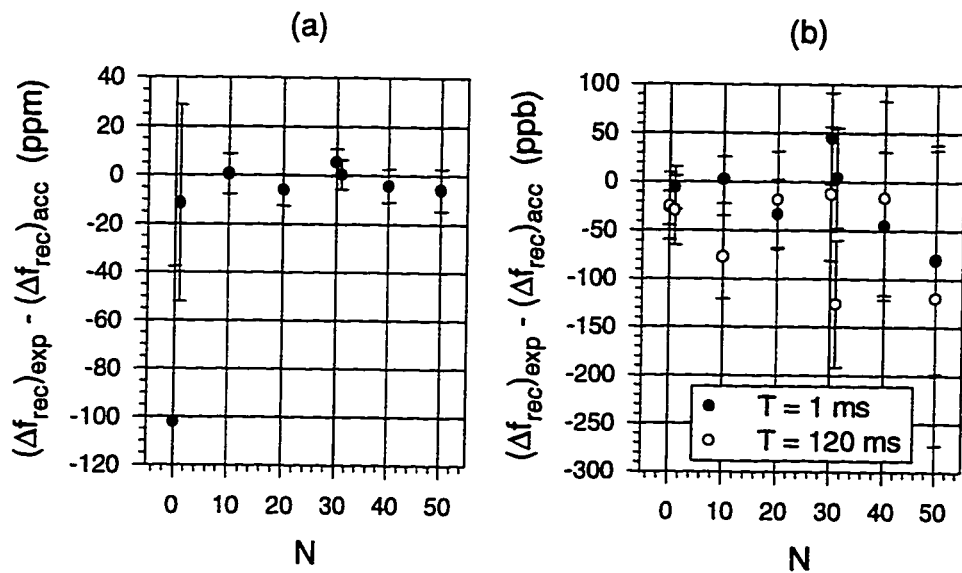


Figure 4.9: Variation of Δf_{rec} with N . (a) The actual recoil measurement results with their statistical error bars. (b) For data collected with $T = 1 \text{ ms}$ and $T = 120 \text{ ms}$, we scale the discrepancies and error bars for $T = 120 \text{ ms}$ and $N = 30$, assuming that they are caused by systematics that scale down with increasing T and N . This determines the limit that can be placed on scaleable systematics. The accepted value $(\Delta f_{\text{rec}})^{\text{acc}} = 30,012.5588(29) \text{ Hz}$ serves as the baseline for both plots.

4.3 Summary of recoil results

We have measured the photon recoil shift in cesium using counterpropagating laser beams on resonance with the $6S_{1/2}$, $F = 3 \leftrightarrow 6P_{1/2}$, $F' = 3$ and $6S_{1/2}$, $F = 4 \leftrightarrow 6P_{1/2}$, $F' = 3$ transitions. Figure 4.10 shows the consistency of data collected over a continuous period of about 4 hours for Ramsey-Bordé atom interferometers with beam-splitter separations of $T = 120$ ms and $N = 30$ momentum transfer pulses. Each point in Fig. 4.10(a) represents the average of two 90 s recoil measurements—one with normal interferometers and one with k_{eff} reversed. This average largely cancels shifts from wave-front phase errors and magnetic-field variations. For measurements over this time period, the standard deviation of averaged measurements continues to decrease for averaging times as long as 100 minutes. The uncorrected average for the entire 4-hour data set is

$$(\Delta f_{\text{rec}})_{\text{unc}} = 30,012.558\,01(66) \text{ Hz}, \quad (4.9)$$

where the 22 ppb 1σ error bar is based on the standard deviation for 100-minute time intervals from Fig. 4.10(b), but reduced to approximate the standard deviation of the mean for the entire 4-hour period.

Table 4.1 summarizes the systematic-error corrections and uncertainties for Δf_{rec} that have been developed throughout this section. Note that the correction for electronic phase shifts depends on T , N , and the start time for the interferometer. The particular value in Table 4.1 corresponds to interferometers with $T = 120$ ms and $N = 30$ that start about 180 ms before the peak of the unperturbed trajectory. Adjusting the value of Eq. (4.9) for the systematic-error corrections listed in Table 4.1 gives

$$\Delta f_{\text{rec}} = 30,012.557\,3(16)(7) \text{ Hz}, \quad (4.10)$$

where the first 1σ error bar is the 52 ppb systematic error uncertainty, and the second error bar is the 22 ppb statistical uncertainty after 4 hours of data.

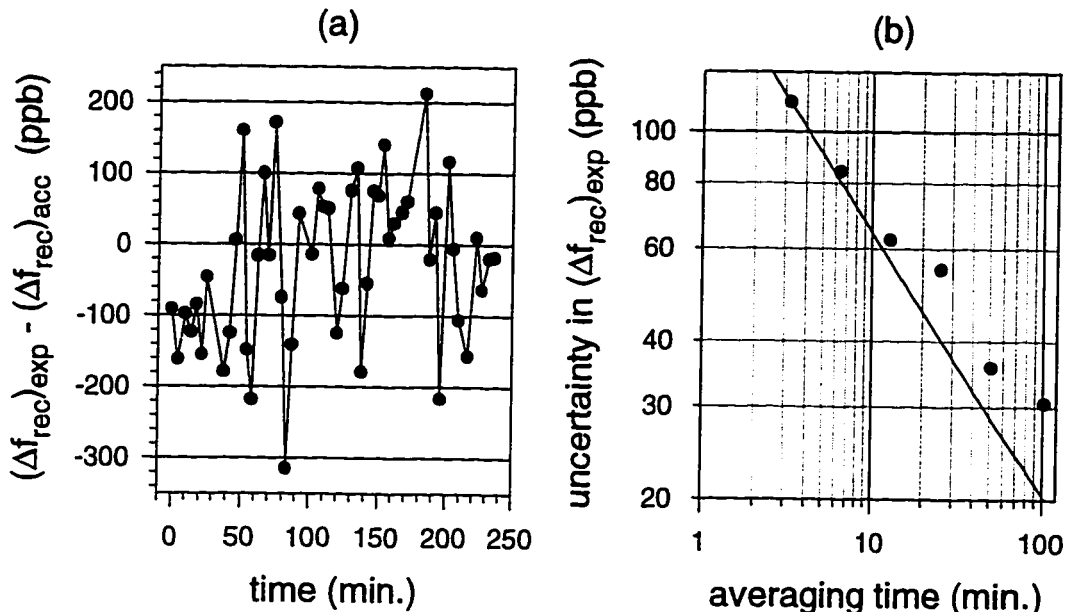


Figure 4.10: Data collected during a continuous 4-hour time period. (a) Each point is the average of two 90-s interferometer-pair measurements—one with k_{eff} reversed to cancel wave-front phase errors and magnetic-field shifts. (b) When the data is time-binned and averaged, the standard deviation of the averaged data continues to decrease for averaging times as long as 100 minutes, at which time the statistical uncertainty is 30 ppb for Δf_{rec} . The line shows the $t^{-1/2}$ dependence expected for random noise.

Table 4.1: Systematic corrections and error budget for Δf_{rec} .

Source of error	Correction \pm error (ppb)
Quadratic Zeeman shift	0 ± 1.3
Photon size	0 ± 0.6
ac Stark shift	0 ± 2
Missed photon kicks	0 ± 0.4
Beam misalignment	$+8 \pm 8$
Beam collimation	$+0.02 \pm 0.02$
Wave-front distortion	0 ± 10
Electronic phase shifts	-32 ± 3
Inconsistencies with N and T	0 ± 50
Total \pm quadrature sum	-24 ± 52

4.4 Determination of α

Table 4.2 lists the various physical constants, masses, and spectroscopic measurements that we use to calculate a value for α from the photon recoil measurement. For reference, it also lists the accepted value of α from the electron a_e measurement and the accepted value $(\Delta f_{\text{rec}})_{\text{acc}}$ it provides for the photon recoil shift. Substituting Δf_{rec} from Eq. (4.10) and the values from Table 4.2 into Eq. (2.34) gives for the fine-structure constant

$$\alpha^{-1} = 137.036\,002\,8(66)(36)(15), \quad (4.11)$$

where the first 1σ error bar is the 48 ppb uncertainty introduced into the calculation by the net effect of the quantities in Table 4.2, and the last two error bars are the 26 ppb and 11 ppb systematic and statistical uncertainties from Δf_{rec} .

The first error bar in Eq. (4.11) is only of temporary concern. Its dominant contributor is the uncertainty in the knowledge of the absolute frequency of the cesium D_1 line. This absolute frequency is also the quantity from Table 4.2 with the potential for the most drastic improvement in the near future. A chain of phase-locked lasers may be able to bridge the difference between the cesium D_1 line and an optical frequency standard [12]. The next limiting factor besides $(\Delta f_{\text{rec}})_{\text{exp}}$ is the ratio m_{Cs}/m_p . Experiments are presently underway to increase the precision of this mass ratio by about an order of magnitude [10].

Once those improved measurements are completed, the systematic error uncertainty of Δf_{rec} will grossly dominate the uncertainty in the determination of α . Chapter 5 will cover the prospects for further improvements in the measurement of Δf_{rec} .

Table 4.2: Various quantities needed to relate Δf_{rec} and α .

Physical quantity	Value	Units	Precision (ppb)	Ref.
Speed of light, c	299,792,458	m/s	defined	[71]
Rydberg constant, R_∞	10,973,731.568 30(31)	m^{-1}	0.028	[7]
Proton mass, m_p	1.007 276 470(12)	u	12	[71]
Cesium mass, m_{Cs}	132.905 442 3(45)	u	34	[9]
Proton/electron mass, m_p/m_e	1836.152 666 5(40)		2.2	[8]
Photon frequency, ν_{eff}	670,231,959(30)	MHz	45	[42, 11]
Fine-structure const., $\alpha^{-1}(a_e)$	137.035 999 44(57)		4.2	[2]
Photon-recoil shift, $(\Delta f_{\text{rec}})_{\text{acc}}$	30,012.558 8(29)	Hz	97	

Chapter 5

Future prospects

Within the basic context of the measurement described here, several options exist for improvements. Of premier importance is reducing the systematic error uncertainty, which is equal to the statistical uncertainty for only 30 minutes of data. Furthermore, fairly minor technical improvements could lead to a factor of at least two, and perhaps as much as an order-of-magnitude, increase in the measurement resolution of the present apparatus. The resulting shorter integration times would greatly facilitate the search for and characterization of systematic errors. Several revolutionary changes of the experiment may also lead to higher sensitivity, or at least provide a fairly independent measurement with much different sensitivity to systematic errors.

5.1 Short-term improvements

5.1.1 Reduction of systematic error uncertainty

To reduce the systematic error uncertainty, we need to identify the source(s) of the discrepancies of Δf_{rec} measurements with variations of T and N . One likely source of the problems is beam distortions involving diffraction. Such problems cause a systematic shift toward smaller Δf_{rec} values, similar to incorrect collimation and misalignment of the Raman beams. To reduce the uncertainty, we could either reduce the amplitude of the uncorrected errors, or we could try to improve the level to

which we cancel the errors. Taking the first route, we have recently been working on improving the optical quality of the wave fronts. Alteration of the probe and Raman beam diameters may also contribute toward this effort. For improved cancellation of the errors, we could experiment more with changes of the parity of N . Perhaps if we combined results from reversing k_{eff} directly and indirectly via the parity of N , we could further reduce the size of the uncertainty from wave-front distortions.

5.1.2 Improved measurement sensitivity

One physical limitation to the sensitivity of the present apparatus is the 23-cm length of the uniform bias field region within the solenoid. This places an upper limit of $T = 216$ ms for the beam-splitter separation times for a simple Ramsey-Bordé interferometer. The source of much of the data presented here is interferometers with $T = 120$ ms and $N = 30$. These interferometers span a vertical spatial range of 16.4 cm. For a fixed spatial region, it is sensible in the recoil measurement to trade off T for larger N since the required spatial extent for N pulses grows only roughly linearly with N , but quadratically with T . We could increase T by at most a factor of two (and that only at the expense of the 16-fold sensitivity improvement for $N = 30$). In theory, we could achieve arbitrarily large sensitivity improvements from increasing N (although it quickly requires reducing T from its present 120 ms value). Presently, amplitude noise of the atom signal is the limitation on increasing N . Consequently, the reduction of this amplitude noise is the primary focus for short-term sensitivity improvements. On the other hand, if the amplitude noise of the probe signal could be significantly reduced below its present 1.5% (rms), we could perhaps reduce N and still achieve a higher overall precision. We have already exerted much effort to reduce this amplitude noise, so additional gains, especially beyond a factor of about two, may require major modifications of the launch or detection. A normalization scheme for the total number of launched atoms may provide such a route to significant improvements. Unfortunately, initial attempts at normalization have failed. Of course, if future work successfully addresses the amplitude noise issues, there is no practical reason why the solenoid could not be made roughly twice as long.

5.1.3 Reducing amplitude noise from adiabatic passage

Compared to stimulated Raman transitions, adiabatic passage is relatively insensitive to the laser intensity. In the initial recoil measurement, the precision enhancement factor rolled off at $N \approx 15$, instead of the present $N \approx 30$. However, after enough transfers, small changes in the adiabaticity of the transitions—and consequently the transfer efficiency—take their toll. For example, we have observed that after about 50 transfers, a 10% change of the laser intensity causes a 10% change in the final signal size. Two options for dealing with this problem include increasing the average transfer efficiency or actively stabilizing the laser intensity.

Increasing the adiabatic transfer efficiency may reduce the sensitivity to intensity fluctuations of the laser. Figure 2.7 indicates that for a fourfold change of intensity, the transfer efficiency should only change roughly 2%. Scaling this down for 10% intensity fluctuations would predict a signal amplitude noise after 50 transfers of only 2.5% instead of the observed 10%. The present transfer efficiency is significantly short of the theoretical limit for the cesium D_1 line. The problem may be a poor alignment of \mathbf{k}_{eff} with the solenoid axis that causes loss from the presence of the nondegenerate magnetic sublevels. The justification for the present alignment is that \mathbf{k}_{eff} should be aligned with \mathbf{g} to minimize the transverse motion of atoms in the beams, which could increase wave-front distortion errors. Unfortunately we at present do not have a method of fine tuning the alignment of the solenoid, but that certainly should not be a serious obstacle.

A more certain approach for reducing the adiabatic passage noise is to stabilize the beam intensities. After peaking up the power on the Coherent Ti:Sapphire laser used for the Raman beams, the fluctuations in the output power are about 5%(rms). On the outputs of the optical fibers the intensity noise is about 8%(rms). The noise in the interferometer signal correlates well with slightly increased noise in the laser power. At both observation points, much of the large amplitude noise is at low frequencies (< 2 Hz). This actually is the worst situation for the interferometer signal. If the noise were high frequency (> 1 kHz) then the varying efficiency would average out over a large number of transfers. For low-frequency noise, the change of efficiency is nearly perfectly correlated for all N pulses, thereby adding the individual effects. The

fact that the noise is low frequency, however, increases the ease of actively reducing it.

Since the fibers contribute as much or more noise than the Ti:Sapphire, that must be a primary concern. Quite possibly that low-frequency noise is from etalon effects of the fibers caused by temperature or acoustic changes. We already have the fibers reasonably well shielded from the surrounding environment. A passive option for reducing that noise is to cleave the fibers at an angle. Regardless of a possible reduction of the fiber noise, the difficulty of stabilizing the beam intensities is the same regardless of where we measure the intensities, so for better control, the photodiodes for the active stabilization should be located after the fibers.

Two approaches for stabilizing the beam intensities include actively controlling the intensities for each individual pulse or just adjusting the intensity once per interferometer based on the measured intensity for a single initial pulse, *e.g.*, the preselection pulse. Active control of the shapes of all pulses would certainly yield the lowest amplitude noise for the interferometer. The only danger that this approach introduces is that the finite bandwidth of the feedback loop would further blur the transitions of the beam-splitter pulses. That could possibly cause systematic errors if the amplifiers and loop gain are not well matched. Providing the shaping AOM's with a feed-forward signal to set the basic shape, and then using the feedback loop only to correct for the noise fluctuation would speed up the transitions, but it would require two arbitrary waveforms for each Raman beam—a pre-linearized waveform for the feed-forward control and the desired intensity pattern for the feedback loop. Alternatively, a gated integrator could record the intensities of the $F = 3$ and $F = 4$ light for the preselection pulse, and scale the intensities of the remaining interferometer pulses accordingly. This would at least reduce the noise for frequencies lower than about 5 Hz.

5.1.4 Normalization of the probe signal

In the first recoil measurement, the probe signal had an amplitude noise of about 5%(rms). By measuring both the $F = 4$ and $F = 3$ populations, we were able to

normalize the $F = 4$ population for the total number of atoms. This reduced the amplitude noise by a factor of three to five [15]. This was an effective normalization technique for stimulated Raman transitions because very few atoms scattered large numbers of photons, so the total number of launched atoms was nearly conserved.

With adiabatic passage, however, atoms that are not in the dark state scatter many photons, which reduces the eventual detection efficiency in the probe region. The actual fraction of background atoms that do arrive at the PMT imaging region at the probe time varies with the interferometer parameters N and T , which increases the complexity of the normalization. We made some early attempts at normalization with adiabatic passage. For every launch cycle, we counted both the signal atoms in $m_F = 0$ and the atoms pumped into either $F = 3$, $m_F = 3$ or 4, or $F = 4$, $m_F = 4$. We attempted to generate a point-by-point weighted average of the signal and background atoms that served as an estimate for the total atom signal. Over a wide range of weighting factors, we were unable to normalize the fringes with a weighted average that produced a noticeably better signal-to-noise than the unscaled data. At the time that we performed these tests, the amplitude noise was much worse, and we were having difficulties with the microwave transitions that we were using, so it may be worth revisiting a normalization scheme such as this.

It may be that significant gains will be elusive for large N . Even for stimulated Raman transitions, the normalization process became less successful as N increased. The end result is that for a fixed measurement time, we now obtain roughly 12 times higher precision than in the first generation measurement. For the factors of seven and two increase in T and N , respectively, we would expect a 14-fold improvement for equal quality fringes. Consequently, even without normalization, we still have obtained nearly the expected gains over the previous measurement.

5.2 Major revisions of the recoil measurement

The work here has demonstrated that atom interferometry can compete favorably with other precision measurement techniques both in terms of sensitivity and accuracy. Consequently, it is reasonable to consider other more major revisions of the

experiment that may further boost the accuracy of the measurement, or help to test for systematic errors in atom interferometers. These changes may also include experimenting with other as yet undemonstrated forms of atom interferometers, such as the large-area interferometers described in Sec. 2.1.2.

5.2.1 Lower-mass atoms

Ever since the photon recoil measurement began, we have wondered whether cesium is the right atom for the measurement, or if we should be using a lighter atom with a larger recoil velocity such as lithium or sodium [15]. This round of experimentation has partially addressed some of the relevant issues surrounding that question.

One of the limits of the accuracy for modified Ramsey-Bordé atom interferometers as in Fig. 2.3(a) is the ratio of the optical wave-front distortion to the number of wave fronts that atoms cross because of the photon recoil(s). (Note that the wave-front distortion should be measured differentially along individual atomic trajectories.) The major advantage of using lower-mass atoms is that the atoms will cross a macroscopic distance very quickly from only a few photon recoils. In the present experiment, recoils from multiple photons displace the atoms about 5 cm without serious reduction of the original signal-to-noise. Fairly straightforward improvements may boost that by a factor of two. Consequently, to improve the measurement accuracy with lighter atoms would require either achieving larger displacements or more uniform wave fronts.

The most serious disadvantage of lighter atoms is their higher susceptibility to wave-front phase errors. Since the photon recoil cooling limit corresponds to a higher atomic velocity, atoms have larger transverse velocities that degrade the differential cancellation of wave-front phase distortions within interferometers. Aperturing of the atoms by a narrow probe beam can selectively image atoms with low transverse velocity, but this would also reduce the signal size. With cesium, relatively low transverse velocities are an automatic result of standard polarization-gradient cooling, so we only increase velocity in the direction we want it, not all three.

Although the accuracy may not improve with lighter atoms for an experiment on the same spatial scale, it may be quite possible to achieve a higher precision for a

given measurement time. We have observed that atom normalization techniques can yield considerable improvement in signal-to-noise for simple interferometers, but that the normalization fails for large N (see Sec. 5.1.4). Consequently, it is quite likely that a well designed experiment using lighter atoms with a simple interferometer may achieve much higher signal-to-noise ratios with the same total spatial separation. A higher sensitivity might allow a more thorough study of certain systematic errors than we performed here, although fewer experimental handles exist for testing systematics in simpler interferometers.

5.2.2 Large-area interferometers

As mentioned in Sec. 2.1.2, the large-area interferometer in Fig. 2.3(b) provides an N^2 enhancement of sensitivity for a nearly identical spatial displacement as the modified Ramsey-Bordé interferometer of Fig. 2.3(a), which only has a factor of N enhancement. This increased sensitivity for the same spatial displacement occurs because the optical wave fronts that are the “ruler” divisions for the measurement are spaced by λ_{eff}/N instead of λ_{eff} . The compression of the reference spacing results from the replacement of each original transition with N transitions. In essence, one factor of N arises from the N times increase in the displacement (as for the modified Ramsey-Bordé interferometer), and the second comes from the reduction of the wave-front spacing by a factor of N .

This perspective on these interferometers clarifies their comparative sensitivity to experimental noise and wave-front errors. They do indeed have higher sensitivity, but the sensitivity unfortunately extends to factors such as mirror vibrations and the Raman frequency reference phase noise. In these interferometers the first factor of N enhancement from spatial displacement would be reasonably straightforward to achieve, although not without some additional technical difficulties. The amount of the second factor of N that actually translates into improved sensitivity would depend on the quality and the stability of the optical wave fronts. Since this second factor of N is from replacing each effective photon with N effective photons from the same fields, nearly perfect correlation of the phase noise on the Raman frequency reference

and the Doppler-shifts from mirror vibrations (assuming closely spaced pulses) will cause these noise sources to be multiplied in amplitude by N . Consequently, this type of interferometer makes most sense in an experiment with its sensitivity clearly limited by amplitude noise, rather than phase noise or vibrational noise.

Since the present recoil measurement is limited in sensitivity by amplitude noise, it may be worthwhile to consider a large-area interferometer. These interferometers introduce a number of additional experimental complexities. With the modified Ramsey-Bordé interferometers, the stability of the phase of the Raman detuning was inconsequential for the transfer pulses because they acted on both interferometer arms. Consequently, we could rapidly switch frequencies and k_{eff} without caring about the phase of the Raman or tracer phaselocks. In the N^2 interferometer, the phase of the light during the transfer pulses is important since only one arm makes a transition. In actual fact, the $\sim 50 \mu\text{s}$ settling times for both of these locks is already sufficiently fast, so that should not be a major limitation. The more serious additional technical requirements would be on the vibration isolation reference since the loop gain is fairly borderline at present. Achieving better isolation factors may require a three-axis isolation system to eliminate the present limits from cross-coupling of noise between axes.

As mentioned in Sec. 2.2.2, the more significant change required for large-area interferometers would be a return to stimulated Raman transitions, since adiabatic passage is not good for leaving paths alone. At the present time no study has been completed regarding the absolute accuracy that can be achieved with atom interferometers using stimulated Raman transitions, especially regarding ac Stark shifts. Also it is unclear how well we can control systematic errors if we return to the far simpler retroreflected Raman beams. Perhaps high accuracy in light pulse atom interferometers always requires spectrally pure, counterpropagating beams. The anticipated rapid completion of the atom interferometry g measurement at Stanford may answer some of those questions.

Bibliography

- [1] R. S. Van Dyck, Jr., P. B. Schwinberg, and H. G. Dehmelt, Phys. Rev. Lett. **59**, 26 (1987).
- [2] T. Kinoshita, Phys. Rev. Lett. **75**, 4728 (1995).
- [3] M. E. Cage *et al.*, IEEE Trans. Instrum. Meas. **38**, 284 (1989).
- [4] E. Kruger, W. Nistler, and W. Weirauch, IEEE Trans. Instrum. Meas. **44**, 514 (1995).
- [5] E. R. Williams *et al.*, IEEE Trans. Instrum. Meas. **38**, 233 (1989).
- [6] T. Kinoshita, Rep. Prog. Phys. **59**, 1459 (1996).
- [7] F. Nez *et al.*, Phys. Rev. Lett. **69**, 2326 (1992).
- [8] D. L. Farnham, R. S. Van Dyck, Jr., and P. B. Schwinberg, Phys. Rev. Lett. **75**, 3598 (1995).
- [9] H. Stolzenberg *et al.*, Phys. Rev. Lett. **65**, 3104 (1990).
- [10] D. E. Pritchard, 1996, private communication.
- [11] K.-H. Weber and C. J. Sansonetti, Phys. Rev. A **35**, 4650 (1987).
- [12] T. W. Hänsch, 1996, private communication.
- [13] D. S. Weiss, Ph.D. thesis, Stanford University, 1993.
- [14] D. S. Weiss, B. C. Young, and S. Chu, Phys. Rev. Lett. **70**, 2706 (1993).

- [15] D. S. Weiss, B. C. Young, and S. Chu, *Appl. Phys. B* **59**, 217 (1994).
- [16] N. F. Ramsey, *Phys. Rev.* **78**, 695 (1950).
- [17] C. J. Bordé, *Phys. Lett. A* **140**, 10 (1989).
- [18] B. Young, M. Kasevich, and S. Chu, in *Atom Interferometry*, edited by P. R. Berman (Academic Press, Chestnut Hill, 1997), Chap. 9, pp. 363–406.
- [19] J. Ishikawa, F. Riehle, J. Helmcke, and C. J. Bordé, *Phys. Rev. A* **49**, 4794 (1994).
- [20] R. Friedberg and S. R. Hartmann, *Phys. Rev. A* **48**, 1446 (1993).
- [21] P. Storey and C. Cohen-Tannoudji, *J. Phys. II France* **4**, 1999 (1994).
- [22] M. Kasevich and S. Chu, *Phys. Rev. Lett.* **67**, 181 (1991).
- [23] M. Kasevich and S. Chu, *Appl. Phys. B* **54**, 321 (1992).
- [24] Y. V. Baklanov, B. Y. Dubetsky, and V. P. Chebotayev, *Appl. Phys.* **9**, 171 (1976).
- [25] J. C. Bergquist, S. A. Lee, and J. L. Hall, *Phys. Rev. Lett.* **38**, 159 (1977).
- [26] C. J. Bordé *et al.*, *Phys. Rev. A* **30**, 1836 (1984).
- [27] J. Oreg, F. T. Hioe, and J. H. Eberly, *Phys. Rev. A* **29**, 690 (1984).
- [28] U. Gaubatz *et al.*, *Chem. Phys. Lett.* **149**, 463 (1988).
- [29] J. R. Kuklinski, U. Gaubatz, F. T. Hioe, and K. Bergmann, *Phys. Rev. A* **40**, 6741 (1989).
- [30] P. Marte, P. Zoller, and J. L. Hall, *Phys. Rev. A* **44**, R4118 (1991).
- [31] M. Weitz, B. C. Young, and S. Chu, *Phys. Rev. A* **50**, 2438 (1994).
- [32] A. Abragam, *The Principles of Nuclear Magnetism* (Oxford Univ. Press, London, 1961).

- [33] C. P. Slichter, *Principles of Magnetic Resonance*, 3rd ed. (Springer-Verlag, Berlin, 1990).
- [34] D. Grischkowsky, Phys. Rev. Lett. **24**, 866 (1970).
- [35] M. M. T. Loy, Phys. Rev. Lett. **32**, 814 (1974).
- [36] Y. B. Band, Phys. Rev. A **47**, 4970 (1993).
- [37] U. Gaubatz, P. Rudecki, S. Schiemann, and K. Bergmann, J. Chem. Phys. **92**, 5363 (1990).
- [38] C. J. Bordé, in *Laser Spectroscopy X*, edited by M. Ducloy, E. Giacobino, and G. Camy (World Scientific, Singapore, 1992), pp. 239–245.
- [39] P. Pillet, C. Valentin, R.-L. Yuan, and J. Yu, Phys. Rev. A **48**, 845 (1993).
- [40] J. Lawall and M. Prentiss, Phys. Rev. Lett. **72**, 993 (1994).
- [41] L. S. Goldner *et al.*, Phys. Rev. Lett. **72**, 997 (1994).
- [42] J. Abele, Z. Phys. A **274**, 185 (1975).
- [43] M. Weitz, B. C. Young, and S. Chu, Phys. Rev. Lett. **73**, 2563 (1994).
- [44] G. Alzetta, A. Gozzini, L. Moi, and G. Orriols, Nuovo Cimento **36B**, 5 (1976).
- [45] E. Arimondo and G. Orriols, Lett. Nuovo Cimento **17**, 333 (1976).
- [46] H. R. Gray, R. M. Whitley, and C. R. Stroud, Jr., Opt. Lett. **3**, 218 (1978).
- [47] W. Rudin, *Principles of Mathematical Analysis* (McGraw-Hill, New York, 1976).
- [48] F. Riehle *et al.*, Phys. Rev. Lett. **67**, 177 (1991).
- [49] P. D. Featonby *et al.*, Phys. Rev. A **53**, 373 (1996).
- [50] W. Ertmer, R. Blatt, J. L. Hall, and M. Zhu, Phys. Rev. Lett. **54**, 996 (1985).
- [51] K. Moler, D. S. Weiss, M. Kasevich, and S. Chu, Phys. Rev. A **45**, 342 (1992).

- [52] D. S. Weiss *et al.*, in *Light Induced Kinetic Effects on Atoms, Ions and Molecules*, edited by I. Moi *et al.* (ETS Editrice, Pisa, 1991), pp. 35–44.
- [53] J. L. Hall, L. Hollberg, T. Baer, and H. G. Robinson, *Appl. Phys. Lett.* **39**, 680 (1981).
- [54] C. E. Wieman and L. Hollberg, *Rev. Sci. Instrum.* **62**, 1 (1991).
- [55] G. White and G. M. Chin, *Opt. Commun.* **5**, 374 (1972).
- [56] E. L. Raab *et al.*, *Phys. Rev. Lett.* **59**, 2631 (1987).
- [57] D. W. Sesko, T. G. Walker, and C. E. Wieman, *J. Opt. Soc. Am. B* **8**, 946 (1991).
- [58] A. M. Steane and C. J. Foot, *Europhys. Lett.* **14**, 231 (1991).
- [59] P. J. Ungar, D. S. Weiss, E. Riis, and S. Chu, *J. Opt. Soc. Am. B* **6**, 2058 (1989).
- [60] D. S. Weiss *et al.*, *J. Opt. Soc. Am. B* **6**, 2072 (1989).
- [61] J. Dalibard and C. Cohen-Tannoudji, *J. Opt. Soc. Am. B* **6**, 2023 (1989).
- [62] N. F. Ramsey, *Molecular Beams* (Oxford Univ. Press, Oxford, 1956).
- [63] T. J. Sumner, J. M. Pendlebury, and K. F. Smith, *J. Phys. D* **20**, 1095 (1987).
- [64] C. J. Myatt, N. R. Newbury, and C. E. Wieman, *Opt. Lett.* **18**, 649 (1993).
- [65] J. H. Shirley, *Opt. Lett.* **7**, 537 (1982).
- [66] G. C. Bjorklund, *Opt. Lett.* **5**, 15 (1980).
- [67] M. Long-Sheng and J. L. Hall, *IEEE J. Quantum Electron.* **26**, 2006 (1990).
- [68] L.-S. Ma, P. Jungner, J. Ye, and J. L. Hall, *Opt. Lett.* **19**, 1777 (1994).
- [69] M. Kasevich, 1994, private communication.
- [70] J. M. Hensley, A. Peters, and S. Chu, (to be published).
- [71] E. R. Cohen and B. N. Taylor, *Rev. Mod. Phys.* **59**, 1121 (1987).